Evaluation of Aeolus wind observations and their contribution to surface wind forecasts

Zuo, Haichen

Link to article, DOI:
10.11581/DTU.00000292

Publication date:
2023

Document Version
Publisher's PDF, also known as Version of record

DTU Wind and Energy Systems
Meteorology and Remote Sensing

Evaluation of Aeolus wind observations and their contribution to surface wind forecasts

Haichen Zuo

PhD thesis

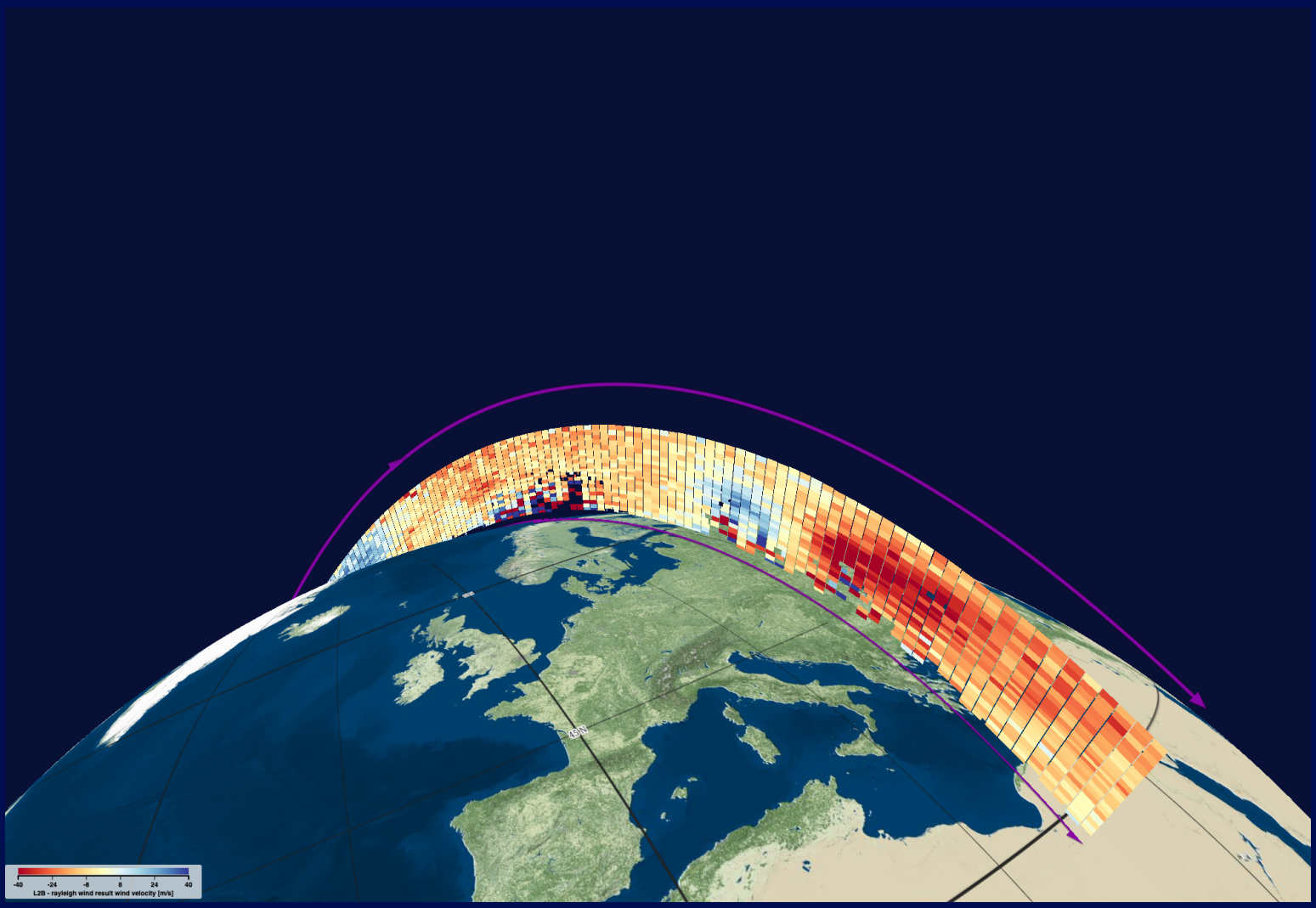

Evaluation of Aeolus wind observations and their contribution to surface wind forecasts

PhD Thesis
August 31, 2023

By
Haichen Zuo

Cover photo: Produced by using VirES for Aeolus
Published by: DTU Wind and Energy Systems, Frederiksborgvej 399, 4000 Roskilde, Denmark
Website: https://wind.dtu.dk/
DOI: 10.11581/DTU.00000292

Preface

This thesis is the result of a three-year PhD project Aeolus Satellite Lidar for Wind Mapping carried out at the Department of Wind and Energy Systems of Technical University of Denmark. The presented work was done between August 2020 and August 2023 and was supervised by Charlotte Bay Hasager, with co-supervision from Ioanna Karagali and Xiaoli Guo Larsén. During the PhD study, two 3-month external research stays were spent at the Royal Netherlands Meteorological Institute (KNMI) in De Bilt, the Netherlands. This PhD project is a part of the Innovation Training Network Marie Skłodowska-Curie Actions: Lidar Knowledge Europe (LIKE), supported by the European Union Horizon 2020 (Grant number: 858358).

This PhD thesis is article-based and consists of two parts: Part I Synopsis and Part II Appendix. Part I provides an overview of the PhD study and introduces how the articles relate to each other. Part II is a collection of three journal articles.

Haichen Zuo

Risø, August 2023

Abstract

Wind profile information is critical for understanding atmospheric dynamics and improving numerical weather prediction (NWP), which in turn benefits our daily activities and supports decision-making in a variety of industries, such as renewable energy, aviation, and ocean shipping. However, the absence of distributed wind profile measurements, particularly in regions over the oceans, tropics, and Southern Hemisphere, is one of the major deficiencies of the Global Observing System. To fill this gap, the European Space Agency launched the Aeolus satellite in August 2018. Owing to the state-of-the-art onboard Doppler wind lidar (DWL), the vertical profile of the horizontal line-of-sight (HLOS) wind velocity can be determined based on the Doppler shift of light backscattered by air molecules and particulates moving with winds. Before wind profile data can be utilized for practical applications, such as in the wind energy sector, comprehensive assessments of their error characteristics and their value to NWP model performance are required.

In light of the above, this PhD study aims to evaluate the performance of the space-borne DWL in wind profile detection and its contribution to near-surface wind forecasts. This study is scoped by three objectives. The first objective is to validate the wind profiles of Aeolus over Australia, which complements the validation in the Southern Hemisphere. The second objective is to investigate the impact of Aeolus wind profile assimilation on global sea surface wind forecasts based on the observing system experiments conducted by the European Centre for Medium-Range Weather Forecasts (ECMWF) comparing to surface wind observations from satellite scatterometers and ocean buoys. The third objective is to assess Aeolus' impact on near-surface wind forecasts over high-latitude lands in both hemispheres comparing to weather station data. Inter-comparison and triple collocation analyses were performed to achieve these objectives.

By taking wind profile measurements from ground-based wind profiling radars (WPRs) as the reference data, the Aeolus wind profile validation in Australia demonstrates that both Rayleigh-clear and Mie-cloudy winds achieve the mission bias requirement of 0.7 m s^{-1}. Mie-cloudy winds are more precise than Rayleigh-clear winds, with random errors of 4.14 m s^{-1} and 5.81 m s^{-1}, respectively. Similar precisions are obtained from the triple collocation analysis based on the Aeolus, WPR, and ECMWF model data. In addition, the inter-comparison analysis shows that Mie-cloudy winds have smaller bias and higher precision than Rayleigh-clear winds at altitudes below 1,500 m, suggesting a greater influence of Mie-cloudy than Rayleigh-clear winds on data assimilation for NWPs in the planetary boundary layer.

Verifications based on the ECMWF Aeolus impact experiments and ocean surface wind observations indicate that Aeolus benefits the short-range (within 12 hours) sea surface wind forecasts for the global ocean, except in the tropical regions. Moreover, Aeolus can reduce the

large-scale zonal biases of the short-range forecasts, whereas its impact on meridional biases varies with regions. As the forecast step is extended to T+120 h, the positive impact of Aeolus becomes more evident, particularly for the extratropical ocean regions in the Southern Hemisphere. For high-latitude lands, the positive contribution of Aeolus is mainly observed in the Northern Hemisphere after T+120 h, during the period with good Aeolus data quality, and during boreal winter and stormy conditions.

The research conducted in this PhD study extends our understanding of Aeolus observations and their performance in wind profile detection and their contribution to surface wind forecasts over the global ocean and over land at high latitudes in the Northern and Southern Hemispheres.

Dansk resumé

Det er vigtigt at kende vindprofilet, som er vindens variation vertikalt, for at kunne forstå de atmosfæriske dynamiske processer og dermed forbedre forudsigelsen af vejret. Vejrudsigter er nødvendige i mange beslutninger inden for industrier såsom vedvarende energi, flytrafik, navigation, mm. Manglen på vindprofil data især over oceanerne, i troperne og på den sydlige hemisfære er en svaghed ved det globale observations system. For at forbedre dette forhold opsendte det Europæiske Rumagentur (ESA) Aeolus satellitten i august 2018. Aeolus har en Doppler vind lidar ombord og dette instrument måler det vertikale profil af vinden som horisontale line-of-sight observationer. Det sker ved at lyset fra lidaren tilbagereflekteres fra partikler og gasser i luften og deres bevægelse forårsaget af vinden registreres ved Doppler skift. Det er nødvendigt at foretage en evaluering af kvaliteten af disse nye vindprofil data og at kvantificere deres nytteværdi i forhold til vejrmodeller inden Aeolus anvendes inden for bl.a. vind energi.

Baseret på de ovennævnte forhold er formålet med Ph.D. studiet at evaluere kvaliteten af vindprofil data fra Aeolus og disse datas bidrag til at forbedre vejrforudsigelse af vinden nær jordens overflade. Det første delmål er at kvantificere Aeolus vindprofil data kvaliteten i Australien for at bidrage med øget viden om forholdene på den sydlige halvkugle og dermed komplementere den eksisterende viden. Det andet delmål er at undersøge betydningen af at assimilere Aeolus vind profil data til forudsigelse af vinden nær havets overflade globalt ved at sammenligne model kørsler fra det European Centre for Medium-Range Weather Forecasts (ECMWF) med og uden Aeolus i vejrmodellen med vind observationer fra satellit scatterometer og havbøjer. Det tredje delmål er at undersøge samme men over landjorden i områder på høje breddegrader på den nordlige og sydlige hemisfære ved at sammenligne med vind observationer fra vejrstationer. For at nå delmålene er anvendt såvel komparative analyser og triple collocation med tre data sæt i én analyse.

Resultater fra studiet i Australien af Aeolus vindprofil data sammenlignet med vindprofil data fra jordbaserede radar instrumenter viser at både Aeolus Rayleigh-clear og Mie-cloudy vind data ligger inden for missionens krav om bias mindre end 0.7 m s^{-1}. Mie-cloudy vind data er mere præcise end Rayleigh-clear vind data, med spredninger på henholdsvis 4.14 m s^{-1} and 5.81 m s^{-1}. Lignende resultater er fundet ved at anvende triple collocation analyse af Aeolus vindprofiler, radar vindprofiler og vindprofiler fra ECMWF model data. Endvidere viser studiet at Mie-cloudy vind data har mindre bias og mindre spredning end Rayleigh-clear i vindprofilet fra overfladen til 1.500 m. Dette forhold kan være en årsag til at der vil være en større effekt af Mie-cloudy end Rayleigh-clear vindprofiler i vejrmodellerne til at forudsige vinden i det atmosfæriske grænselag.

Baseret på data fra ECMWF's numeriske eksperimenter, som har til formål at demonstrere den mulige betydning af at assimilere Aeolus i forhold til forudsigelse af vejret på korte, mellem og lange fremskrivninger, er følgende resultater opnået ved at sammenligne med observationer af vinden nær overfladen. På den korte tidsskala (indenfor 12 timer), viser studiet at Aeolus forbedrer forudsigelse af vinden over havet globalt, dog med undtagelse af de tropiske områder sammenlignet med observationer af vinden fra satellit scatterometer og havbøje data. Endvidere formindsker Aeolus bias i forudsigelsen af den zonale vind set over større regioner, mens bias i den meridonale vind varierer for regionerne. På den længere tidsskala, T=120 h, giver Aeolus en endnu tydeligere positiv indvirkning end for de korte tidsskalaer, især for forudsigelse af vinden over havet syd for troperne i den sydlige hemisfære. Også på land på høje breddegrader forbedrer Aeolus forudsigelse af vinden sammenlignet med observationer fra vejrstationer. Dette er tydeligst for en periode med gode Aeolus data samt for vinter og storm.

Forskningen fra dette Ph.D. studie bidrager til at øge vores forståelse af Aeolus vindprofil observationer og disse datas bidrag til at forbedre forudsigelsen af vinden nær overfladen over havet globalt og over land på høje breddegrader i nord og syd.

Acknowledgements

There are many who helped me along the way on this PhD journey. I would like to take a moment to extend my heartfelt appreciation to them.

First of all, I would like to thank Charlotte Bay Hasager, Jakob Mann, and Ioanna Karagali for providing me with the opportunity to pursue this project for my PhD degree. My deepest gratitude is expressed to my main supervisor, Charlotte Bay Hasager, who initialized this amazing project and kept me on the right track while ensuring this three-year study was productive and enjoyable. My big thanks also go to my co-supervisor, Ioanna Karagali, who led me into the field of Aeolus satellite and provided valuable guidance on data processing and academic writing. Equally, I would like to extend my warm thanks to another co-supervisor, Xiaoli Guo Larsén, who has always been a great source of support during the past three years.

A very special appreciation goes to Ad Stoffelen from KNMI, who was the host supervisor when I undertook my external research stays at KNMI and to whom I owe a great deal of gratitude for his shining advice, patient guidance, and continued support throughout this project. Special thanks should also go to Gert-Jan Marseille, Jos de Kloe, and Anton Verhoef from the Active Instruments Group at KNMI and Michael Rennie from the ECMWF for their academic suggestions, constructive comments, and technical support. Without their help, my PhD project cannot move forward smoothly.

In addition, I would like to say a big thank you to all the colleagues from the Meteorology and Remote Sensing section at DTU and members from LIKE. Your expertise, kindness, enthusiasm, and humor build a pleasant working environment that makes my three-year PhD life rewarding, enjoyable, and memorable. Sincere thanks also go to Marc Imberger, Xiaoying Liu, Sara Müller, Oscar Manuel Garcia Santiago, Xiaonan Wang, Zhixiong Wang, and Ke Zhao for all your help throughout this PhD study.

Last but not least, I have to mention my parents, relatives, and friends. Without their constant understanding, support, and encouragement, I would not be in the position I am today.

Abbreviations and Acronyms

4D-Var – Four-Dimensional Variational Data Assimilation
ALADIN – Atmospheric Laser Doppler Instrument
AMDAR – Aircraft Meteorological Data Relay
AMV – Atmospheric Motion Vector
ASCAT – Advanced Scatterometer
AUX_MET – Auxiliary Meteorological Data
AWDP – ASCAT Wind Data Processor
DWD – Deutscher Wetterdienst
DWL – Doppler Wind Lidar
ECMWF – European Centre for Medium Range Weather Forecasts
ESA – European Space Agency
ESD – Error Standard Deviation
FM-A – Flight Model A
FM-B – Flight Model B
GOS – Global Observing System
HLOS – Horizontal Line-Of-Sight
HSCAT – Haiyang Scatterometer
IFS – Integrated Forecasting System
KNMI – Royal Netherlands Meteorological Institute
L2B – Level-2B
LOS – Line-of-sight
LT – Local Time
MAD – Median Absolute Deviation
MARS – Meteorological Archival and Retrieval System
MBE – Mean Bias Error
Metop – Meteorological Operational
NCRMSD – Normalized Change in Root Mean Square Difference
NCRMSE – Normalized Change in Root Mean Square Error
NH – Northern Hemisphere
NOAA – National Oceanic and Atmospheric Administration
NRT – Near Real-Time
NWP – Numerical Weather Prediction

OSE	–	Observing System Experiment
PBL	–	Planetary Boundary Layer
PenWP	–	Pencil Beam Wind Processor
RMSD	–	Root Mean Square Difference
RMSE	–	Root Mean Square Error
SAF	–	Satellite Application Facility
SD	–	Standard Deviation
SH	–	Southern Hemisphere
TC	–	Triple Collocation
TKE	–	Turbulence Kinetic Energy
UK Met Office	–	United Kingdom Meteorological Office
UTC	–	Universal Time Coordinated
WMO	–	World Meteorological Organization
WPR	–	Wind Profiling Radar

Content

Part I Synopsis

1 Introduction

Winds, a fundamental weather variable, dominate different scales of atmospheric phenomena, from microscale turbulence to mesoscale thunderstorms to synoptic scale weather fronts (Ahrens, 2009) (Figure 1.1). Wind information with high accuracy and good spatial coverage not only is essential for studying atmospheric dynamics and improving weather forecasts but also plays an important role in real-world applications, such as wind farm development and operation, aviation safety management, and natural disaster mitigation.

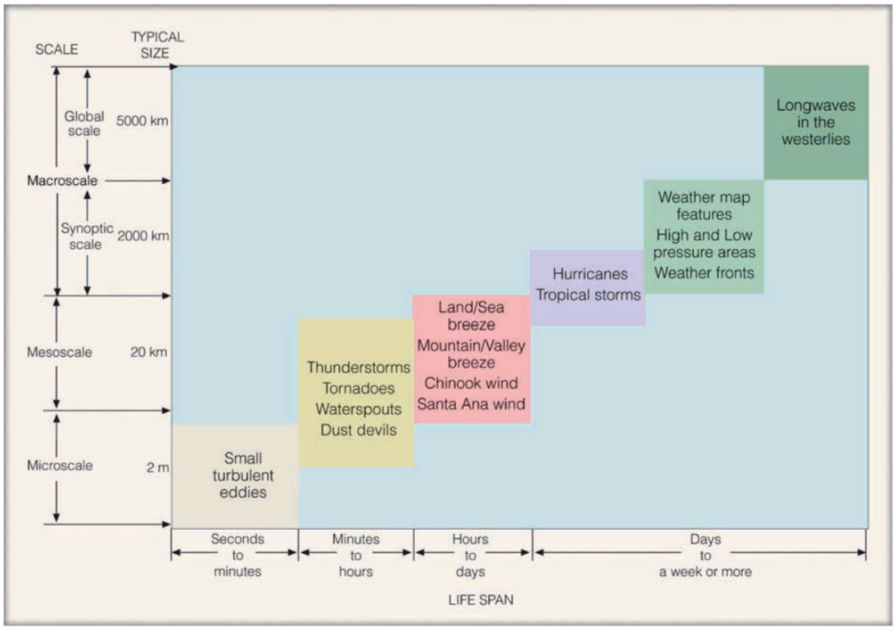

Figure 1.1: The scales of atmospheric motion with the phenomenon's average size and lifespan. (Because the actual size of certain features may vary, some of the features fall into more than one category). From Ahrens (2009) with permission for use.

1.1 Numerical weather prediction for wind forecasts

With the development of computer technology, numerical weather prediction (NWP) has become a powerful tool for atmospheric simulation and weather forecasting, including winds. The working principle of NWP is to use current atmospheric conditions to obtain future atmospheric states by solving a set of physics-based equations that govern atmospheric motion and evolution (Pu & Kalnay, 2018). The primitive equations involve momentum conservation (i.e., Newton's second law of motion), heat conservation (i.e., the first law of thermodynamics), mass conservation (i.e., continuity equation), moisture conservation, and the equation of state (i.e., ideal gas law), which forecasts the fundamental parameters of the atmosphere, including

wind components, temperature, total water mixing ratio, air density, and pressure. Small-scale physical processes, such as cloud microphysics and precipitation, which cannot be resolved in model grid boxes, are described through parameterization schemes.

To start an NWP model, initial values describing a recent atmospheric state are indispensable and are estimated through data assimilation, a technique that integrates the latest weather observations and previous short-term forecasts to better estimate the current atmospheric state. As indicated by Lorenz (1963), nonlinear dynamical equations are sensitive to initial conditions, which implies that small errors in the initial conditions can result in significant deviations from the actual weather as the forecast leads. Because the initial conditions are never perfect, the forecast skill decreases with increasing forecast length (Stull, 2017a).

Global and regional NWP models have been employed for wind forecasting. Global models are primarily used to generate medium-range wind forecasts, typically up to 15 days in advance, and climate projections with relatively coarse temporal and spatial resolution (Pu & Kalnay, 2018). For example, the operational medium-range forecasts from the European Centre for Medium-Range Weather Forecasts Integrated Forecasting System (ECMWF IFS) have a grid spacing of approximately 9 km.

Regional models aim to provide forecasts for limited domains of interest with an increased spatial resolution, which is usually three or more times higher than that of global models. The higher resolution allows them to resolve smaller-scale circulations, such as mountain and valley breezes. In addition to the initial conditions, running regional models requires lateral boundary conditions at the edges of the domains at regular time intervals, which are usually provided by the forecasts from coarse global models (Pu & Kalnay, 2018). Because the evolving boundary conditions will eradicate the value of the initial conditions with time, regional models are usually used to generate wind forecasts for a short period, typically 1–3 days ahead (Pu & Kalnay, 2018). More detailed wind forecasts from regional models are not only a part of operational weather forecasts but can also serve as inputs for other wind-related applications. For instance, in the wind energy sector, the wind predicted by regional models is an important ingredient of wind power predictions and wind farm operations, particularly in complex terrains and coastal regions (Prósper et al., 2019).

1.2 Wind measurements

As mentioned in Section 1.1, the performance of NWP models is strongly determined by the initial and boundary conditions, which are partly associated with observations. Moreover, understanding atmospheric dynamics also requires high-quality and high-coverage observations. Figure 1.2 depicts the Global Observing System (GOS) integrated by the World Meteorological Organization (WMO). Considering the scope of this study, the focus is on wind measurements.

According to measurement platforms, wind observations can be classified into three categories: surface-, flight-, and satellite-based wind measurements.

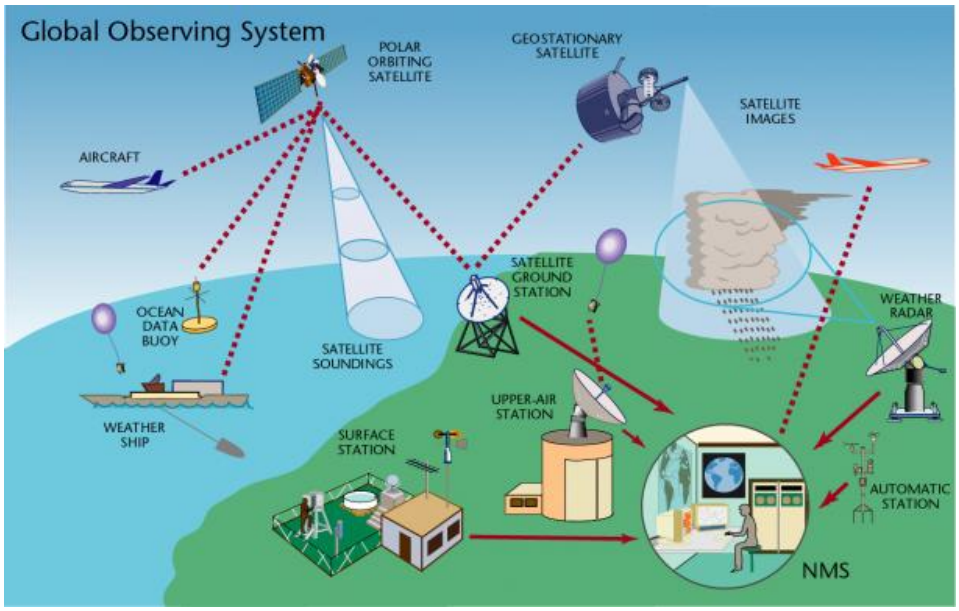

Figure 1.2: Global Observing System. From WMO (2022).

Surface-based wind measurements are primarily obtained from weather stations on land, buoys, ships, and ground-based wind profiling radars (WPR). Anemometers installed at weather stations and buoys are the conventional methods for measuring near-surface winds. Approximately 11,500 weather stations are widely distributed over land, while the moored buoys with wind measurements are mainly located in tropical oceans and coastal regions (Ingleby, 2023; WMO, 2022). Ships also provide voluntary wind measurements. In addition to in situ measurements, ground-based WPR is a type of active remote sensing equipment that operates in the radio frequency band to detect wind speed and direction at different heights above the ground; wind retrieval is based on the Doppler shift phenomenon; WPRs can provide continuous wind measurements regardless of weather conditions (Lehmann & Brown, 2021).

Flight-based wind measurements mainly include rawinsonde observations and wind measurements from aircraft. A rawinsonde is used to obtain the wind speed and direction in the upper air (up to approximately 35 km) by tracking the position of a balloon-borne radiosonde during flight using the global positioning system or a radio direction finder. There are about 1,300 radiosonde stations worldwide, most of which provide observations twice per day at 00:00 UTC and 12:00 UTC (National Oceanic and Atmospheric Administration, 2023). Another important type of upper-air wind observation is the global Aircraft Meteorological DAta Relay (AMDAR) programme initialized by the WMO (2022). Normally, the AMDAR programme provides more than 700,000 high-quality observations every day, including wind speed and direction with positional and temporal information captured by sensors on aircraft during take-

off, cruise, and landing. However, aircraft wind observations depend on flight routes and are affected by the aviation industry. For example, during the COVID-19 pandemic, a significant decrease in commercial flights resulted in fewer measurements.

Satellite-derived wind data are another key component of wind information. Global ocean surface winds can be obtained from spaceborne active radar scatterometers and passive microwave radiometers based on wind-induced ocean roughness. For a scatterometer, wind speed and direction are determined by measuring the electromagnetic signals reflected or backscattered from the ocean surface to an instrument, such as the QuikSCAT satellite (Kramer, 2012). Wind information from a radiometer is derived based on microwave emissions from the ocean surface. Examples include WindSat for wind vector observations and Special Sensor Microwave/Imager for wind speed observations (Bettenhausen et al., 2006; Goodberlet et al., 1990). For winds in the upper air, Atmospheric Motion Vectors (AMVs) are estimated by tracking cloud or moisture movement using consecutive images captured by geostationary or polar-orbiting satellites. Then, with the help of model data for quality control and height assignment, cloud motion winds can be generated (Forsythe, 2008). However, AMV products only partially fill the gaps in wind measurements in the upper atmosphere because they only provide wind information at a few levels, and the height assignment may contain errors (Salonen et al., 2015).

The above-mentioned wind formation is not only useful for studying atmospheric dynamics but also a great source for feeding the NWP models to initialize the atmospheric state.

In addition to the GOS measurements, wind profiles are captured by wind masts with sensors (e.g., anemometers) installed at different heights up to about 250 m or even higher. Wind masts are typically built for planetary boundary layer (PBL) studies or wind resource assessments before wind farm construction. In addition to wind masts, wind information can be detected using a ground-based light detection and ranging device, referred to as lidar, that uses the optical Doppler effect and has a maximum detection range of up to 10 km in the horizontal plane. With the advantages of easy installation and high vertical and temporal resolutions, ground-based lidars are primarily used for wind resource assessments, power curve testing, turbulence characterization, wind turbine wake measurements, and airport wind shear detections (Liu et al., 2019). However, except for a few research lidars, most operational wind lidars cannot reach a detection height of more than 300 m.

Although winds from the surface to the upper-level atmosphere have been detected using various techniques, significant gaps remain in the distributed wind profile measurements, particularly in regions such as the oceans, tropics, and Southern Hemisphere (Stoffelen, Benedetti, et al., 2020; WMO, 2020). These limitations in data availability hamper our understanding of atmospheric dynamics and affect the performance of NWP models.

1.3 Aeolus Mission

Aiming to address the wind profile deficiency in the GOS, the European Space Agency (ESA) launched the Aeolus satellite in August 2018 (Straume-Lindner et al., 2021). The Aeolus mission is part of the ESA's Earth Explorer programme that aims to observe different fields of the Earth's system using cutting-edge technologies. Owing to the Atmospheric LAser Doppler INstrument (ALADIN), a state-of-the-art direct-detection Doppler wind lidar (DWL), and a sun-synchronous polar orbit, Aeolus became a pioneering satellite mission to capture wind profiles on a global scale. It travelled from south to north (ascending orbits) and across the Equator at 18:00 local time (LT), referred to as the ascending node. Conversely, it had the descending node at 06:00 LT when travelling from north to south (i.e., descending orbits). It took about 12 hours to sample the global winds by around 8 orbits (Figure 1.3).

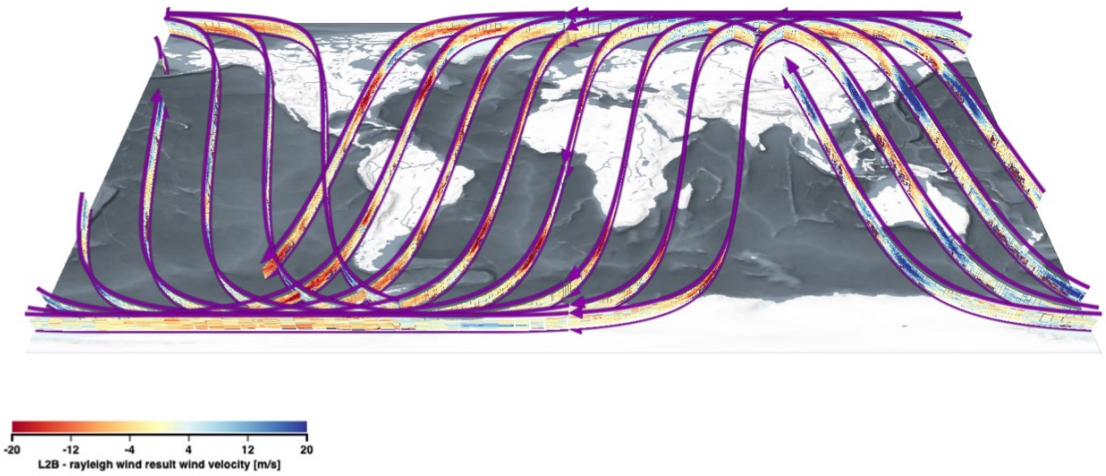

Figure 1.3: Aeolus observation coverage during a 12-hour period from 00:00 UTC to 12:00 UTC on 7 February 2021. Figure produced by using VirES for Aeolus.

The DWL onboard the Aeolus consisted of two laser transmitters, referred to as flight model A (FM-A) and flight model B (FM-B), a very big telescope, and a two-channel receiver (Figure 1.4 (a)). The working principle of the DWL is based on the light scattering by the atmosphere and the Doppler effect. Short powerful light pulses were emitted by an ultraviolet laser system at a wavelength of 355 nm down into the Earth's atmosphere. Then, the telescope captured the backscattered signal from the atmosphere and sent it to the receiver for analysis (Andersson et al., 2008). The receiver had two separate detection channels, Rayleigh and Mie. The Rayleigh channel was designed to detect light scattering from air molecules (i.e., oxygen and nitrogen) that have diameters (0.3–0.4 nm) smaller than the laser light wavelength, and the Mie channel was used to detect light scattering from particulates (i.e., cloud droplets, dust, and aerosols) with diameters (usually >1 μm) larger than the wavelength of the laser light (Calvert, 1990; Ingmann & Straume, 2016; Vallejos-Burgos et al., 2018; Wallace & Hobbs, 2006).

(a) 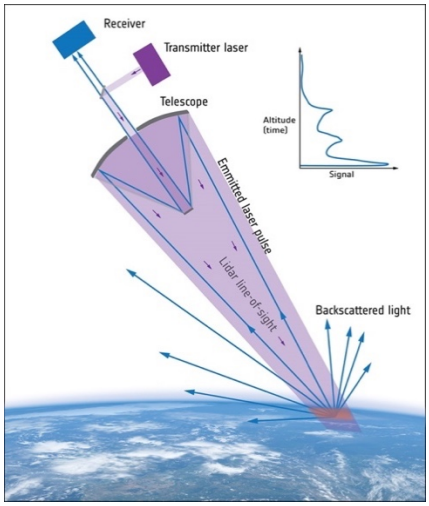

(b) 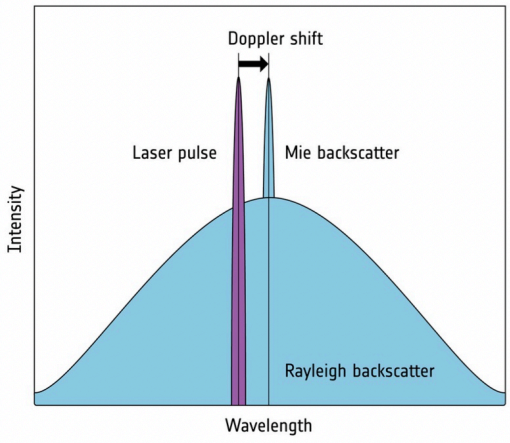

Figure 1.4: (a) Concept of DWL instrument; (b) Schematic view of the backscatter spectrum of Rayleigh-scattering and Mie-scattering, as compared with the emitted laser pulse. From Ingmann and Straume (2016). Credit: ESA/ATG medialab.

According to the Doppler shift, the frequency of the backscattered light is altered in relation to the speed of the 'scatterers' moving with the wind (Tan et al., 2008):

$$\Delta f = -\frac{2v_{LOS}}{\lambda_0} \tag{1.1}$$

where $\lambda_0$is the laser wavelength (355 nm), and v_{LOS} is the wind speed along the line-of-sight (LOS).

By measuring this small frequency change, the winds are derived along the LOS of the laser beam that is perpendicular to the flight direction at a 35° off-nadir angle on the night side of the Earth. Then, by converting the LOS winds into horizontal winds, a horizontal line-of-sight (HLOS) wind component is obtained. Because the azimuth angles of the Aeolus are around 260° during ascending orbits and around 100° during descending orbits (Figure 1.5), the HLOS winds are approximately in an east-west direction for most parts of the orbits (Andersson et al., 2008). The altitude of the measured wind can be calculated from the flight altitude and time between emitting the light pulse and receiving the backscattered signal. Each wind profile is defined by 24 vertical range bins from near the surface to up to a height of approximately 30 km, the settings of which depend on the observation requirements and the characteristics of atmospheric circulation in different regions and seasons (ESA, 2020).

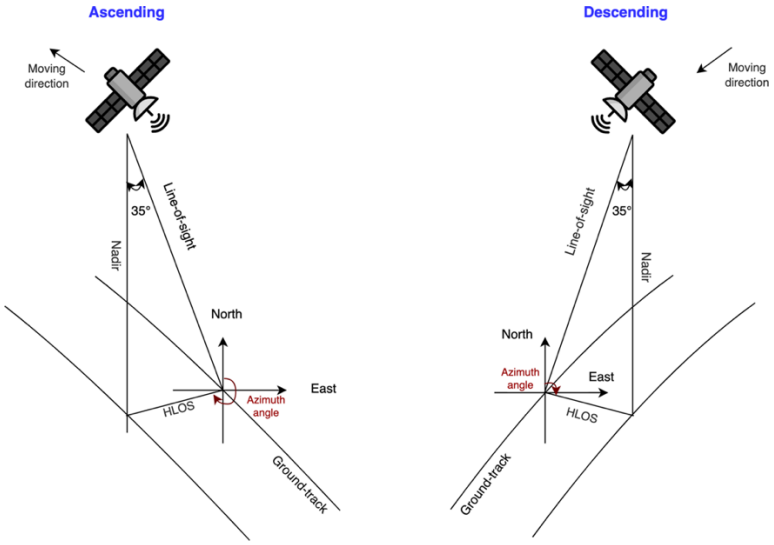

Figure 1.5: Geometry of Aeolus wind measurements. From **Article I** (Zuo et al., 2022).

The geo-located and fully consolidated HLOS wind observations form the Aeolus Level-2B (L2B) product, the main product of the Aeolus mission (Ingmann & Straume, 2016). Figure 1.6 gives an example of the Aeolus wind profiles from the L2B product over the Tibetan Plateau on 06 May 2020. Positive HLOS wind velocity is defined as the condition where the air is moving away from the instrument, thus positive HLOS winds (in blue) represent easterlies during a descending orbit, and conversely, negative HLOS winds (in red) indicate westerlies. The range bin setting changed along with the Aeolus descending orbit from extratropical to tropical regions. The Tibetan Plateau is the region with no data below an altitude of approximately 6 km. More Rayleigh-clear samples are available than Mie-cloudy samples since the measurement of the Mie channel depends on clouds.

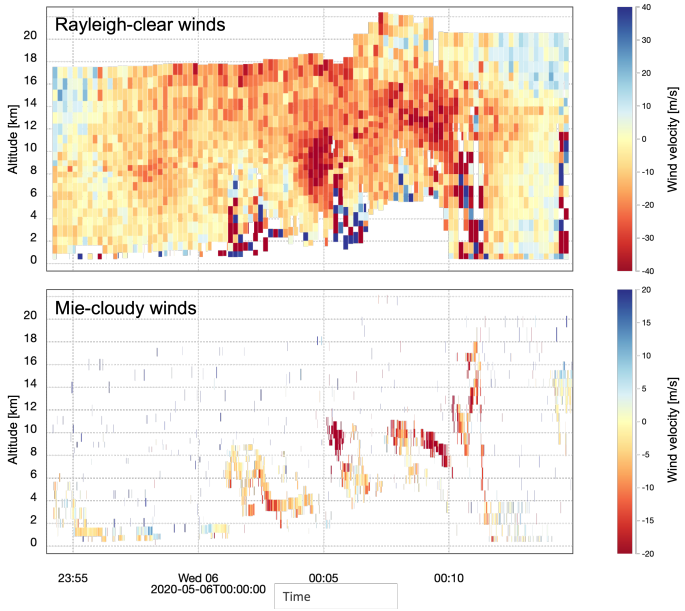

Figure 1.6: An example of Aeolus L2B wind profiles on 06 May 2020 during a descending orbit across the Tibetan Plateau. Produced by using VirES for Aeolus and adapted by the author.

According to the mission requirements (Ingmann & Straume, 2016), the data quality of Aeolus HLOS winds aims to achieve a bias within 0.7 m s^{-1} for the whole vertical range. The precision aims to be smaller than 1 m s^{-1} in the PBL and 2.5 m s^{-1} in the free troposphere. For the stratosphere, the desired precision is better than 3 m s^{-1} between 16 km and 20 km, and 3–5 m s^{-1} above 20 km (Table 1.1).

Table 1.1: Quality requirements for Aeolus HLOS wind observations. Information from Ingmann and Straume (2016).

	PBL	**Free Troposphere**	**Stratosphere**	
Height range	0-2 km	2-16 km	16-20 km	20 – 30 km
Bias	0.7 m s^{-1}			
Precision	1 m s^{-1}	2.5 m s^{-1}	3 m s^{-1}	3-5 m s^{-1}

Since its successful launch, significant efforts have been made to calibrate and validate the Aeolus winds, and the data processing algorithm has been constantly improved. The Aeolus wind products are marked or re-processed using different baseline versions (Baseline 11 was the latest version available at the initial stage of this PhD study). The mission timeline is shown in Figure 1.7. The mission initially operated with FM-A, but due to the unexpected laser pulse energy degradation, it switched to FM-B in June 2019 and then switched back to FM-A in late-2022, until the end of the mission operations in April 2023 (Krisna & Wernham, 2023). Despite

the signal loss, the operation of the Aeolus mission lasted for nearly five years, which is more than the designed lifetime of three years. Figure 1.7 also indicates the timing when Aeolus observations were operationally used by four biggest meteorological services centres in Europe, including the ECMWF, Deutscher Wetterdienst (DWD), Météo-France, and United Kingdom Meteorological Office (UK Met Office) (ESA, 2021b).

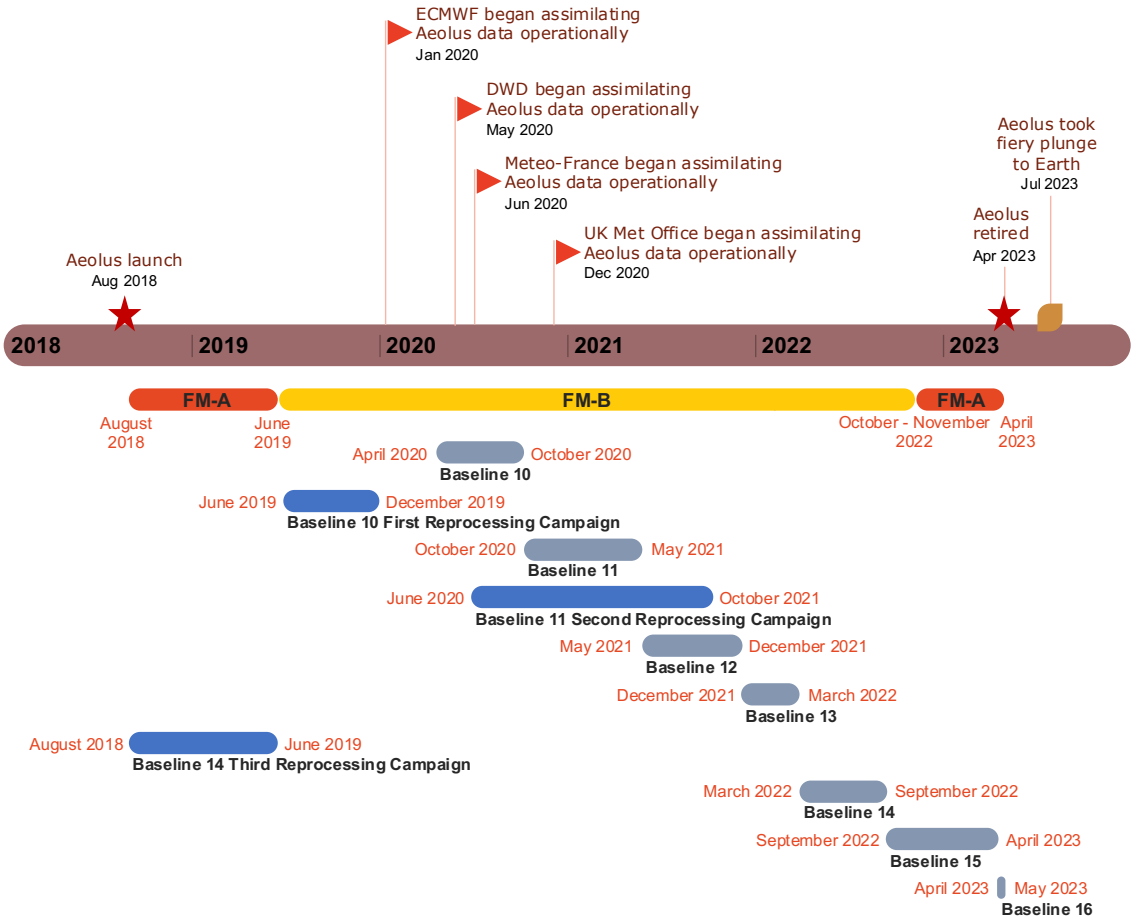

Figure 1.7: Aeolus mission timeline, data products based on different processing baselines, and the onsets of operational assimilation of Aeolus data at different weather centers in Europe. Figure is created by the author based on the information from ESA (2021b, 2023a) and Krisna and Wernham (2023).

1.3.1 Aeolus wind error characteristics

During the Aeolus mission, observation-based validations were performed for various baselines in different regions. During the early stage of the mission, the evaluation for the baseline 2 product (November–December 2018) over the Atlantic Ocean shows that Aeolus has good precision, achieving 4.84 m s^{-1} and 1.58 m s^{-1} for Rayleigh-clear and Mie-cloudy winds,

respectively; the biases are relatively large at 1.5 m s^{-1} for Rayleigh-clear winds and 1 m s^{-1} for Mie-cloudy winds (Baars et al., 2020). With improved data processing algorithms, the M1-temperature-based bias is corrected, and daily updates of bias removal are implemented after Baseline 10 (Aeolus Data Innovation and Science Cluster (DISC), 2020). The validations for later baselines reveal that the overall biases for both Rayleigh-clear and Mie-cloudy winds are commonly smaller than the mission requirement (0.7 m s^{-1}), except for some special cases, such as for polar regions. However, because of the unexpected reduction in signal loss, the random errors are larger than expected, mainly ranging from 4 m s^{-1} to 8 m s^{-1} for Rayleigh-clear winds and from 2.0 m s^{-1} to 5 m s^{-1} for Mie-cloudy winds, most of which are much larger than the required precision of the mission (Belova et al., 2021; Ingmann & Straume, 2016; Iwai et al., 2021; Ratynski et al., 2023; Witschas et al., 2022).

Evaluations based on the departures between the Aeolus observations and ECMWF model background winds show similar results. For the second reprocessed Level-2B Baseline 11 data, the global daily average biases are close to zero for both Rayleigh-clear and Mie-cloudy winds during June 2019 – October 2020. However, the unexpected signal loss of the laser system leads to a gradual increase in the estimated random errors for Rayleigh-clear winds, rising from ~5 m s^{-1} to ~7 m s^{-1} during the study period, whereas Mie-cloudy winds are insensitive to this instrument problem, with stable random errors of ~3.5 m s^{-1} (Rennie & Isaksen, 2023).

1.3.2 Observing system experiments

Building upon calibration and validation work, the value of Aeolus wind profiles in NWP models has been assessed by observing system experiments (OSEs) at different weather forecast centers worldwide, including the ECMWF, National Oceanic and Atmospheric Administration (NOAA), DWD, Météo-France, UK Met Office, Environment and Climate Change Canada, and Korea Meteorological Administration (Borne et al., 2023; Garrett et al., 2022; Laroche & St-James, 2022; Lee et al., 2023; Pourret et al., 2022; Rennie & Isaksen, 2023). OSEs were performed by running the models under different scenarios with and without Aeolus data assimilation, in turn determining the impact of these novel wind profiles on weather forecasts.

Verifications based on OSEs with different global NWP models demonstrate that Aeolus wind assimilation can improve wind vector forecasts by up to ~4%. This improvement is particularly significant in the upper troposphere and/or lower stratosphere over the tropical regions and in the Southern Hemisphere for the forecasts of up to 120 h (Garrett et al., 2022; Laroche & St-James, 2022; Pourret et al., 2022; Rennie et al., 2021). In the Northern Hemisphere, positive contributions to wind forecasts are mainly obtained in the polar troposphere (Laroche & St-James, 2022; Lee et al., 2023; Rennie et al., 2021). In addition to global models, wind speed and direction forecasts from the AROME-Arctic mesoscale model also benefit from Aeolus wind assimilation by applying a footprint operator (Mile et al., 2022).

1.3.3 The value of Aeolus

The added values and potentials of the Aeolus wind profiles are summarized as follows:

- Capture large-scale air motion (Banyard et al., 2021).
- Enhance understanding of atmospheric dynamics.
- Improve the performance of NWP models for operational forecasts, including extreme weather (Garrett et al., 2022), and climate events, such as monsoons and El Niño (Borne et al., 2023).
- By improving wind forecasts from NWP models, Aeolus can help estimate the movement and concentration of air pollutants, such as volcanic ash plume dispersion (Amiridis et al., 2023).
- Wind profiles from Aeolus can be used for model calibration and validation, particularly in regions lacking conventional wind observations.

These values can greatly contribute to daily activities and support decision-making in various industries, such as aviation, renewable energy, and ocean shipping, which eventually enhance human welfare.

1.4 Motivation and research goal

Wind information is crucial for different applications in wind energy. Wind resource assessments rely heavily on wind observations and numerical simulations. Moreover, because wind power is proportional to the cube of wind speed (Stull, 2017b), high-quality wind forecasts can help reduce the uncertainties in wind power predictions, which is important for the optimization of multi-energy system operations. Additionally, accurate wind information benefits wind turbine design as well as the control and operations of wind farms, particularly in response to extreme wind events and weather conditions (Pryor & Barthelmie, 2021).

The accuracy of wind simulations and forecasts for the surface layer is not only highly dependent on wind measurements at the same layer (i.e., weather stations, scatterometer winds, and ground-based wind lidar) but is also affected by wind information at the upper levels. As the studies indicate, a better estimation of the upper-level atmospheric initial state can benefit the tropospheric circulation in the NWP models through downward propagation (Charlton et al., 2004; Christiansen, 2001; Kodera et al., 1990), thus improving medium- to long-range wind forecasts for the low-level atmospheres. Therefore, the novel wind profile observations provided by Aeolus open up the possibilities to improve wind forecasts for the lower troposphere, which in turn has the potential to aid wind energy applications.

Before investigating the potential of Aeolus wind profiles for the wind energy industry, it is important to understand their error characteristics on a global scale. Until the initial stage of this PhD project (late 2020 and early 2021), most observation-based validations of Aeolus winds focused on the Northern Hemisphere regions and some polar regions. The validations for the Southern Hemisphere were still very few (Figure 1.8) and needed to be complemented.

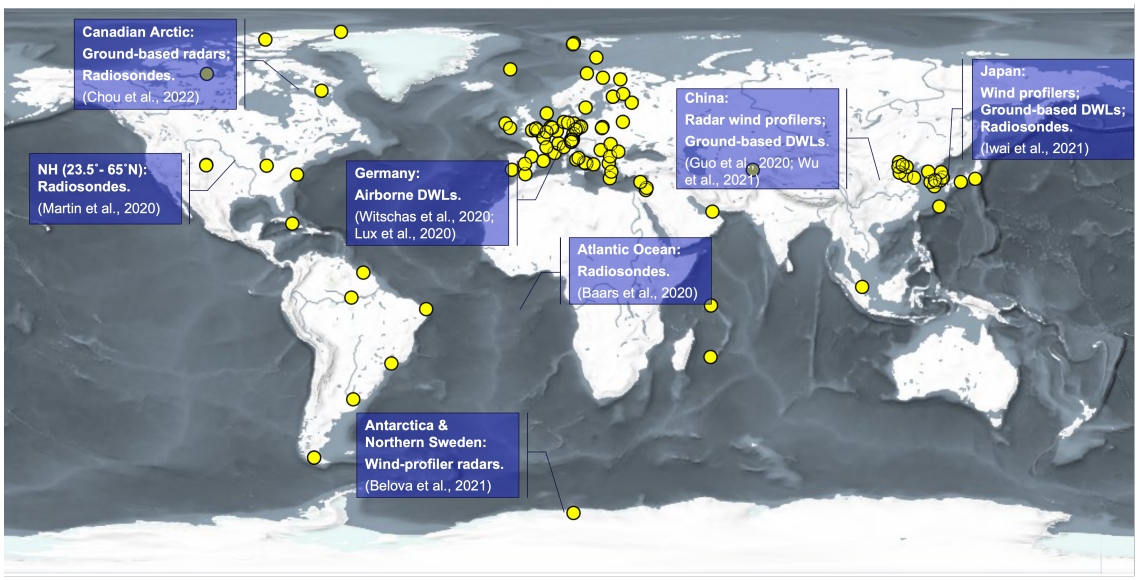

Figure 1.8: Geographical distribution of Aeolus validation/calibration sites (yellow dots) and the published evaluations based on observations until 2022. The background map produced by using VirES for Aeolus and adapted by the author.

Moreover, although Aeolus observations have been demonstrated to positively contribute to wind forecasts, most existing verifications are for latitudinal bands and pressure levels by taking model analysis as reference data (Garrett et al., 2022; Laroche & St-James, 2022; Lee et al., 2023; Rennie et al., 2021). The impact of the Aeolus data on the atmospheric surface layer in different geographical ocean regions remains unclear. In other words, the ocean regions that can benefit from Aeolus winds and those that Aeolus may degrade the wind forecasts remain unknown. Understanding this issue is conducive to generating high-resolution and high-quality wind information for limited areas, which is critical for offshore wind farm developments and operations worldwide. In particular, for the Southern Hemisphere, many offshore wind farms are being planned, such as in South America, Australia, and South Africa; however, model skills are, to some extent, limited by insufficient wind profile information. In addition, with the deployment of wind farms in high-latitude regions (Minin & Furtaev, 2019), it is worth investigating the impact of Aeolus on wind forecasts for these regions, where conventional wind profile observations are limited.

In light of the above, as a starting point, this PhD study aims to investigate the performance of Aeolus in wind profile detection and understand its geographical impact on near-surface wind forecasts.

2 Research Objectives, Hypotheses, and Thesis Structure

This section describes the three objectives of this PhD study together with the corresponding hypotheses and scientific articles, followed by the thesis structure.

2.1 Objective 1

The first objective is to evaluate the quality of Aeolus HLOS wind products. The analyses investigate:

- Whether systematic (bias) and random (precision) errors of Rayleigh-clear and Mie-cloudy winds achieve the mission requirements over Australia;
- Error characteristics of the Rayleigh-clear and Mie-cloudy winds as a function of height.

The hypothesis for **Objective 1** is:

- The bias and precision of the Aeolus wind products fulfill the mission requirements.

The results of Aeolus wind validation over Australia have been published in Atmospheric Measurement Techniques, see Appendix A.1, referred to as **Article I** (Zuo et al., 2022).

2.2 Objective 2

The second objective is to evaluate the impact of Aeolus wind assimilation on global sea surface wind forecasts geographically. This study aims to investigate the following:

- Whether Aeolus wind assimilation can benefit medium-range wind forecasts up to T+240 h for tropical Atlantic Ocean, Indian Ocean and Pacific Ocean;
- For global ocean, whether and over which regions Aeolus wind assimilation can reduce the wind component biases of short-range (within T+12 h) forecasts;
- For the global ocean, whether and over which regions Aeolus wind assimilation can improve short- and medium-range forecasts up to T+120 h.

The hypotheses for **Objective 2** are as follows:

- Aeolus wind assimilation improves medium-range wind forecasts for tropical oceans;
- Aeolus wind assimilation reduces the short-range forecast biases of wind components for each climatic region;

- Aeolus wind assimilation generally reduces the difference between observations and short- and medium-range ocean wind forecasts for each climatic region.

The evaluation for tropical oceans is a part of **Article II** (Zuo & Hasager, 2023) that has been published in Atmospheric Measurement Techniques (see Appendix A.2). The evaluation for the global ocean is presented in the manuscript attached in Appendix A.3, referred to as **Article III** (Zuo et al., 2023), that has been submitted to the Journal of Geophysical Research: Atmospheres and is currently under revision.

2.3 Objective 3

The third objective focuses on assessing the Aeolus' value for medium-range wind forecasts over high-latitude lands in both hemispheres. This study aims to explore the following:

- Whether Aeolus is able to improve the near-surface wind forecasts up to 240 h;
- Whether the impact of Aeolus on near-surface wind forecasts varies with seasons, Aeolus wind quality, and different wind speed categories.

The hypotheses for **Objective 3** are as follows:

- Aeolus wind assimilation improves medium-range near-surface wind forecasts for high-latitude lands in the Northern Hemisphere and Southern Hemisphere;
- The contribution of Aeolus to near-surface wind forecasts is sensitive to seasons, Aeolus wind quality, and different wind speed categories.

This study is presented in **Article II** (Zuo & Hasager, 2023); see Appendix A.2.

2.4 Thesis Structure

Section 3 introduces the data sets used for achieving the three objectives. Section 4 presents the methods and computational resources for data processing and analysis. Section 5 summarizes the main research findings for each objective. Section 6 concludes the study, followed by an outlook for future research in Section 7. Published articles and a submitted manuscript related to this PhD project are attached in **Part II Appendix**, which includes

Article I: Zuo, H., Hasager, C. B., Karagali, I., Stoffelen, A., Marseille, G.-J., & de Kloe, J. (2022). Evaluation of Aeolus L2B wind product with wind profiling radar measurements and numerical weather prediction model equivalents over Australia. Atmospheric Measurement Techniques, 15(13), 4107–4124. https://doi.org/10.5194/amt-15-4107-2022 [Published]

Article II: Zuo, H., & Hasager, C. B. (2023). The impact of Aeolus winds on near-surface wind forecasts over tropical ocean and high-latitude regions. Atmospheric Measurement Techniques, 16, 3901–3913. https://doi.org/10.5194/amt-16-3901-2023 [Published]

Article III: Zuo, H., Stoffelen, A., Rennie, M., and Hasager, C. B. (2023) The Contribution of Aeolus Wind Observations to ECMWF Sea Surface Wind Forecasts, submitted to Journal of Geophysical Research Atmospheres [In revision]

Note: **Article III** is currently under revision, and the results presented in the thesis and manuscript may differ from the final published version.

3 Data

3.1 Data for Aeolus wind validation

Section 3.1 introduces the data sets used to achieve **Objective 1**: Aeolus wind validation in Australia. Validation was performed for the Aeolus L2B baseline 11 HLOS wind product from October 2020 to March 2021, which was the latest available baseline version when performing this study. Wind profiling radar (WPR) measurements serve as the reference data, and wind predictions from the ECMWF model also assist in validation.

3.1.1 Aeolus Level-2B wind product

Aeolus L2B baseline 11 near real-time (NRT) HLOS winds were obtained from the ESA Aeolus Online Dissemination System at https://aeolus-ds.eo.esa.int/oads/access/ (ESA, 2021a). Wind measurements from the Rayleigh and Mie channels in the Aeolus L2B product are categorized as Rayleigh-clear, Rayleigh-cloudy, Mie-clear, and Mie-cloudy, based on signal-to-noise ratios (de Kloe et al., 2021). Among them, Rayleigh-clear and Mie-cloudy winds are the most reliable types, because a clear sky with little or no contamination from Mie scattering favors wind detection from the Rayleigh channel, and strong backscattering from particulates is required for the wind measurements in the Mie channel (Rennie et al., 2021). Additionally, only Rayleigh-clear and Mie-cloudy winds were assimilated into NWP models for operational weather forecasts and Aeolus impact experiments (Rennie et al., 2021). Hence, the validation focuses on these two types of wind products.

The horizontal resolution along the ground track at the observation scale is around 87 km for Rayleigh-clear winds and around 15 km for Mie-cloudy winds, but locally, this length might be shorter due to scene classification into clear and cloudy conditions (Ingmann & Straume, 2016). Vertically, each profile has 24 range bins, with thicknesses ranging from 250 m to 2 km (ESA, 2020). To better capture atmospheric circulation across different climate zones, range bin settings vary geographically and seasonally depending on measurement requests. Australia crosses two range bin setting regions: the tropical region (30° S–30° N) and the extratropical region (30–60° S), where range bin settings differ in measurement heights and range bin thickness (ESA, 2020).

Quality control was performed prior to validating Aeolus winds. The HLOS winds with a validity flag of 0 were removed. Moreover, Rayleigh-clear and Mie-cloudy winds with estimated errors larger than 8 m s^{-1} and 4 m s^{-1} were screened out, respectively (Martin et al., 2021; Rennie & Isaksen, 2023).

3.1.2 Wind profiling radar measurements

The WPR is a ground-based radar system that remotely detects the vertical profiles of wind vectors up to approximately 20 km in height (Dolman et al., 2018). WPR wind measurements, rather than lidar winds, were used as the referenced data for Aeolus wind validation because the maximum detection height of most operational wind lidars is 250–300 m above the ground, which leads to only a few match-ups available for validation after collocating with the Aeolus wind profiles (Angelou et al., 2019).

The WPR network in Australia, primarily operated by the Australian Government Bureau of Meteorology, comprises two types of WPR operating at 55 MHz (Dolman et al., 2018). One is the boundary layer profilers (BLPs) that utilize the spaced antenna full correlation analysis technique with maximum detection ranges of 7 km for the low mode and 14 km for the high mode. The other is the stratospheric tropospheric profilers (STPs) that utilize the Doppler beam swinging technique and can detect winds up to ~8 km in height for the low mode and ~20 km in height for the high mode (Dolman et al., 2018). Table 3.1 provides technical information on these two types of WPRs. Wind measurements from WPRs have been quality-controlled and bias-corrected (Dolman et al., 2016). The 30-minute averaged wind vectors were obtained from the Centre for Environmental Data Analysis archive (Met Office, 2008).

Table 3.1: Technical information of boundary layer profilers and stratospheric tropospheric profilers. Information from Dolman et al. (2016).

Parameter	BLPs	STPs
Operating frequency	55 MHz	55 MHz
Power	12 kW	80 kW
Antenna configuration	27 Yagi antennas, arranged in 3 groups of 9	144 Yagi antennas, arranged in a 12 x 12 square grid.
Radar receiver	Three coherent (complex) radar receiver channels	One coherent (complex) radar receiver channel
Analysis mode	Full Correlation Analysis	Doppler
Measurement mode	Low/High	Low/High
Maximum detection range	7 km/14 km	8 km/20 km
Standard range resolution	100 m/250 m	250 m/500 m

3.1.3 Auxiliary Meteorological Data

Predicted winds at Aeolus observation locations from Aeolus auxiliary meteorological data (AUX_MET) files were obtained to validate the Aeolus winds through triple collocation (TC) analysis, an advanced data validation method that requires three independent data sets (Vogelzang & Stoffelen, 2012). The TC method is introduced in Section 4.3 with more details.

AUX_MET is produced by the fifth-generation ECMWF IFS with a model resolution of $T_{co}1279/L137$, corresponding to a horizontal grid spacing of approximately 9 km (Straume-Lindner, 2018). Notably, the effective resolution of an NWP model in a free atmosphere is generally 7–10 times the grid distance (Skamarock, 2004). Therefore, the ECMWF IFS model has an effective resolution of about 90 km. In terms of data quality, ECMWF winds typically differ from radiosonde winds by 2–3 m s^{-1} (Ingleby, 2016).

Wind information from the AUX_MET files, instead of the reanalysis data set or operational model forecasts, was employed to ensure the independence between the observations and model-generated winds. This is because the Aeolus winds were not incorporated into the model to produce the AUX_MET. Additionally, despite the assimilation of WPR observations into the model, the dependence of the predicted winds on the observations weakens as forecast time increases. Thus, the Aeolus L2B winds, WPR observations, and predicted winds from AUX_MET can be considered independent of each other.

3.2 Data for surface wind forecast evaluation

The data sets introduced in Section 3.2 were used to evaluate the impact of Aeolus wind assimilation on surface wind forecasts in different regions, corresponding to **Objectives 2** and **3**.

3.2.1 Observing system experiments at ECMWF

The evaluations for understanding the impact of Aeolus on surface wind forecasts were based on the OSEs conducted by the ECMWF (Rennie & Isaksen, 2023). The employed OSEs include a control experiment without Aeolus data assimilation (no Aeolus) and an experiment with the 2nd reprocessed Aeolus L2B baseline 11 data assimilated during the FM-B period from June 2019 to October 2020 and NRT baseline 11/12 data assimilated from October 2020 to September 2021. The applied IFS code version is CY47R2 with an atmospheric outer loop resolution of $T_{co}639$, corresponding to a horizontal grid spacing of ~18 km. A four-dimensional variational data assimilation (4D-Var) technique was used to generate analysis by combining a background forecast and observations over a 12-hour assimilation window. For the experiment with Aeolus data assimilation, only Mie-cloudy winds were assimilated below 850 hPa, which were very few and mainly distributed over the ocean regions with stratocumulus clouds occurring (Wood, 2012), as shown in Figure 3.1; above 850 hPa, both Rayleigh-clear and Mie-

cloudy winds were assimilated into the model (Rennie & Isaksen, 2023). Technical information about the OSE setup, including quality control decisions, can be found in Rennie and Isaksen (2023).

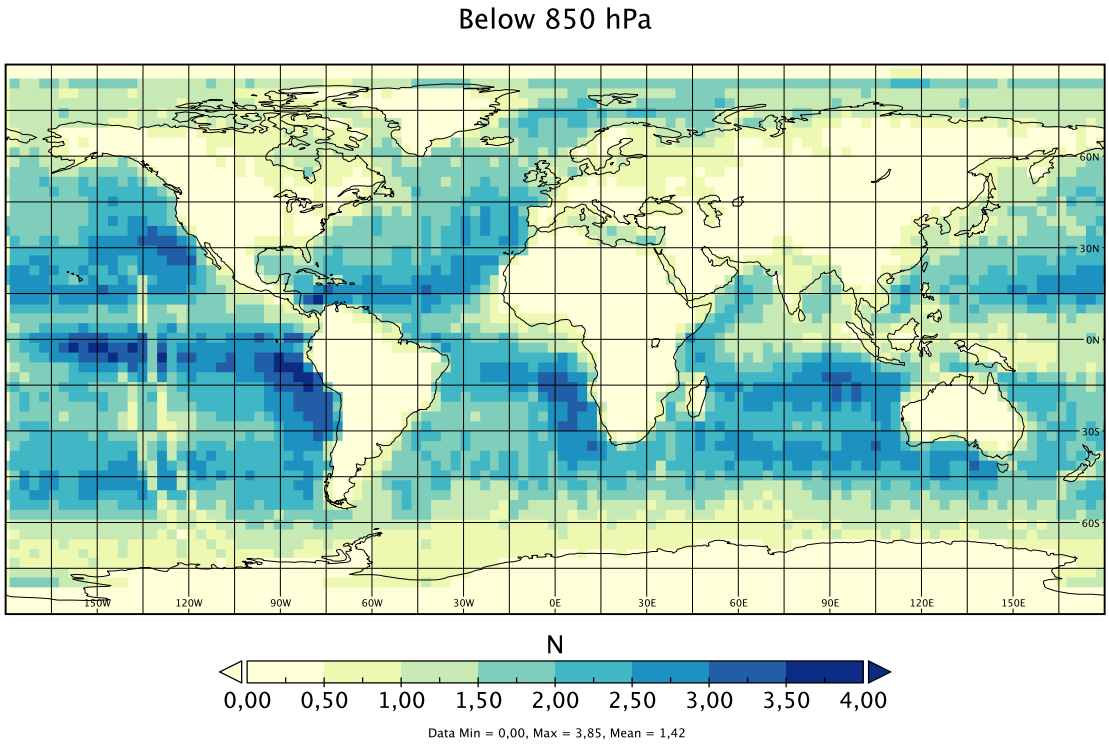

Figure 3.1: The averaged number of Aeolus winds assimilated per cycle below 850 hPa from the forecasts based on the 00:00 UTC and 12:00 UTC analysis during July 2019–June 2020.

The first-guess departures of wind components between the advanced scatterometer (ASCAT) measurements and the model background forecasts were used to evaluate Aeolus' impact on the short-range (within 12 hours) ocean wind forecasts. Moreover, wind component forecasts at a height of 10 m with a 24-h time interval were used to evaluate the medium-range forecasts for both ocean and high-latitude regions. The above-mentioned OSE data were obtained from the ECMWF Meteorological Archival and Retrieval System (MARS) (ECMWF Research Department, 2022).

3.2.2 Satellite scatterometer winds

Scatterometers are active microwave sensors usually equipped with low Earth-orbiting satellites to determine the wind speed and direction over the Earth's water bodies (EUMETSAT, 2022). Wind derivation is based on Bragg scattering and sea roughness by measuring the electromagnetic backscatter from wind-generated ocean ripples called gravity-capillary waves. To evaluate the impact of Aeolus on global ocean wind forecasts, 25-km swath grid wind

products from the ASCAT on a series of Meteorological Operational (Metop) satellites and from the Haiyang-2B (HY-2B) satellite were used as references (EUMETSAT SAF on Ocean and Sea Ice, 2009, 2021).

ASCAT is a dual-swath fan beam scatterometer onboard Metop-A (2006–2021), Metop-B (2012–2024), and Metop-C (2018–2027) satellites that follow a sun-synchronous orbit with 9:30 LT for the descending node and 21:30 LT for the ascending node (ESA, n.d.). The instrument consists of two sets of three antennas that provide dual-swath observations with each of about 550 km in width and a gap of about 670 km along the ground track (Figure 3.2 (a)) (EUMETSAT, 2022). Operating at a C-band frequency (5.255 GHz), the quality of ASCAT-derived winds is not very sensitive to rainy weather but is compromised at high wind speeds (>16 m s^{-1}) (Wang et al., 2020). The wind speed of the 25-km wind product is free of bias, and the standard deviations of differences based on the o-b statistics, i.e., ASCAT observations minus ECMWF background winds, are about 1.4 m s^{-1} for wind components (Ocean and Sea Ice Satellite Application Facilities/EUMETSAT Advanced Retransmission Service Winds Team, 2021); and the error standard deviations (ESD) for wind components are about 0.4 m s^{-1} in the spatial representation of the scatterometers (Vogelzang & Stoffelen, 2021).

HY-2B is part of China's marine satellite series dedicated to marine environment monitoring and investigation with observations of sea surface wind, wave height, sea surface height, sea surface temperature, and more (National Satellite Ocean Application Service, n.d.). Launched in October 2018, HY-2B operates in a sun-synchronous orbit with 06:00 LT for the descending node and 18:00 LT for the ascending node. The onboard instrument is a Ku-band (13.3 GHz) rotating pencil beam scatterometer that detects the wind speed and direction within a single swath of 1,700 km in width along the ground track (Figure 3.2 (b)). Unlike a C-band scatterometer, the wind retrieval of a Ku-band scatterometer is affected by rain contamination (S. Liu et al., 2022). For the 25-km swath grid product, the wind speed bias is about 0.11 m s^{-1} by comparing with the ECMWF stress-equivalent background winds at 10-m height, and the standard deviations of differences for the wind components are about 1.2 m s^{-1}; the ESDs are about 0.5 m s^{-1} for the wind components (OSI SAF Winds Team, 2021).

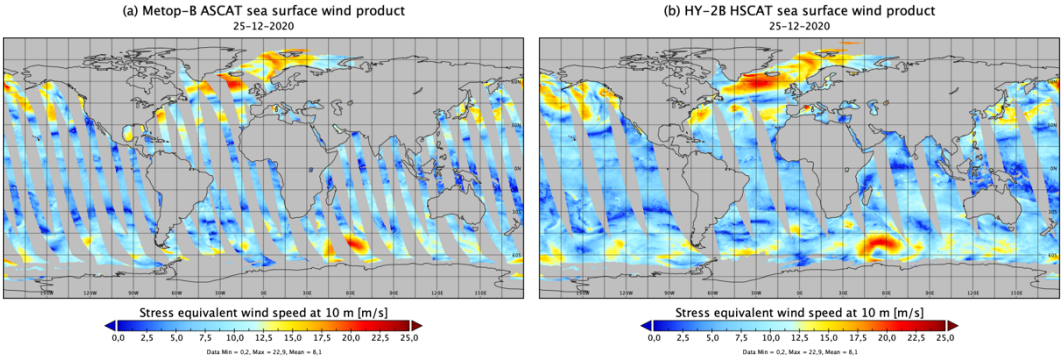

Figure 3.2: Examples of (a) ASCAT and (b) HSCAT stress equivalent wind speed at 0.25 degrees based on 25 km scatterometer swath observations during ascending orbits on 25 December 2020. Figure generated using the data retrieved from E.U. Copernicus Marine Service Information, https://doi.org/10.48670/moi-00182.

3.2.3 In situ wind measurements

To assess the impact of Aeolus on the tropical oceans, wind measurements from moored buoys over the tropical Atlantic, Indian, and Pacific oceans were obtained from the Global Tropical Moored Buoy Array (Pacific Marine Environmental Laboratory, n.d.). During the study period, 11, 9, and 55 buoys were available in the tropical Atlantic, Indian, and Pacific Oceans, respectively. Winds from different buoys are provided at their sensor heights of 3.5 m or 4 m with a temporal resolution of 10 min or 1 h. All measurements were quality controlled, and the 10-min winds were averaged to the hourly winds to ensure that all measurements have the same temporal resolution.

To assess the contribution of Aeolus to wind forecasts over high-latitude regions (> 60° N and > 60° S), surface wind observations from land weather stations were employed as reference data, which were obtained from the global hourly Integrated Surface Database (National Centers for Environmental Information, n.d.).

The geographical distribution of the buoy and weather stations is shown in Figure 3.3.

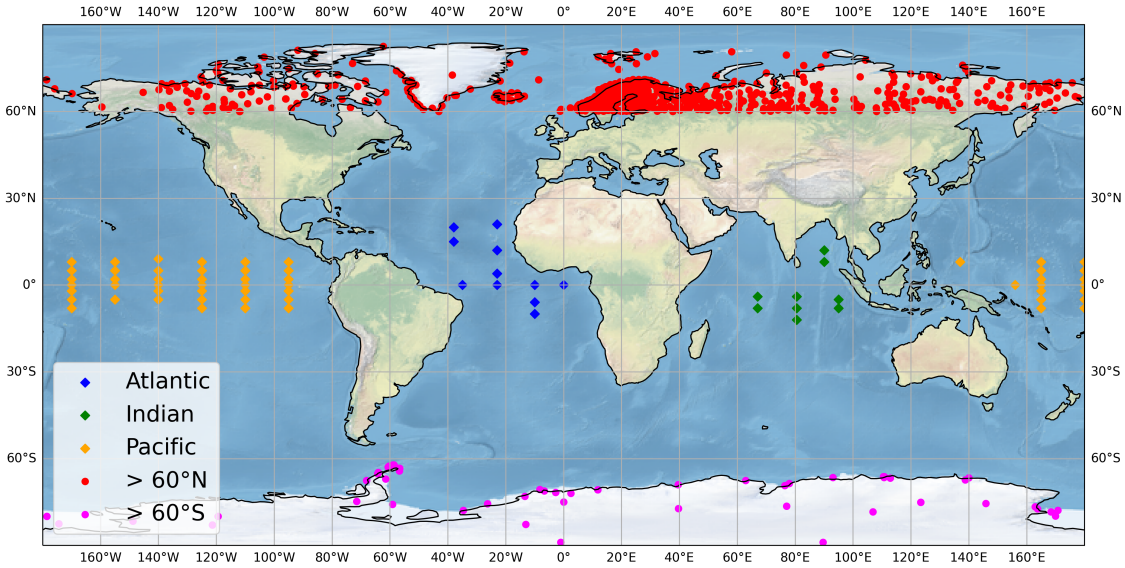

Figure 3.3: The geographical distribution of moored buoys in the tropical oceans and weather stations in the high latitude > 60° N and high latitude > 60° S (background image made with Natural Earth. Free vector and raster map data at naturalearthdata.com). From **Article II** (Zuo & Hasager, 2023).

4 Methodology

4.1 Wind collocation and interpolation

4.1.1 Wind profile collocation

Before quantifying the Aeolus wind errors, the WPR measurements (see Section 3.1.2) and ECMWF-predicted winds from AUX_MET files (see Section 3.1.3) were collocated with the Aeolus wind profiles (see Section 3.1.1). For WPR-Aeolus collocations, considering the WPR site locations and following the existing WPR-based study, the distance between the Aeolus ground tracks and WPR sites should not exceed 75 km (Zhang et al., 2016; Guo et al., 2021). According to this criterion, six WPR sites were available over Australia, with Ceduna and East Sale in the extratropics and Carnarvon, Tennant Creek, Longreach, and Cairns in the tropics (Figure 4.1). The closest Aeolus L2B wind profiles to the WPR sites were then extracted and collocated with the WPR wind profiles at the closest timing to Aeolus observations. For the AUX_MET-Aeolus collocation, the ECMWF-predicted winds were selected from the profiles nearest to each Aeolus L2B wind profile.

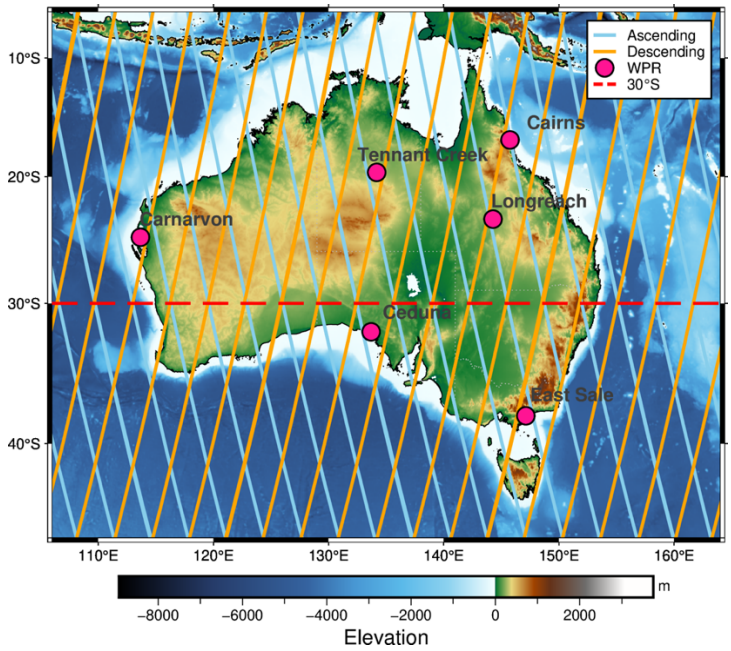

Figure 4.1: Location of wind profiling radars (WPRs) and Aeolus ground tracks over Australia. The pink marks on the map represent the sites of WPRs used in this study, and the blue and orange lines indicate the Aeolus ground tracks for ascending and descending orbits, respectively. The red dashed line at 30° S is the boundary between the tropics and extratropics. Shading with different colors represents the earth relief. The elevation data were accessed, and

the map was created by the authors using PyGMT (Tozer et al., 2019; Uieda et al., 2021; Wessel et al., 2019). From **Article I** (Zuo et al., 2022).

The wind information from the WPRs and AUX_MET consists of zonal (u) and meridional (v) wind components, which were converted to HLOS winds according to Eq. (4.1):

$$HLOS = -u_{Ref} \sin A - v_{Ref} \cos A \tag{4.1}$$

where A is the Aeolus azimuth angle, and *Ref* stands for either WPR or AUX_MET.

To vertically collocate with Aeolus winds, the converted WPR and AUX_MET HLOS winds between the top and bottom altitudes of each Aeolus vertical bin were averaged (Figure 4.2).

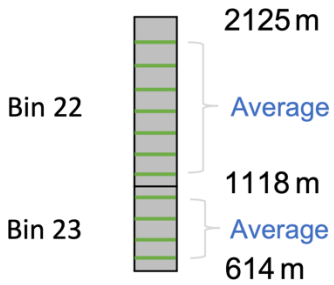

Figure 4.2: Sketch map of WPR and AUX_MET wind conversion to Aeolus range bins, where green bars represent the altitudes of WPR or AUX_MET winds. From **Article I** (Zuo et al., 2022).

4.1.2 Surface wind interpolation and collocation

To investigate the impact of Aeolus on surface wind forecasts, the predicted winds from the ECMWF OSEs (see Section 3.2.1) and the reference data (see Sections 3.2.2 and 3.2.3) were collocated first.

In situ measurements and ECMWF OSE forecasts

To spatially collocate with point-based measurements (see Section 3.2.3), 10-m wind forecasts were selected at the model grid boxes nearest to the buoy or weather station locations. The buoy winds were vertically extrapolated from a sensor height to 10 m using the method described by Bidlot et al. (2002). No extrapolation was required for the weather station data, because they were measured at a height of 10 m. Moreover, to ensure data quality and good spatial representativeness, only weather stations with correlation coefficients between wind measurements and model analysis from the control experiment (no Aeolus) greater than 0.5 were kept for further analysis. Finally, there are 751 stations available for the region > 60° N and 56 stations for the region > 60° S. The geographical distribution of the weather stations is shown in Figure 3.3. Temporally, the hourly in situ measurements at 00:00 UTC were extracted

to match with the ECMWF OSE forecasts based on the 00:00 UTC analysis with a forecast step interval of 24-h.

Scatterometer winds and ECMWF OSE forecasts

For short-range forecasts, the evaluation is based on the first-guess departures (i.e., ASCAT winds minus short-range forecasts), for which wind component interpolation and collocation are not required because they have already been done as a part of 4D-Var. Thanks to the 12-h data assimilation window, the first-guess departures have a global coverage (Figure 4.3). To ensure data quality, first-guess departures with sea ice > 0 have been removed. Moreover, 2.5°×2.5° grid boxes with data sample numbers less than 25,000 were filtered out because they were either close to lands or in polar regions, where ASCAT wind vector cells tend to be contaminated by land or sea ice.

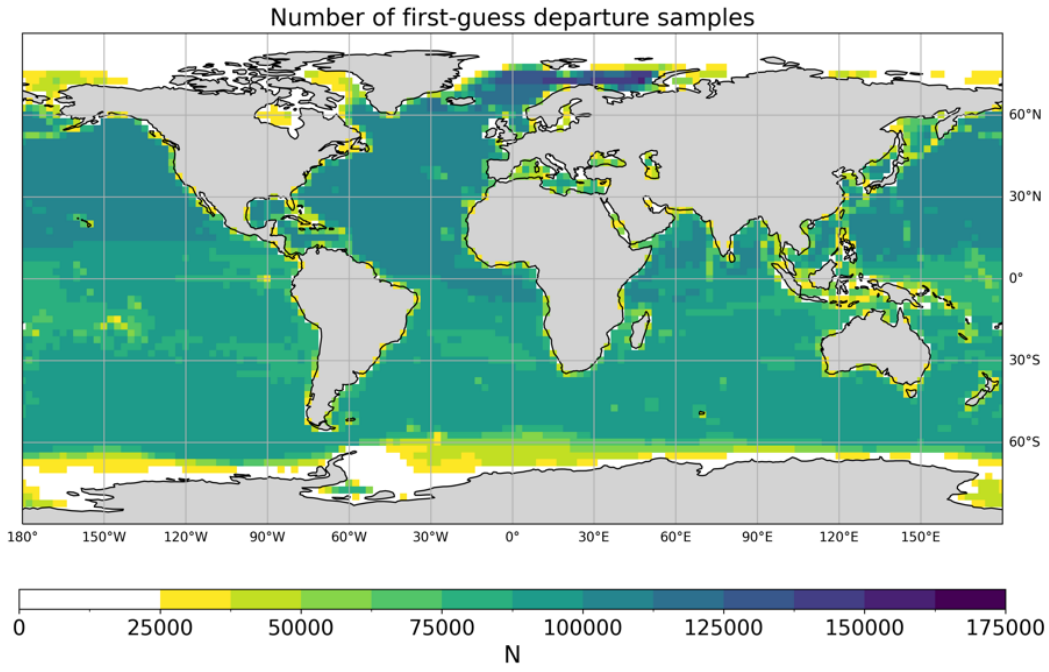

Figure 4.3: The number of paired first-guess departure data samples in 2.5°×2.5° grids. From **Article III** (Zuo et al., 2023).

To assess medium-range forecasts, the predicted winds from the ECMWF OSE and the satellite scatterometer winds were interpolated and collocated first, because of the different horizontal and temporal resolutions. The ASCAT Wind Data Processor (AWDP) software and Pencil Beam Wind Processor (PenWP) software were used for wind vector interpolation of the two ECMWF forecasts to the ASCAT and HSCAT wind vector cells, respectively (EUMETSAT NWP SAF, 2020, 2022).

Collocation and interpolation were performed at the forecast steps of T+24 h, T+48 h, T+72 h, T+96 h, and T+120 h with a collocation time window of ±30 mins for the forecast steps. For the forecasts based on the 00:00 UTC (12:00 UTC) analysis, the descending overpasses of ASCAT are mainly over the time zones of UTC+8, UTC+9, and UTC+10 (UTC-2, UTC-3, and UTC-4), and the ascending overpasses are mainly over the time zones of UTC-2, UTC-3 and UTC-4 (UTC+8, UTC+9, and UTC+10). That is to say, there are two bands available when displaying the ASCAT-based collocated samples on the map (Figure 4.4 (a)). Similarly, the HSCAT-based collocated samples are mainly over the time zones of UTC+5, UTC +6, UTC +7, UTC-5, UTC -6, and UTC -7 (Figure 4.4 (b)). Owing to the different LTs of the descending nodes of ASCAT and HSCAT, their data coverage is complementary after collocation with the ECMWF forecasts at a time interval of 24 h.

To ensure the evaluation quality, 10° × 10° grid boxes with data samples less than 50,000 were removed to avoid land or sea ice contamination. The data samples for the ASCAT-based evaluation far outweigh those for the HSCAT-based evaluation because there were three Metop satellites operating during the study period, whereas only one was available for HSCAT winds.

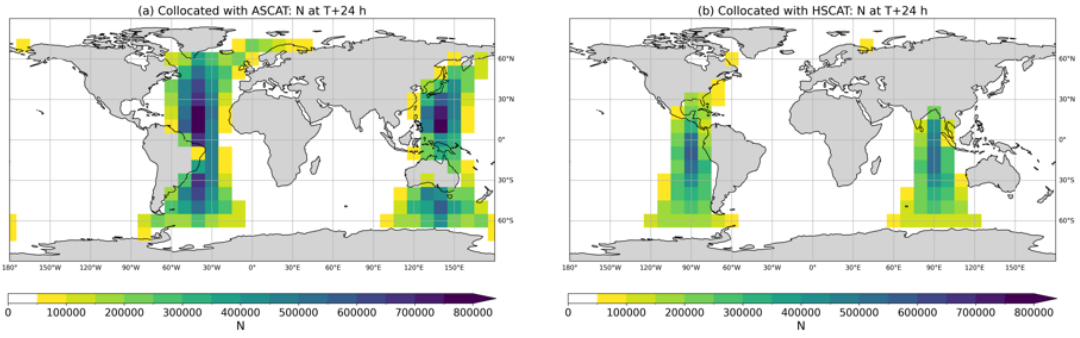

Figure 4.4: Data coverage after time collocating with (a) ASCAT winds and (b) HSCAT winds at the 24-hour forecast step. Grid boxes (10° × 10°) with data samples smaller than 50,000 have been removed as those grid boxes are mainly close to polar regions or land. From **Article III** (Zuo et al., 2023).

4.2 Inter-comparison analysis

Inter-comparison analysis is the primary method used for Aeolus wind validation and Aeolus impact evaluation for surface wind forecasts.

4.2.1 Statistics for Aeolus wind validation

For Aeolus wind validation, the WPR measurements were assumed to be the truth. The statistical metrics, including the mean bias (BIAS), standard deviation of wind difference (SD),

scaled median absolute deviation (scaled MAD), and correlation coefficient (R), were quantified for both Rayleigh-clear and Mie-cloudy winds using Eqs. (4.2), (4.3), (4.4), and (4.5). The scaled MAD was chosen to represent the random error of Aeolus observations as it is less influenced by outliers compared to the SD, making it a more robust measure of data variability (Ruppert, 2011).

$$BIAS = \frac{1}{N}\sum_{i=1}^{N}\left(HLOS_{Aeolus,i} - HLOS_{WPR,i}\right) \tag{4.2}$$

$$SD = \sqrt{\frac{1}{N-1}\sum_{i=1}^{N}\left(\left(HLOS_{Aeolus,i} - HLOS_{WPR,i}\right) - BIAS\right)^2} \tag{4.3}$$

$$Scaled\ MAD = 1.4826 \times \text{median}\left(\left|\left(HLOS_{Aeolus,i} - HLOS_{WPR,i}\right) - \text{median}\left(HLOS_{Aeolus,i} - HLOS_{WPR,i}\right)\right|\right) \tag{4.4}$$

$$R = \frac{\sum_{i=1}^{N}\left(HLOS_{Aeolus,i} - \overline{HLOS_{Aeolus}}\right)\left(HLOS_{WPR,i} - \overline{HLOS_{WPR}}\right)}{\sqrt{\sum_{i=1}^{N}(HLOS_{Aeolus,i} - \overline{HLOS_{Aeolus}})^2}\sqrt{\sum_{i=1}^{N}(HLOS_{WPR,i} - \overline{HLOS_{WPR}})^2}} \tag{4.5}$$

where N is the total number of collocated data samples, $\overline{HLOS_{Aeolus}}$ is the mean wind velocity of Aeolus, and $\overline{HLOS_{WPR}}$ is the mean wind velocity of the WPRs for each case.

The bias uncertainties were estimated at a 95 % confidence interval by using the bootstrap method because the distributions of wind difference are not always Gaussian.

4.2.2 Statistics for Aeolus impact assessment

Following existing verifications of Aeolus OSEs, the normalized change in root-mean-square difference (NCRMSD), also referred to as normalized change in root-mean-square error (NCRMSE), and the difference in mean bias error (DMBE) were used to evaluate the impact of Aeolus on surface wind forecasts.

The values of root-mean-square difference (RMSD) were quantified for u and v wind components as well as wind speed according to Eq. 4.6,

$$RMSD = \sqrt{\frac{\sum_{i=1}^{N}(o_i - f_i)^2}{N}} \tag{4.6}$$

where o_i is the wind observation from the in situ measurements or scatterometers, and f_i is the forecast wind from the ECMWF OSEs, and N is the total number of collocated data samples for each case.

Eq. 4.7 quantifies the RMSD for vector wind.

$$RMSD_{vector\ wind} = \sqrt{RMSD_u^2 + RMSD_v^2} \tag{4.7}$$

The $RMSD_{with\ Aeolus}$ and $RMSD_{no\ Aeolus}$ were quantified for u and v wind components, vector wind, and wind speed based on the forecasts with and without Aeolus wind assimilation, respectively, before calculating the corresponding NCRMSD (Eq. 4.8). A negative value of the NCRMSD implies a reduction in wind difference between the observations and the forecasts, indicating the positive impact of Aeolus.

$$NCRMSD = \frac{RMSD_{with\ Aeolus} - RMSD_{no\ Aeolus}}{RMSD_{no\ Aeolus}} \tag{4.8}$$

The mean bias error (MBE) and the difference in MBE (DMBE) of the u and v wind components were estimated using Eqs.4.9 and 4.10.

$$MBE = \frac{\sum_{i=1}^{n}(o_i - f_i)}{N} \tag{4.9}$$

$$DMBE = MBE_{with\ Aeolus} - MBE_{no\ Aeolus} \tag{4.10}$$

where o_i is the scatterometer winds, f_i is the forecasts from the ECMWF OSEs, and N is the total number of collocated data samples for each case. The $MBE_{with\ Aeolus}$ and $MBE_{no\ Aeolus}$ were quantified based on the forecasts with and without Aeolus wind assimilation, respectively, prior to calculating the DMBE.

4.3 Triple collocation analysis

In addition to the conventional inter-comparison analysis, triple collocation (TC) analysis is an advanced method for environmental parameter validation and calibration (Stoffelen, 1998; Vogelzang & Stoffelen, 2012). Implementing TC requires three independent data sets. Each data set is assumed to have a linear correlation with the truth at the scale commonly captured by all three data sets, with one data set assumed free of systematic errors to be the reference data. The primary results of TC are the ESD (or random error) of each data set and the calibration coefficients of the other two data sets based on the chosen reference data set (Vogelzang & Stoffelen, 2012). Different from the direct inter-comparison analysis that regards a reference data free of errors and estimates the relative error of a given data set, the TC analysis considers

representation errors when the three data sets have different spatial and/or temporal resolutions, and the result is the absolute errors with respect to the medium or coarsest resolution among the three data sets.

In this thesis, the TC method was attempted to validate Aeolus wind observations by taking the WPR measurements as the reference data, referred to as data set 1. Aeolus L2B wind product is the data set 2, and the predicted wind extracted from the AUX_MET is the data set 3. Table 4.1 lists the temporal and spatial resolutions of these three data sets.

Table 4.1: Spatial and temporal resolution of the WPR, Aeolus L2B and AUX_MET winds for Aeolus wind validation. From **Article I** (Zuo et al., 2022).

	1: WPR	**2: Aeolus L2B**	**3: AUX_MET**
Horizontal	Point-based	87 km (Rayleigh) / 10–15 km (Mie)	~90 km
Vertical	100/250/500 m	From 250 m to 2 km	137 model levels
Temporal	30 minutes	~ 10 seconds / ~1-2 seconds	Instantaneous

The linear relationship of each data set with the true HLOS wind is described by Eqs. 4.11, 4.12, and 4.13:

$$HLOS_1 = t + e_1 \tag{4.11}$$

$$HLOS_2 = a_2 + b_2 t + e_2 \tag{4.12}$$

$$HLOS_3 = a_3 + b_3 t + e_3 \tag{4.13}$$

where $HLOS_i$ is the HLOS winds of data set i; t is the true HLOS winds; a_i and b_i are the intercept and gradient of the calibration for data set i, respectively; e_i is the true random errors of data set i; and i=1, 2 or 3, representing WPR, Aeolus L2B and AUX_MET, respectively.

Following the equation derivation documented in Vogelzang and Stoffelen (2012), the error variance for each data set is given by the following equations (Ribal & Young, 2020):

$$\sigma_1^2 = \langle e_1^2 \rangle = C_{11} - \frac{(C_{12} - < e_1 e_2 >)(C_{13} - < e_1 e_3 >)}{C_{23} - < e_2 e_3 >} \tag{4.14}$$

$$\sigma_2^2 = \langle e_2^2 \rangle = C_{22} - \frac{(C_{12} - < e_1 e_2 >)(C_{23} - < e_2 e_3 >)}{C_{13} - < e_1 e_3 >} \tag{4.15}$$

$$\sigma_3^2 = \langle e_3^2 \rangle = C_{33} - \frac{(C_{23} - < e_2 e_3 >)(C_{13} - < e_1 e_3 >)}{C_{12} - < e_1 e_2 >} \tag{4.16}$$

where C_{ii} is the variance of each data set, C_{ij} is the covariance between two different data sets, $\langle e_i e_j \rangle$ is the error covariance between two different data sets, and $\langle \quad \rangle$ denotes the mean value.

To simplify the calculation, the true errors for each data set were assumed to be independent of each other, which makes no contribution of representation errors to the error covariances (i.e., $< e_1 e_2 > = < e_1 e_3 > = < e_2 e_3 > = 0$). Hence, the equations for calculating the ESD (σ_i) of each data set can be simplified to Eqs. 4.17, 4.18, and 4.19.

$$\sigma_1 = \sqrt{\langle e_1^2 \rangle} = \sqrt{C_{11} - \frac{C_{12}\, C_{13}}{C_{23}}} \tag{4.17}$$

$$\sigma_2 = \sqrt{\langle e_2^2 \rangle} = \sqrt{C_{22} - \frac{C_{12} C_{23}}{C_{13}}} \tag{4.18}$$

$$\sigma_3 = \sqrt{\langle e_3^2 \rangle} = \sqrt{C_{33} - \frac{C_{23} C_{13}}{C_{12}}} \tag{4.19}$$

Equations (4.20) – (4.23) give the calibration coefficients, and Eqs. (4.24) and (4.25) show the calibration relations.

$$b_2 = \frac{C_{23}}{C_{13}} \tag{4.20}$$

$$b_3 = \frac{C_{23}}{C_{12}} \tag{4.21}$$

$$a_2 = \langle HLOS_2 \rangle - b_2 \langle HLOS_1 \rangle \tag{4.22}$$

$$a_3 = \langle HLOS_3 \rangle - b_3 \langle HLOS_1 \rangle \tag{4.23}$$

$$HLOS_2^* = \frac{HLOS_2}{b_2} - \frac{a_2}{b_2} \tag{4.24}$$

$$HLOS_3^* = \frac{HLOS_3}{b_3} - \frac{a_3}{b_3} \tag{4.25}$$

Here $HLOS_2^*$ and $HLOS_3^*$ are the calibrated HLOS wind velocities of data sets 2 and 3, respectively.

A detailed description of how to implement the TC method in practice can be found in Vogelzang and Stoffelen (2012).

4.4 Wind variability analysis

Local weather conditions may affect wind measurements. To analyze the impact of atmospheric conditions on Aeolus wind observations, the wind variability of each component and the turbulence kinetic energy (TKE) were quantified using WPR measurements ±2 h around the collocation points using Eqs. (4.26) – (4.29). Results were averaged for Rayleigh-clear and Mie-cloudy winds, as well as ascending and descending orbits of each wind type.

$$Var(u) = \frac{\sum_{i=1}^{n}(u_i - \bar{u})^2}{n} \tag{4.26}$$

$$Var(v) = \frac{\sum_{i=1}^{n}(v_i - \bar{v})^2}{n} \tag{4.27}$$

$$Var(w) = \frac{\sum_{i=1}^{n}(w_i - \bar{w})^2}{n} \tag{4.28}$$

$$TKE = \frac{Var(u) + Var(v) + Var(w)}{2} \tag{4.29}$$

Here u_i, v_i , and w_i are the zonal, meridional, and vertical wind components of the WPR measurements, respectively, at each time step (every 30 min) of ± 2 h (n = 9) around the collocation points, and $\bar{u}$, $\bar{v}$, and $\bar{w}$ are the corresponding mean wind speeds.

4.5 Software and computational resources

Aeolus wind profile validation over Australia and in situ measurement-based Aeolus impact evaluations for tropical oceans and high-latitude lands were achieved mainly through Python programming.

For global ocean wind forecast evaluations, the employed software and computational resources mainly include Metview, AWDP, PenWP, Pythons, and ECMWF high-performance computing facility. Metview is a meteorological workstation application designed by ECMWF and Brazilian National Institute for Space Research (2023) for data access, processing, and visualization. For short-range forecast evaluation, the scripting language, called Macro, of Metview was used for extracting the observational feedback data of ASCAT from the ECMWF OSEs and for data pre-processing and analysis. For medium-range forecast assessments, the 10-day wind forecasts from ECMWF OSEs were retrieved using *mars* command and request syntax. AWDP and PenWP are software packages developed for generating sea surface winds from ASCAT and HSCAT, respectively, with the help of model data (EUMETSAT NWP SAF, 2020, 2022). Owing to the function of data collocation and interpolation, AWDP and PenWP were used to collocate and interpolate the ECMWF forecasts to ASCAT and HSCAT wind

vector cells, respectively. Data analysis and plot-making were done by Metview Macro and Python programming, respectively. Since the amount of data for processing was more than 2 TB due to the large number of scatterometer wind vector cells, the ECMWF high-performance computing facility was employed for handling the data processing.

5 Main Research Findings

This section provides a summary of the main research findings for each objective defined in Section 2. The corresponding publications and a submitted manuscript are attached in Appendix A, where more detailed descriptions and discussions of the results can be found.

5.1 Aeolus error characteristics over Australia

To complement the validation efforts for the SH, the Aeolus L2B baseline 11 HLOS winds over Australia from October 2020 to March 2021 were evaluated using WPR measurements and ECMWF model equivalents. Both the conventional inter-comparison and the advanced triple collocation methods were utilized to characterize the error information of the Aeolus winds. This study aims to achieve **Objective 1**, and the main research findings presented in the following sub-sections are based on **Article I** (Zuo et al., 2022).

5.1.1 Results based on inter-comparison analysis

An inter-comparison analysis was conducted using the WPR measurements as the reference. According to Figure 5.1, both Rayleigh-clear and Mie-cloudy winds are highly consistent with the ground-based WPR measurements, with correlation coefficients of no smaller than 0.90 for all collocated samples and 0.86 for different orbits. The overall biases are -0.48 m s^{-1} and 0.69 m s^{-1} for Rayleigh-clear and Mie-cloudy winds, respectively, which achieves the intended mission bias of 0.7 m s^{-1}. Mie-cloudy winds show a better precision than Rayleigh-clear winds, with an overall random error (i.e., scaled MADs) of 4.14 m s^{-1} and 5.81 m s^{-1}, respectively. However, the values of both measurement channels, particularly the Rayleigh channel, are higher than the mission-intended random errors, which are primarily associated with the long-term unexpected signal loss of the instrument (Krisna & Wernham, 2023). These results are comparable to the WPR-based validations for Baseline 10 data in Japan (Iwai et al., 2021). Regarding the results in different orbits, wind observations in the Mie channel show a larger bias and poorer precision during ascending orbits than those during descending orbits.

Table 5.1 gives information about wind variability in three directions and TKE during Rayleigh and Mie wind sampling as well as during ascending and descending orbits. Larger wind variability, particularly for *w* component, and TKE are obtained during Mie wind sampling than during Rayleigh wind sampling, suggesting more convective conditions during Mie wind sampling. In terms of orbit, for Mie-cloudy winds, significantly larger wind variability in *v* and *w* components as well as TKE are obtained during ascending orbits than during descending orbits, which implies different atmospheric conditions in the afternoon (ascending) and morning (descending), with more convective weathers being in the late afternoon. Thus, the poorer

accuracy and precision of Mie-cloudy winds during ascending orbits than during descending orbits may result from the atmospheric convection in the late afternoon.

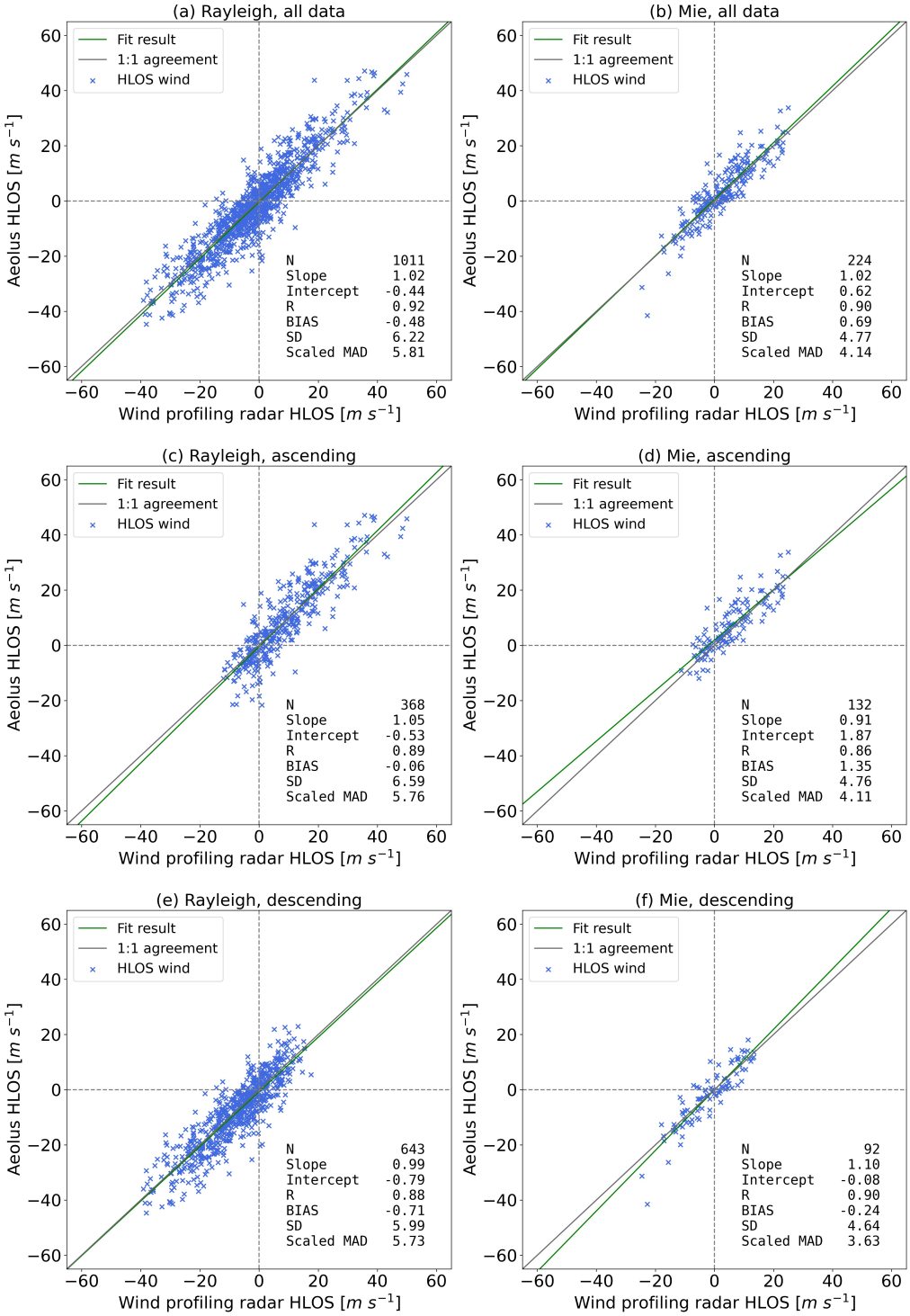

Figure 5.1: Scatter plots of Aeolus HLOS winds against WPR HLOS winds for all data, ascending orbits and descending orbits. Plot (a), (c) and (e) are for the Rayleigh-clear winds, and (b), (d) and (f) are for the Mie-cloudy winds. Green and grey lines indicate the fitted regression result and 1:1 agreement, respectively. From **Article I** (Zuo et al., 2022).

Table 5.1: Zonal (*u*), meridional (*v*), and vertical (*w*) wind variability and TKE based on WPR measurements. From **Article I** (Zuo et al., 2022).

	Var (*u*)	**Var (*v*)**	**Var (*w*)**	**TKE**
Rayleigh-clear [m^2 s^{-2}]	2.24	2.09	0.01	2.15
Mie-cloudy [m^2 s^{-2}]	2.48	2.45	0.03	2.48
***p* value**	0.358	0.181	< 0.001	0.110
Rayleigh-clear Ascending [m^2 s^{-2}]	2.08	1.80	0.02	1.94
Rayleigh-clear Descending [m^2 s^{-2}]	2.34	2.25	0.01	2.26
***p* value**	0.298	0.070	< 0.001	0.097
Mie-cloudy Ascending [m^2 s^{-2}]	2.78	2.95	0.03	2.89
Mie-cloudy Descending [m^2 s^{-2}]	2.06	1.76	0.02	1.92
***p* value**	0.143	0.029	0.002	0.033

Validation was performed as a function of height for all match-ups from the 6 WPR sites and also from the tropical and extratropical sites, separately, as Australia crosses two range bin setting regions. The analysis for all match-ups was performed by re-grouping collocated data samples into 12 new range bins defined by considering the sample size and atmospheric characteristics at different altitudes, as shown in Figure 5.2. The numbers of collocated Rayleigh-WPR samples are far greater than that of the Mie-WPR samples in almost all new range bins. Mie wind measurements mainly occur below 10,000 m owing to the Mie scattering from aerosols, water droplets, and ice crystals in the troposphere. The number of Mie-WPR samples peaks at altitudes between 4,500 m and 6,000 m during descending orbits, which may be related to the mid-level clouds that usually exist in warm spring and summer mornings (Gao et al., 2019). Very few data samples are at the bottom range bin, suggesting the necessity for better Aeolus DWL signals.

Regarding the measurement accuracy, the magnitudes of the biases for Rayleigh-clear and Mie-cloudy winds are comparable in most range bins (Figure 5.2). The mission-intended bias is achieved by Mie-cloudy winds during descending orbits between 750 and 6,000 m, partly owing to stable atmospheric conditions in the morning. The random errors of Mie-cloudy winds are typically smaller than those of Rayleigh-clear winds for most range bins, except above 4,250 m in the extratropics. For Rayleigh-clear winds, large random errors are obtained, particularly for the altitudes below 1,500 m and above 12,500 m (Figure 5.2), which may be related to the smaller range bin thickness at those heights in the tropics (Figure 5.3 (a)). Another key finding is that the Mie channel performs better in wind measurements for the PBL than the Rayleigh channel, as demonstrated by the smaller biases and random errors, as well as uncertainties

below 1,500 m for most cases (Figure 5.2 and Figure 5.3). This result suggests a greater impact of Mie-cloudy winds on data assimilation for estimating the state of the low-level atmosphere in the NWP models.

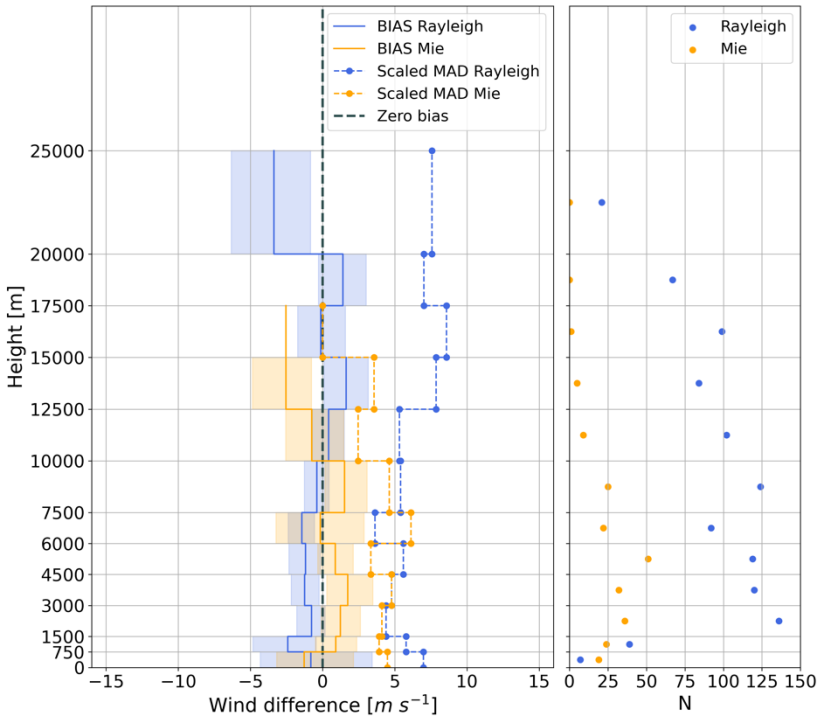

Figure 5.2: Vertical profile of BIAS and scaled MAD based on wind differences (Aeolus–WPR) with shading areas representing the uncertainty (left) and the number of available match-ups (right) for all data. Blue and orange colors indicate the results for the Rayleigh and Mie channels, respectively. From **Article I** (Zuo et al., 2022).

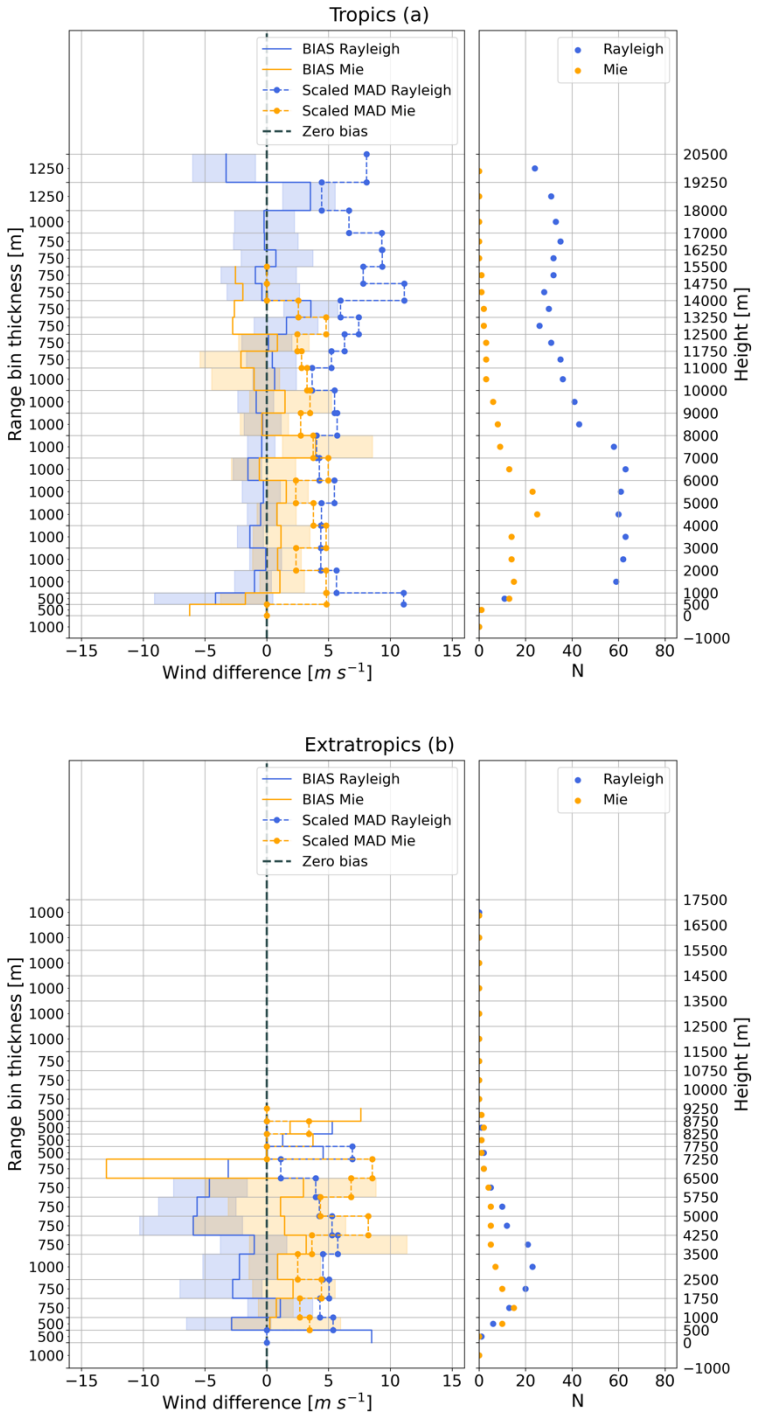

Figure 5.3: Wind differences (Aeolus–WPR) with Aeolus range bins for (a) tropics and (b) extratropics. Left: distributions of BIAS and scaled MAD of wind differences over different range bins with shading areas representing the uncertainty. Right: the number of available match-ups at each range bin. Blue and orange colors indicate the results for the Rayleigh and Mie channels, respectively. Note: the heights on y-axis are just for reference, which are not

exactly same with the actual heights of each vertical range bin. From **Article I** (Zuo et al., 2022).

5.1.2 Results based on triple collocation analysis

Aeolus wind validation was also performed via triple collocation (TC) analysis using WPR wind measurements and ECMWF model-predicted winds (i.e., AUX_MET). The key results are shown in Table 5.2 and Table 5.3. The error standard deviations (ESDs) of Rayleigh-clear and Mie-cloudy winds are 5.61 m s^{-1} and 3.50 m s^{-1}, respectively. This result is almost in line with the random errors from inter-comparison analysis, indicating that the Mie-cloudy winds have a higher precision. For bias calibration, the intercepts and slopes are -0.404 and 1.044 for Rayleigh-clear winds and 0.388 and 1.106 for Mie-cloudy winds.

Table 5.2: Error standard deviations of the WPR, Aeolus L2B, and AUX_MET ECMWF data derived from triple collocation analysis. From **Article I** (Zuo et al., 2022).

	1: WPR [m s^{-1}]	**2: Aeolus L2B** [m s^{-1}]	**3: AUX_MET** [m s^{-1}]	**N**
Rayleigh-clear	2.01	5.61	1.17	1011
Mie-cloudy	2.60	3.50	1.70	224

Table 5.3: The calibration coefficients and relations for Aeolus L2B data. Adapted from **Article I** (Zuo et al., 2022).

	a_2	b_2	$HLOS_2^*$
Rayleigh-clear	-0.404	1.044	$0.958HLOS_2 + 0.387$
Mie-cloudy	0.388	1.106	$0.904HLOS_2 - 0.351$

Since the effective spatial resolution of an NWP model in the free atmosphere is generally 7–10 times the grid spacing (Skamarock, 2004), the Aeolus Rayleigh-clear winds (~87 km) and ECMWF model-predicted winds (~90 km) have similar horizontal resolutions. This implies that almost no common variance between the Rayleigh-clear winds and WPR measurements is not resolved by the coarse ECMWF model. Thus, the representation error has a limited impact on the Rayleigh wind analysis. For Mie wind analysis, the WPR and Aeolus measure the small-scale wind signals that are not resolved by the coarse model, which results in a larger ESD of ECMWF model winds. Assuming a spatial representation error for NWP of 1 m s^{-1} (Stoffelen et al., 2020), then the ESDs with respect to the ECMWF model resolution become 2.79, 3.64 and

1.37 m s^{-1} for WPR winds, Mie-cloudy winds, and ECMWF model equivalents, respectively. The results based on both Rayleigh-clear and Mie-cloudy wind combinations indicate that ECMWF model-predicted winds exhibit the highest precision, followed by the WPR wind measurements, and both are more precise than the Aeolus measurements. Compared to the inter-comparison analysis, TC method allows us to compare the data quality of each data set at the same resolution, which would provide valuable information for data assimilation in NWP.

Moreover, the larger ESDs in the WPR measurements and ECMWF-predicted winds are obtained for the combination of Mie-cloudy winds than for the Rayleigh-clear winds. This is probably associated with the vertical wind shear and atmospheric convection during the Mie wind observations (Table 5.1) which can make the model winds less accurate (Lin et al., 2016). In addition, notably, the ESDs for the Mie-cloudy combination have larger uncertainties because of the small sample size (N=224) which is much lower than the recommended sample size (N>1,000) for carrying out TC analysis.

To summarize, Objective 1 is reached by investigating whether the performance of the spaceborne DWL on Aeolus satisfied the mission requirements for bias and precision in Australia. The inter-comparison analysis demonstrates that the spaceborne DWL is capable of profiling winds over Australia with sufficient overall biases for both Rayleigh-clear and Mie-cloudy winds, which is in agreement with the hypothesis. Moreover, the Mie-cloudy winds (4.14 m s^{-1}) exhibit higher precision than the Rayleigh-clear winds (5.81 m s^{-1}). However, contrary to the hypothesis, wind data from both channels fail to meet the mission precision requirements, mainly because of the unexpected signal loss of the DWL. The precisions derived from the TC analysis align with the findings of the inter-comparison analysis. Additionally, inter-comparison analysis indicates that Mie-cloudy winds are more accurate and precise than Rayleigh-clear winds in the PBL.

5.2 Impact of Aeolus on global sea surface wind forecasts

Assimilating Aeolus winds into NWP models to facilitate weather forecasts is one of the main applications of Aeolus wind profile observations. According to the existing verifications based on different OSEs, the impact of Aeolus on model skills is not spatially uniform. Therefore, it is important to understand the impact of Aeolus on wind forecasts geographically before applying it to different fields. In this PhD project, the investigations are based on the forecasts from the ECMWF OSEs with a focus on sea surface winds. This study was first performed for tropical ocean regions by comparing to buoy measurements, which is documented in **Article II**. Then, the study was extended to the global ocean using satellite scatterometer winds, which is detailed in **Article III**. The studies presented in this section correspond to **Objective 2**.

5.2.1 Buoy-based assessments for tropical ocean regions

Assessments for the three tropical ocean regions were performed for the year 2020 by comparing ECMWF OSE forecasts based on 00:00 UTC analysis to ocean buoy measurements. Assessments were also conducted for the first and second halves of 2020 to investigate the influence of the Aeolus data quality on ocean surface wind forecasts.

For the forecasts in 2020, some reductions in RMSE are obtained for wind components and wind speed in each ocean basin with Aeolus wind assimilation, but none of them are statistically significant at a 95% confidence interval. This may be caused by the coarse model resolution, which makes the small-scale convection in the tropics not well-resolved by the model (Sandu et al., 2020), whereas point-based buoy measurements can capture it. Another possible reason is the sparse distribution of buoys and the limited data samples available during the study period. Unsurprisingly, the results (i.e., normalized change in RMSE) in the first and second halves of 2020 do not differ significantly, suggesting that the model skills for sea surface wind forecasts in the tropical oceans are not sensitive to Aeolus data quality. Overall, the buoy-based assessments indicate that the contribution of Aeolus to tropical ocean wind forecasts is limited.

5.2.2 Scatterometer-based assessments for global ocean

To further assess the impact of Aeolus wind observations on ocean wind forecasts, the study regions was extended to the global ocean by using satellite scatterometer winds instead of buoy measurements for reference data. The assessments are based on the ECMWF OSEs during July 2019 – June 2020. The main results are summarized as follows.

Short-range forecasts

Assessments based on the first-guess departures between ASCAT observations and short-range forecasts indicate that assimilating Aeolus winds into the ECMWF model can improve sea surface wind forecasts for most ocean regions, leading to reductions of ~2% and ~3% in RMSD for vector wind and wind components, respectively (Figure 5.4). However, the influences of Aeolus wind assimilation on wind forecasts over the tropical regions of the eastern Pacific are limited or even negative.

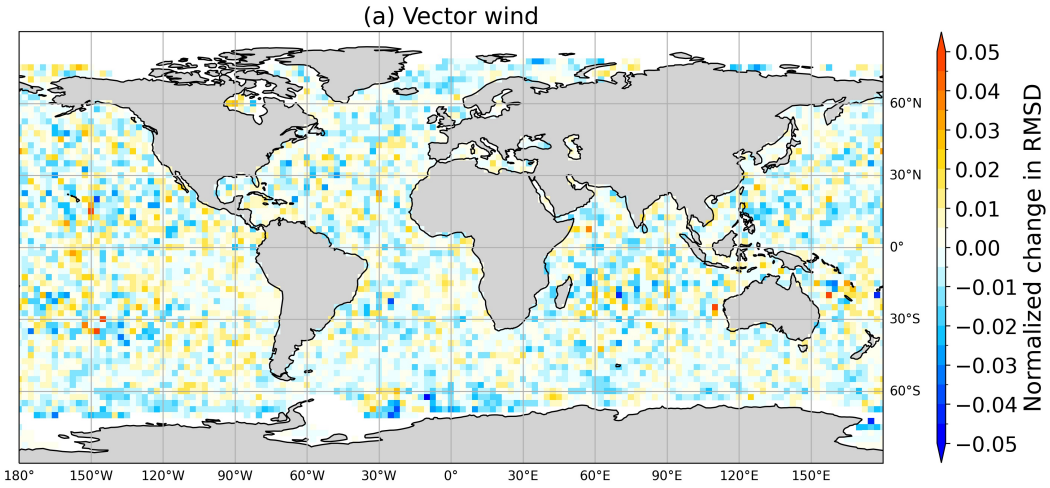
(a) Vector wind
60°N
30°N
0°
30°S
60°S
180°
150°W
120°W
90°W
60°W
30°W
0°
30°E
60°E
90°E
120°E
150°E
0.05
0.04
0.03
0.02
0.01
0.00
−0.01
−0.02
−0.03
−0.04
−0.05
Normalized change in RMSD

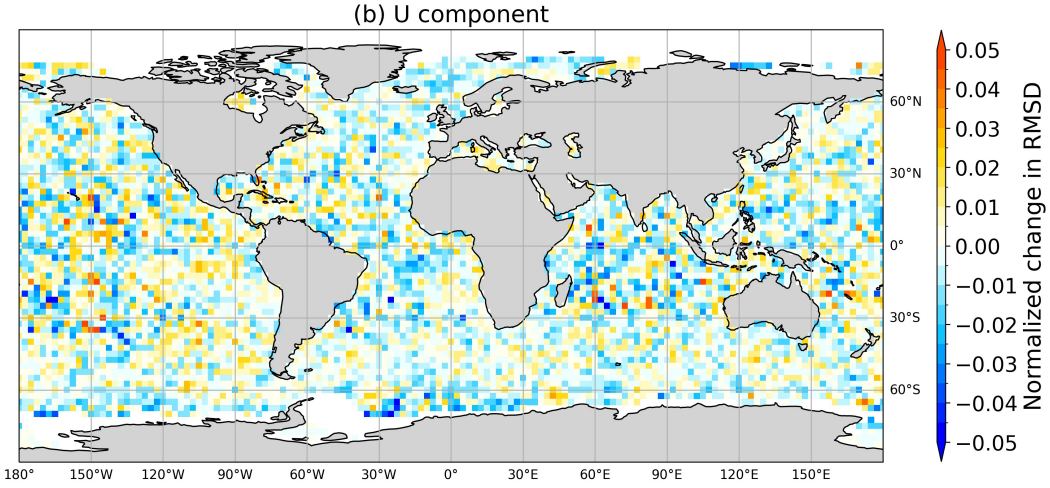
(b) U component
60°N
30°N
0°
30°S
60°S
180°
150°W
120°W
90°W
60°W
30°W
0°
30°E
60°E
90°E
120°E
150°E
0.05
0.04
0.03
0.02
0.01
0.00
−0.01
−0.02
−0.03
−0.04
−0.05
Normalized change in RMSD

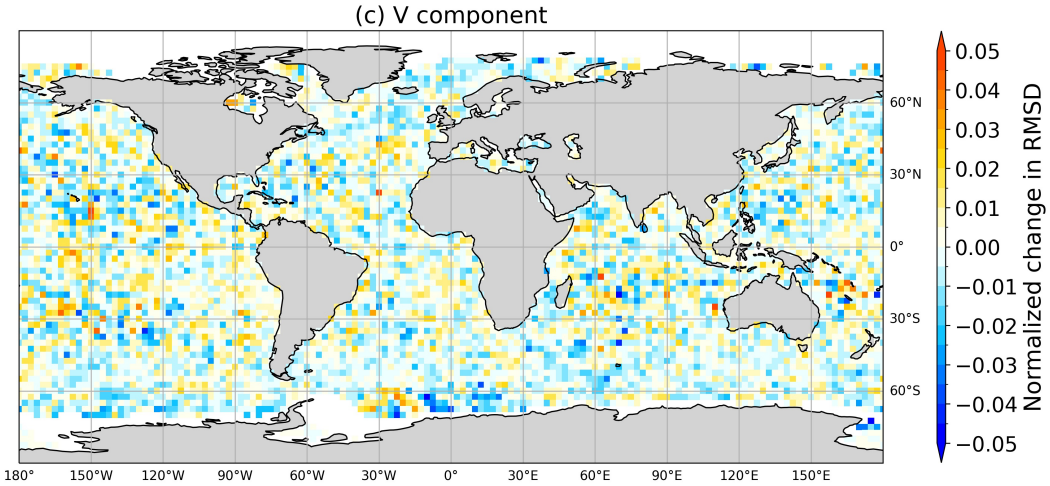
(c) V component
60°N
30°N
0°
30°S
60°S
180°
150°W
120°W
90°W
60°W
30°W
0°
30°E
60°E
90°E
120°E
150°E
0.05
0.04
0.03
0.02
0.01
0.00
−0.01
−0.02
−0.03
−0.04
−0.05
Normalized change in RMSD

Figure 5.4: Normalized change in RMSD for (a) vector wind, (b) *u* component, and (c) *v* component based on first-guess departures between ASCAT winds and short-range forecasts. Negative values indicate a positive impact of Aeolus. From **Article III** (Zuo et al., 2023).

Table 5.4 summarizes the results for different climatic regions. Although the overall contributions of Aeolus to ocean wind forecasts are very small, these impacts are positive and statistically significant at the global scale and in the extratropical oceans. This result is in line with the analysis-based verifications shown in the ECMWF report (see Page 163, Figure 126 (h); Rennie & Isaksen, 2023). For the tropics, wind forecast improvement is obtained only for the *u* component. This is probably related to the Aeolus measurement geometry (Andersson et al., 2008), i.e. approximately east-west winds are detected at lower latitudes, and the relative independence of the *u* and *v* components in the tropics (Žagar et al., 2021).

Table 5.4: Averaged normalized change in RMSD for each climatic region based on the first-guess departures between ASCAT winds and ECMWF short-range forecasts. Negative values indicate error reduction, hence a positive impact of Aeolus. Positive values indicate the increase in error, hence a negative impact of Aeolus. A star (*) marks that the error reduction is statistically significant at a 95% confidence interval, indicating positive impact of Aeolus wind assimilation. Adapted from **Article III** (Zuo et al., 2023).

Region	**Vector wind**	***u* component**	***v* component**
Global	-0.0011*	-0.0013*	-0.0009*
NH (> 20° N)	-0.0012*	-0.0012*	-0.0012*
Tropics	-0.0004	-0.0013*	0.0002
SH (> 20° S)	-0.0015*	-0.0014*	-0.0016*

Regarding the influence of Aeolus wind assimilation on forecast bias, the assessment shows that Aeolus is able to correct short-range forecast bias for wind components to some extent. Figure 5.5 (a) and (b) show the large-scale forecast biases on the *u* and *v* components from the control experiment (no Aeolus), mainly ranging from -1 m s^{-1} to 1 m s^{-1}. With Aeolus data assimilated in addition, the biases can be changed by 0.02–0.05 m s^{-1} for most regions (Figure 5.5 (c) and (d)). When the positive (negative) biases in Figure 5.5 (a) and (b) coincides with the negative (positive) bias changes in Figure 5.5 (c) and (d), it indicates that the model biases are slightly reduced by Aeolus wind assimilation, such as in the tropical Indian Ocean for the *u* component.

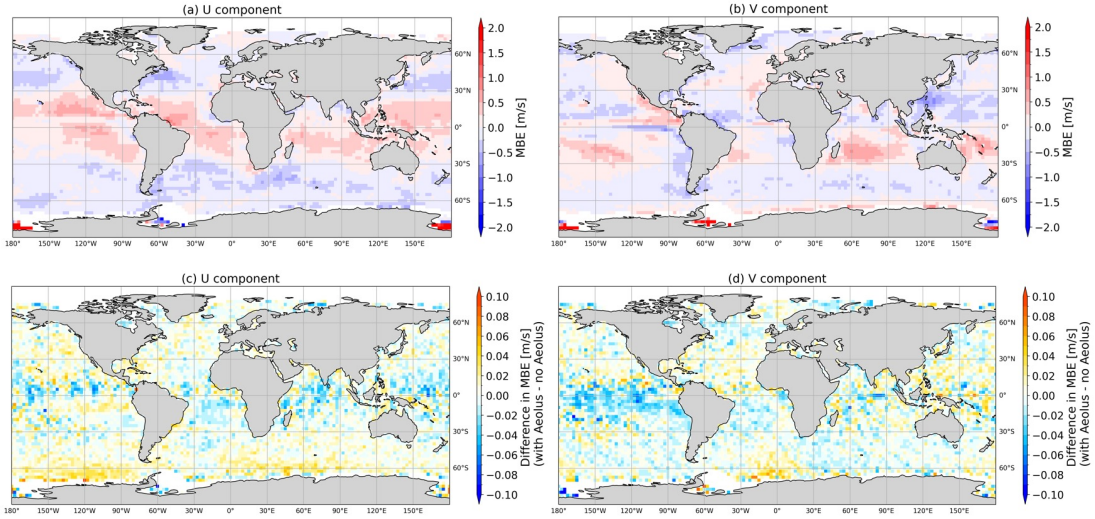

Figure 5.5: (a, b) The MBEs based on the control experiment without Aeolus for the *u* and *v* components; (c, d) the differences in MBE between the experiment with Aeolus and the control experiment without Aeolus for the *u* and *v* components. Evaluations are based on the first-guess departures between ASCAT observations and short-range forecasts. From **Article III** (Zuo et al., 2023).

Figure 5.6 illustrates the relationship between the changes in MBE resulting from assimilating Aeolus winds and the MBEs obtained from the forecast without Aeolus data assimilation in each climatic region. In other words, the x-axis shows the MBEs (Eq. 4.9) from the control experiment (no Aeolus), and the y-axis presents the difference in MBE (i.e., DMBE based on Eq. 4.10) caused by Aeolus data assimilation. Thus, for a positive MBE and a positive DMBE (i.e., Quadrant I), the bias from the forecast with Aeolus data assimilation becomes even larger, indicating the negative impact of Aeolus on model bias correction. For a negative MBE and a positive DMBE (i.e., quadrant II), the negative MBE is balanced with the positive MBE, indicating that Aeolus data assimilation helps reduce forecast bias. Similarly, quadrant III represents that Aeolus increases the biases, while quadrant IV represents that Aeolus reduces the biases. Blue numbers indicate the percentage of scatters in each quadrant. Figure 5.6 in this thesis is the modified version of Figure 6 in **Article III**. In Figure 5.6, the percentage of scatters was added in each quadrant, and the mean values with respect to the positive and negative MBEs were removed to improve the readability and omitted due to some errors in the calculation.

The results show that Aeolus wind assimilation reduces the forecast biases for the majority of regions, with the percentage sum from quadrant II and quadrant IV larger than 50% for most cases (Figure 5.6).

For the *u* component, the NH and SH extratropical regions are dominated by the negative biases, and most of them are reduced with Aeolus wind assimilation, as shown in quadrant II in Figure 5.6 (a) and (e); while for the tropics, positive biases dominate most regions, with bias reduction found in quadrant IV (Figure 5.6 (c)). These results indicate that the large-scale biases of the *u* component are corrected by Aeolus wind assimilation to some extent.

For the *v* component, negative biases are reduced for the NH extratropics, with the majority in quadrant II (Figure 5.6 (b)). For the tropics, negative biases dominate most of the region, but positive bias is mainly reduced, with the majority in quadrant IV (Figure 5.6 (d). For the SH extratropics, negative biases are mainly enhanced (quadrant III, Figure 5.6 (f)), and the percentage sum from quadrant II and quadrant IV is slightly less than 50%; thus, assimilation of Aeolus winds did not reduce the bias for the majority of region for the v component.

Overall, the wind forecast biases are slightly reduced with Aeolus wind assimilated. It is more pronounced for the *u* component owing to the approximately east-west wind observations of Aeolus than for the *v* component. Aeolus helps to reduce zonal wind biases for all climatic regions and has a beneficial impact on meridional wind biases but mainly for the NH extratropical and tropical regions.

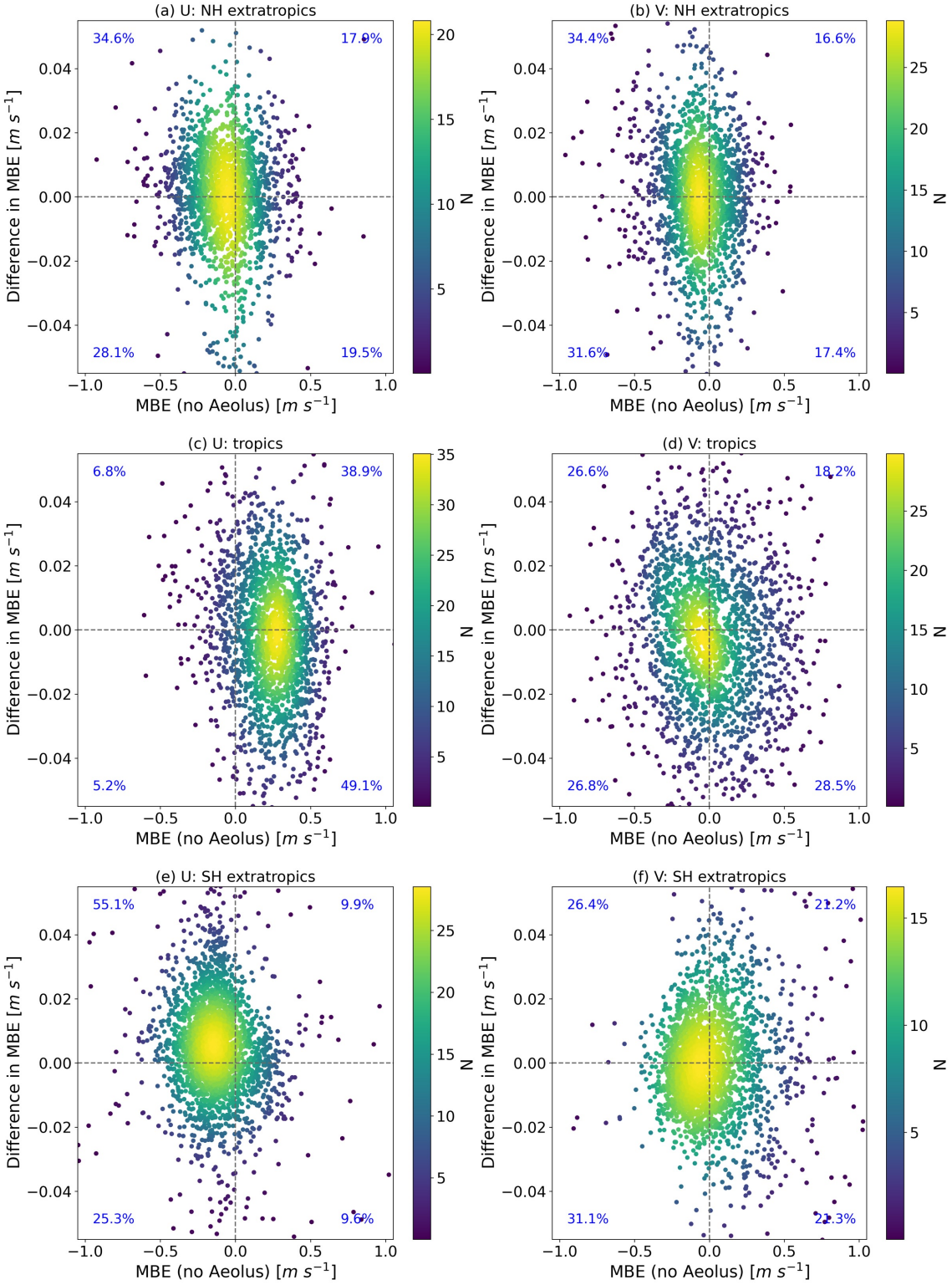

Figure 5.6: Scatter plots of the difference in MBE (DMBE) against the MBE of the control experiment (no Aeolus) for the *u* and *v* components in the NH extratropics, tropics, and SH extratropics. Scatters in quadrants II and IV indicate bias reduction owing to Aeolus data

assimilation. The blue numbers show the percentages of scatters in each quadrant. All scatters are used for percentage calculation, although a few outliers are out of the limit of x-axis and y-axis. Modified based on **Article III** (Zuo et al., 2023) by removing mean values and adding percentages.

Medium-range forecasts

The impact of Aeolus on medium-range forecasts was investigated at T+24 h, T+48 h, T+72 h, T+96 h, and T+120 h forecast steps by comparing with the ASCAT and HSCAT wind products. Negative NCRMSDs are obtained in most regions, especially for the ASCAT-covered regions, indicating a positive impact of Aeolus on sea surface wind forecasts (Figure 5.7). Moreover, as the forecast progresses, the positive impacts become more evident, particularly in the extratropical regions of the Atlantic Ocean at T+72 h and T+96 h and in the southeast of the Pacific Ocean at T+120 h. This increasing positive impact is likely due to the Aeolus wind measurements at higher altitudes. These measurements benefit the estimation of the atmospheric initial state at the upper levels via data assimilation, which could improve tropospheric wind forecasts through downward propagation (Charlton et al., 2004; Christiansen, 2001; Kodera et al., 1990).

According to the current results from ASCAT-based assessments and considering the ability of Aeolus to capture orographic gravity waves over the Southern Andes (Banyard et al., 2021), the coastal regions along the southeast of South America are promising to benefit from Aeolus wind assimilation. For these regions, future research could be conducted using mesoscale models to determine the contribution of Aeolus winds in generating high-resolution meteorological data for limited areas, which would be beneficial for practical applications in the wind energy sector.

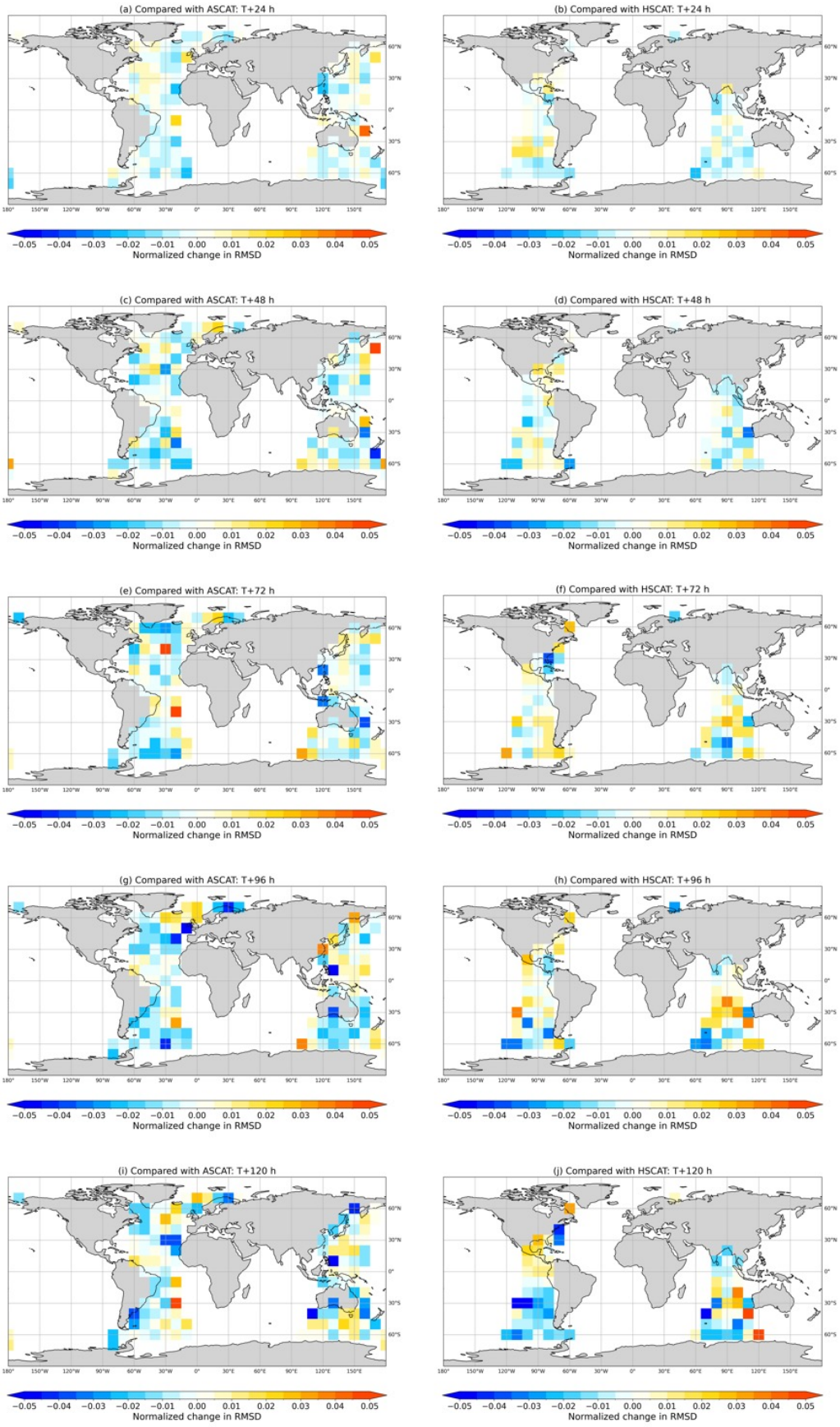
(a) Compared with ASCAT: T+24 h
(b) Compared with HSCAT: T+24 h
(c) Compared with ASCAT: T+48 h
(d) Compared with HSCAT: T+48 h
(e) Compared with ASCAT: T+72 h
(f) Compared with HSCAT: T+72 h
(g) Compared with ASCAT: T+96 h
(h) Compared with HSCAT: T+96 h
(i) Compared with ASCAT: T+120 h
(j) Compared with HSCAT: T+120 h
−0.05 −0.04 −0.03 −0.02 −0.01 0.00 0.01 0.02 0.03 0.04 0.05
Normalized change in RMSD

Figure 5.7: Normalized change in RMSD for vector wind by taking ASCAT and HSCAT winds as the reference. Negative values indicate a positive impact of Aeolus. From **Article III** (Zuo et al., 2023).

After grouping the results from Figure 5.7 into different climatic zones, Table 5.5 shows that the significant error reductions are mainly in the SH extratropics, with the negative mean NCRMSDs from T+24 h to T+96 h for the ASCAT-based assessments and at T+120 h for the HSCAT-based assessments. For the NH extratropics and tropics, the significant error reductions are obtained only at T+120 h and T+48 h, respectively, for ASCAT-covered regions. There is no significant increase in RMSD for both the ASCAT- and HSCAT-based assessments. Overall, the results suggest that the SH extratropical regions tend to benefit more from the Aeolus winds than the NH extratropics and tropics, which is consistent with the analysis-based verifications for the same OSEs at the ECMWF, as shown in the report (Page 167, Figure 130) by Rennie and Isaksen (2023). In Table 5.5, the averaged NCRMSDs of ASCAT- and HSCAT-based assessments show different patterns as a function of the forecast step. This difference in pattern is due to the different geographical regions covered by Metop and HY-2B swaths, where the model may have different performances. Notably, for the HSCAT-based assessments, few grids are available in the NH extratropical ocean regions, which leads to large uncertainties in the results.

Table 5.5: Averaged normalized change in RMSD for vector wind in each climatic region for the forecast steps from T+24 h to T+120 h by taking ASCAT and HSCAT scatterometer winds as references. Negative values indicate error reduction, hence a positive impact of Aeolus. Positive values indicate the increase in error, hence a negative impact of Aeolus. A star (*) marks that the error reduction is statistically significant at a 95% confidence interval. Adapted from **Article III** (Zuo et al., 2023).

Reference	Region	T+24 h	T+48 h	T+72 h	T+96 h	T+120 h
ASCAT	All	-0.0018*	-0.0026*	-0.0027*	-0.0076*	-0.0089
	NH (> 20° N)	-0.0005	0.001	-0.0024	-0.0044	-0.0055*
	Tropics	0	-0.0032*	-0.0014	-0.012	-0.0197
	SH (> 20° S)	-0.0042*	-0.0053*	-0.004*	-0.0071*	-0.0037
HSCAT	All	-0.0013	-0.0022	0.0016	0.001	-0.0057*
	NH (> 20° N)	0.0013	0.0051	-0.0048	0.0053	-0.0002
	Tropics	-0.0005	-0.0028	0.0001	0.0031	0.0018
	SH (> 20° S)	-0.0022	-0.0028	0.0037	-0.0012	-0.0118*

Due to the time constraints of the PhD study, the assessments are focused on forecast steps to T+120 h with a 24-h time interval, which restricts the data coverage of ASCAT and HSCAT to two bands on the maps. To increase data coverage, assessments can be performed for different forecast ranges with a shorter time interval. For example, an ASCAT-based assessment can be performed from T+12 h to T+36 h with a 6-h time interval, and then the results can be merged to cover most of the Indian Ocean and Pacific Ocean in addition. Apart from this, the assessments can be extended up to T+240 h to investigate the longer impact of Aeolus.

In summary, the value of Aeolus wind profiles for ocean wind forecasts was assessed based on the ECMWF OSEs and wind observations, which achieved **Objective 2**. The forecasts were verified using buoy measurements for tropical ocean regions and satellite scatterometer winds for the global ocean. Contrary to the initial hypothesis, Aeolus makes a limited contribution to medium-range wind forecasts for the tropical ocean regions when comparing to buoy measurements. By taking satellite scatterometer winds as the reference, Aeolus generally helps to reduce the short-range forecast biases for zonal wind, while its contribution to meridional bias correction is mainly obtained in the NH extratropical and tropical regions. Moreover, Aeolus can generally improve the short-range wind forecasts for the global ocean, except in the tropics, and benefit the medium-range wind forecasts, particularly for the SH extratropics. These results are not fully in agreement with the hypotheses.

5.3 Impact of Aeolus on surface wind forecasts in high-latitude lands

The impact of Aeolus on near-surface wind forecasts over high-latitude lands was investigated based on the ECMWF OSEs in 2020 and wind measurements at weather stations. This study aims to achieve the **Objective 3** defined in this thesis. Further details of this study can be found in **Article II** (Zuo & Hasager, 2023).

For the region > 60° N, the surface wind forecasts tend to gradually benefit from Aeolus wind assimilation. The NCRMSEs for the *u* and *v* components and the wind speed are almost negative and decrease as the forecast step progresses (Figure 5.8). A significant positive contribution of Aeolus is mainly obtained after T+192 h. This result aligns, to some extent, with the analysis-based verifications conducted by the ECMWF, both showing a noticeable positive impact at the T+216 h forecast step (Rennie & Isaksen, 2023). One possible explanation is that Aeolus wind measurements help better estimate the stratospheric initial states, which in turn benefits the forecasts of tropospheric circulation in the following days through downward propagation (Charlton et al., 2004; Christiansen, 2001; Kodera et al., 1990; Tripathi et al., 2015). Moreover, Aeolus is found to have a more positive influence on *v* component forecasts. This may be related to the Aeolus measurement geometry at higher latitudes, where wind velocities close to the meridional direction are detected, which in turn contributes more to the *v* component predictions.

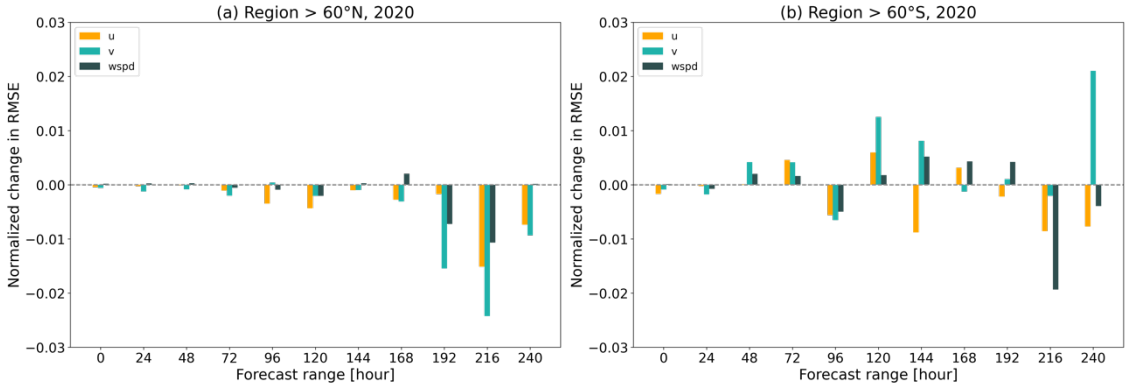

Figure 5.8: Normalized change in RMSE of *u* and *v* components and wind speed (wspd) as a function of forecast range for (a) the region > 60° N and (b) the region > 60° S for the year 2020. Forecasts from ECMWF OSEs with and without Aeolus are compared against weather station data. Adapted from **Article II** (Zuo & Hasager, 2023).

The assessments also show that there are more error reductions for the *u* and *v* wind components during the first half year of 2020 than during the second half year (Figure 5.9), implying that the increased random errors of Aeolus due to signal loss may degrade its contribution to wind forecasts. Moreover, Aeolus tends to make more positive contributions from T+120 h onwards during the boreal winter (January, February, and December) than during the boreal summer (June, July, and August) (Figure 5.10). This is partially explained by the increased random errors of Rayleigh-clear winds during the summer months over polar regions and in the stratosphere due to the varied solar background noise with season (Reitebuch et al., 2022). Another possible explanation for the evident error reductions during winter is that Aeolus contributes more to higher wind speed forecasts than to lower wind speed forecasts (Figure 5.11). Consequently, there could be more error reductions during the stormy season, which is often the wintertime in the region > 60° N.

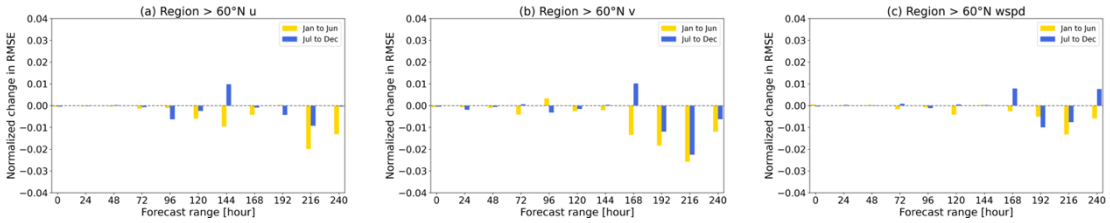

Figure 5.9: Normalized change in RMSE of *u* and *v* components and wind speed (wspd) as a function of forecast range during each half-year of 2020 for the region > 60° N. Forecasts from the ECMWF OSE with and without Aeolus are compared against weather station data. From **Article II** (Zuo & Hasager, 2023).

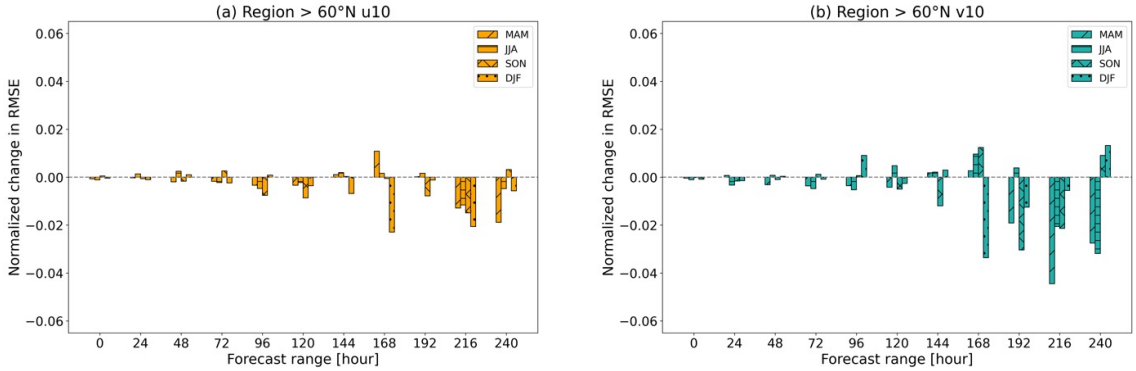

Figure 5.10: Seasonal variation in normalized change in RMSE of *u* and *v* components as a function of forecast range for the region > 60° N for the year 2020. Forecasts from ECMWF OSEs with and without Aeolus are compared against weather station data. MAM: March, April, and May; JJA: June, July, and August; SON: September, October, and November; DJF: December, January, and February. From **Article II** (Zuo & Hasager, 2023).

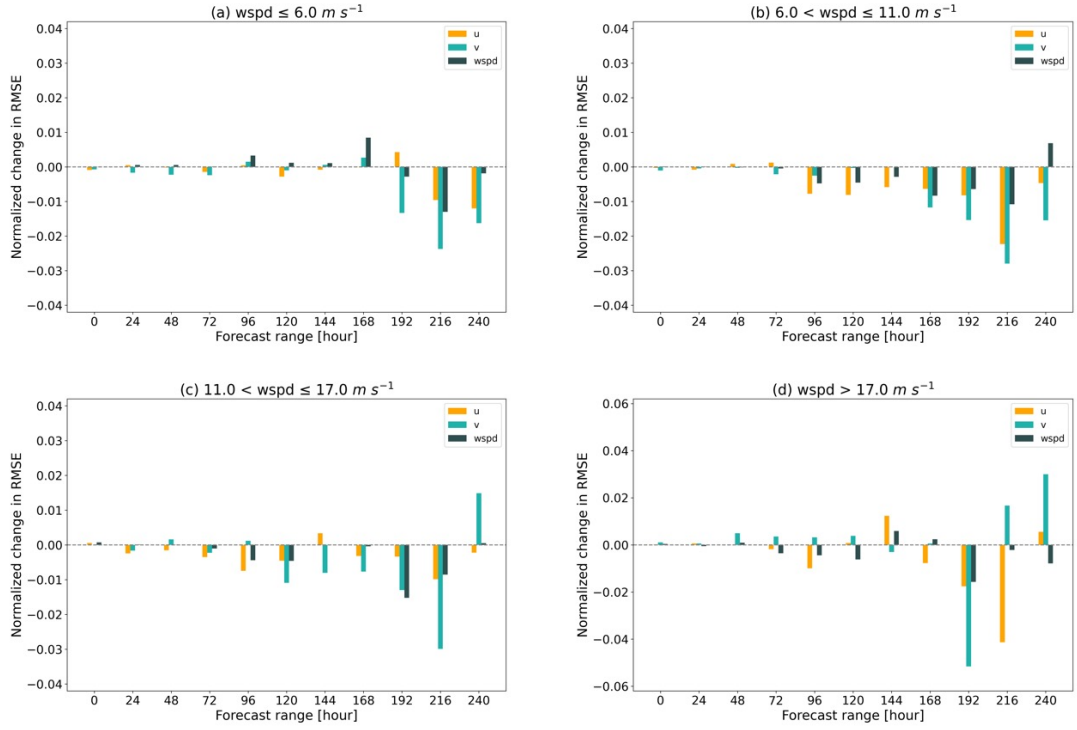

Figure 5.11: Same to **Figure 5.8** but for different wind speed ranges. From **Article II** (Zuo & Hasager, 2023).

Unlike the high-latitude regions in the NH, the impact of Aeolus on the surface wind forecasts for the region > 60° S is nearly neutral when conducting the assessments for the whole year of 2020 (Figure 5.8 (b)). This is partly caused by the sparse weather stations in Antarctica.

Moreover, the NWP model may behave differently for the region > 60° S because the ice sheets and mountainous terrain in Antarctica are poorly resolved due to the coarse model resolution (Bromwich et al., 2005), which impairs the impact of Aeolus on the surface wind forecasts. With respect to the results for two half years, more error reductions are found for the first half of 2020 than the second half, within T+96 h and at T+216 h and T+240 h for the *u* component and wind speed, suggesting the importance of the Aeolus data quality for near-surface wind forecasts.

In summary, in situ data-based assessments were performed to understand the value of Aeolus for surface wind forecasts over high-latitude lands to achieve **Objective 3**. Aeolus wind assimilation can improve surface wind forecasts for the region > 60° N, particularly during the first half of 2020, the boreal winter months, and the stormy conditions. For the region > 60° S, the overall contribution of Aeolus to surface wind forecasts is limited although more error reductions are found for the first half of 2020. These results partly agree with the corresponding hypotheses.

The research findings presented in Section 5.2 and Section 5.3 are based on the longest ECMWF OSEs covering the FM-B period from June 2019 to September 2021. It would be interesting to perform similar investigations for FM-A periods using the latest OSEs based on the third reprocessed data set (4 September 2018 – 4 June 2019) or the late 2022/early 2023 NRT data set. Referring to the analysis-based verifications at the ECMWF, Aeolus also has the ability to contribute to surface wind forecasts during the FM-A periods, particularly from late 2022 to early 2023 (Rennie & Isaksen, 2023).

6 Conclusions

This PhD project aims to assess the performance of the first space-borne Doppler wind lidar on Aeolus satellite in wind profile detection and its contribution to near-surface wind forecasts. To achieve the goal, three main objectives were defined: (i) to evaluate Aeolus wind observations over Australia to complement the validations for the Southern Hemisphere; (ii) to understand the impact of Aeolus wind assimilation on global sea surface wind forecasts geographically; (iii) to evaluate the contribution of Aeolus winds to near-surface wind forecasts over high-latitude lands in both hemispheres.

Aeolus HLOS wind profiles over Australia were validated by taking wind profiling radar measurements as reference data. The inter-comparison analysis demonstrates that Aeolus winds are in good agreement with the ground-based radar measurements, and the mean biases of both Rayleigh-clear and Mie-cloudy winds achieve the mission requirement of 0.7 m s^{-1}. In terms of precision, the overall random errors of Rayleigh-clear and Mie-cloudy winds are 5.81 m s^{-1} and 4.14 m s^{-1}, respectively, indicating the higher precision of Mie-cloudy winds than Rayleigh-clear winds. The precisions derived from triple collocation analysis based on the Aeolus, ground-based radar, and ECMWF model data are comparable with the results of inter-comparison analysis, with error standard deviations of 5.61 m s^{-1} for Rayleigh-clear winds and 3.50 m s^{-1} for Mie-cloudy winds. However, the wind measurements from both channels fail to meet the required mission precision. Furthermore, compared to the Rayleigh channel, the Mie channel is found to be better at capturing wind information below 1,500 m, implying a greater impact of Mie-cloudy winds on data assimilation in the planetary boundary layer.

By comparing the ECMWF OSE forecasts (with Aeolus/no Aeolus) to sea surface wind observations from satellite scatterometers and ocean buoys, the evaluations demonstrate that Aeolus can slightly improve the short-range sea surface wind forecasts for the global ocean except for the tropical regions. Moreover, Aeolus can reduce the large-scale zonal wind biases of short-range forecasts, while the influence on meridional wind biases varies with regions. As the forecast step is extended, Aeolus tends to make a greater contribution to sea surface wind forecasts up to T+120 h, particularly for the extratropical ocean regions in the Southern Hemisphere.

With respect to the high-latitude lands, the investigations were performed by comparing to near-surface wind measurements from weather stations. Aeolus data assimilation can improve near-surface wind forecasts for the region > 60° N. This positive impact becomes more evident as the forecast step is extended. Moreover, the wind forecast improvement is associated with Aeolus data quality and wind speed, with the larger improvements obtained during the first half-year of 2020 and during the boreal winter (December, January, and February) and stormy conditions. In

addition, the meridional wind component generally benefits more from the Aeolus wind assimilation than the zonal wind component. However, for the region > 60° S, the contribution of Aeolus to surface wind forecasts is limited overall.

This PhD study partly complements the validation efforts for Aeolus wind observations in the Southern Hemisphere and expands our understanding of the value of assimilating Aeolus winds into the global NWP model on near-surface wind forecasts. The outcome of this PhD study offers promising indications of Aeolus' potential in improving wind forecasts for the surface layer. Moreover, the insights gained can serve as valuable guidance for generating high-quality and high-resolution wind information for limited areas, thereby benefiting wind-related applications, such as wind power predictions and wind farm operations.

7 Outlook

Beyond the scope of this PhD thesis, several potential extensions of the research could be pursued in the future.

With the development of Aeolus wind retrieval algorithm, improved Rayleigh-cloudy winds have been available since 16 February 2023 (ESA, 2023b). It would be interesting to investigate their error characteristics and compare them with the errors from Mie-cloudy winds.

Due to the time constraint, the assessments for medium-range ocean surface forecasts based on Aeolus impact experiments were only performed at forecast steps with a 24-h time interval, which makes only two data bands available on the maps. To increase the data coverage, future studies could be carried out for a forecast range with a shorter time interval, such as from T+12 h to T+36 h with a 6-h time interval instead of only at the T+24 h forecast step. This would increase the data bands to four for a polar-orbiting satellite.

In this PhD study, the impacts of Aeolus on surface wind forecasts were investigated using the ECMWF OSEs based on the second reprocessed Aeolus L2B baseline 11 and NRT baseline 11/12 wind products. It was the latest and longest OSE when performing this research. As the new OSEs based on the FM-A periods become available, similar studies could be carried out to assess the value of the Aeolus winds during the FM-A periods on surface layer wind forecasts.

Derived from the current research, it remains to explore whether the improved wind forecasts in the ECMWF model will benefit the performance of regional models on surface layer wind forecasts. For example, given the relatively large wind forecast improvement over the southwest Atlantic based on the ECMWF OSEs, an investigation could be conducted for the coastal regions of southeast South America using a regional model, such as Weather Research and Forecasting model, with ECMWF data (with Aeolus) as initial and boundary conditions. Furthermore, regarding the applications in the wind energy sector, how much influence the Aeolus-improved forecasts would make on wind power predictions needs to be quantified.

In addition, over the past few years, most evaluations focused on the impact of Aeolus wind assimilation on wind and temperature forecasts. The contribution of Aeolus to the forecasts for other environmental parameters, such as precipitation, is also noteworthy for investigation.

Aeolus, as an experimental satellite, has demonstrated the ability of spaceborne DWL in global wind profile detection and the value for improving NWPs. The mission has ended since April 2023, while the Aeolus follow-on mission is under preparation for operational use (Mason, 2022). A series of two satellites is planned to be first launched in 2030, and the two satellites together are intended to provide over 10 years of operational and global wind profile

observations. Moreover, with the lessons learnt from the past Aeolus mission and the advancement in techniques, wind profiles acquired by the future spaceborne DWL(s) are believed to have better data quality with higher horizontal and/or vertical resolution. In turn, the potential contributions of global wind profiles to generating high-quality wind data and to practical applications for various industries would be promising in the future.

8 References

Aeolus Data Innovation and Science Cluster (DISC). (2020). *Summary of Quality of Aeolus Data Products from 1st Reprocessing Campaign covering June to December 2019*. ESA. https://earth.esa.int/eogateway/documents/20142/0/Aeolus-Summary-Reprocessing-1-DISC.pdf

Ahrens, C. D. (2009). Wind: Small Scale and Local Systems. In *Meteorology Today: An Introduction to Weather, Climate, and the Environment* (Ninth, pp. 223–257). Brooks/Cole, Cengage Learning.

Amiridis, V., Kampouri, A., Gkikas, A., Misios, S., Gialitaki, A., Marinou, E., Rennie, M., Benedetti, A., Solomos, S., Zanis, P., Vasardani, O., Eleftheratos, K., Paschou, P., Georgiou, T., Scollo, S., Mona, L., Papagiannopoulos, N., Retscher, C., Parrinello, T., & Straume, A. G. (2023). Aeolus winds impact on volcanic ash early warning systems for aviation. *Scientific Reports*, *13*(1), 7531. https://doi.org/10.1038/s41598-023-34715-6

Andersson, E., Dabas, A., Endemann, M., Ingmann, P., Källén, E., Offiler, D., & Stoffelen, A. (2008). *ADM-Aeolus Science Report* (SP-1311; pp. 1–121). ESA. https://esamultimedia.esa.int/multimedia/publications/SP-1311/SP-1311.pdf

Angelou, N., Karagali, I., Santos, P., Badger, M., Hahmann, A., Hasager, C. B., Peña, A., & Mann, J. (2019, May 16). *First results of Aeolus comparison to a ground-based Wind Lidar at Alaiz (Spain)* [Conference]. European Space Agency's 2019 Living Planet Symposium, Milan, Italy. https://orbit.dtu.dk/en/activities/first-results-of-aeolus-comparison-to-a-ground-based-wind-lidar-a

Baars, H., Herzog, A., Heese, B., Ohneiser, K., Hanbuch, K., Hofer, J., Yin, Z., Engelmann, R., & Wandinger, U. (2020). Validation of Aeolus wind products above the Atlantic Ocean. *Atmospheric Measurement Techniques*, *13*(11), 6007–6024. https://doi.org/10.5194/amt-13-6007-2020

Banyard, T. P., Wright, C. J., Hindley, N. P., Halloran, G., Krisch, I., Kaifler, B., & Hoffmann, L. (2021). Atmospheric Gravity Waves in Aeolus Wind Lidar Observations. *Geophysical Research Letters*, *48*(10). https://doi.org/10.1029/2021GL092756

Belova, E., Kirkwood, S., Voelger, P., Chatterjee, S., Satheesan, K., Hagelin, S., Lindskog, M., & Körnich, H. (2021). Validation of Aeolus winds using ground-based radars in Antarctica and in northern Sweden. *Atmospheric Measurement Techniques*, *14*(8), 5415–5428. https://doi.org/10.5194/amt-14-5415-2021

Bettenhausen, M. H., Smith, C. K., Bevilacqua, R. M., Nai-Yu Wang, Gaiser, P. W., & Cox, S. (2006). A nonlinear optimization algorithm for WindSat wind vector retrievals. *IEEE Transactions on Geoscience and Remote Sensing*, *44*(3), 597–610. https://doi.org/10.1109/TGRS.2005.862504

Bidlot, J.-R., Holmes, D. J., Wittmann, P. A., Lalbeharry, R., & Chen, H. S. (2002). Intercomparison of the Performance of Operational Ocean Wave Forecasting Systems with Buoy Data. *Weather and Forecasting*, *17*(2), 287–310. https://doi.org/10.1175/1520-0434(2002)017<0287:IOTPOO>2.0.CO;2

Borne, M., Knippertz, P., Weissmann, M., Martin, A., Rennie, M., & Cress, A. (2023). Impact of Aeolus wind lidar observations on the representation of the West African monsoon

circulation in the ECMWF and DWD forecasting systems. *Quarterly Journal of the Royal Meteorological Society*, *149*(752), 933–958. https://doi.org/10.1002/qj.4442

Bromwich, D. H., Monaghan, A. J., Manning, K. W., & Powers, J. G. (2005). Real-Time Forecasting for the Antarctic: An Evaluation of the Antarctic Mesoscale Prediction System (AMPS). *Monthly Weather Review*, *133*(3), 579–603. https://doi.org/10.1175/MWR-2881.1

Calvert, J. G. (1990). Glossary of atmospheric chemistry terms (Recommendations 1990). *Pure and Applied Chemistry*, *62*(11), 2167–2219. https://doi.org/10.1351/pac199062112167

Charlton, A. J., Oneill, A., Lahoz, W. A., & Massacand, A. C. (2004). Sensitivity of tropospheric forecasts to stratospheric initial conditions. *Quarterly Journal of the Royal Meteorological Society*, *130*(600), 1771–1792. https://doi.org/10.1256/qj.03.167

Christiansen, B. (2001). Downward propagation of zonal mean zonal wind anomalies from the stratosphere to the troposphere: Model and reanalysis. *Journal of Geophysical Research: Atmospheres*, *106*(D21), 27307–27322. https://doi.org/10.1029/2000JD000214

de Kloe, J., Stoffelen, A., Tan, D., Andersson, E., Rennie, M., Dabas, A., Poli, P., & Huber, D. (2021). *Aeolus Data Innovation Science Cluster DISC ADM-Aeolus Level-2B/2C Processor Input/Output Data Definitions Interface Control Document*. ESA. https://earth.esa.int/eogateway/documents/20142/37627/Aeolus-L2B-2C-Input-Output-DD-ICD.pdf

Dolman, B. K., Reid, I. M., & Tingwell, C. (2018). Stratospheric tropospheric wind profiling radars in the Australian network. *Earth, Planets and Space*, *70*(1), 170. https://doi.org/10.1186/s40623-018-0944-z

Dolman, B., Reid, I., & Kane, T. (2016). *The Australian Wind Profiler Network*. WMO Technical Conference on Meteorological and Environmental Instruments and Methods of Observation (TECO-2016), Madrid, Spain. https://www.wmocimo.net/eventpapers/session2/O2(3)_Dolman_The%20Australian%20Wind%20Profiler%20Network.pdf

ECMWF, & Brazilian National Institute for Space Research. (2023). *Metview* (5.18.0) [Computer software]. https://metview.readthedocs.io/en/latest/index.html

ECMWF Research Department. (2022). *ECMWF Research Experiments (RD)* [dataset]. https://www.ecmwf.int/en/forecasts/dataset/ecmwf-research-experiments

ESA. (n.d.). *MetOp (Meteorological Operational Satellite Program of Europe)*. Retrieved 8 August 2023, from https://www.eoportal.org/satellite-missions/metop#mission-status

ESA. (2021a). *ESA Aeolus Online Dissemination* [dataset]. https://aeolus-ds.eo.esa.int/oads/access/

ESA. (2020). *A Guide to Aeolus Range Bin Settings*. Earth Online. https://earth.esa.int/eogateway/news/a-guide-to-aeolus-range-bin-settings

ESA. (2021b). *Aeolus Data Now in Use by Four of Europe's Biggest Meteorological Services*. https://earth.esa.int/eogateway/news/aeolus-data-now-in-use-by-three-of-europe-s-biggest-meteorological-services

ESA. (2023a). *ALADIN Processor Releases*. https://earth.esa.int/eogateway/instruments/aladin/processor-releases

ESA. (2023b). *Improved Aeolus Rayleigh-cloudy winds product now available*. https://earth.esa.int/eogateway/news/improved-aeolus-rayleigh-cloudy-winds-product-now-available

E.U. Copernicus Marine Service Information. (n.d.). *Global Ocean Daily Gridded Sea Surface Winds from Scatterometer* [dataset]. https://doi.org/10.48670/moi-00182

EUMETSAT. (2022). *ASCAT User Guide*. EUMETSAT. https://www-cdn.eumetsat.int/files/2022-12/ASCAT%20User%20Guide.pdf

EUMETSAT NWP SAF. (2020). *ASCAT Wind Data Processor* (v3.3) [Computer software]. https://nwp-saf.eumetsat.int/site/software/scatterometer/awdp/

EUMETSAT NWP SAF. (2022). *Pencil Beam Wind Processor* (v4.0) [Computer software]. https://nwp-saf.eumetsat.int/site/software/scatterometer/penwp/

EUMETSAT SAF on Ocean and Sea Ice. (2009). *ASCAT Winds and Soil Moisture at 25 km Swath Grid—Metop* [Dataset]. https://navigator.eumetsat.int/product/EO:EUM:DAT:METOP:OAS025

EUMETSAT SAF on Ocean and Sea Ice. (2021). *HSCAT Winds at 25 km Swath Grid—Hai Yang 2B* [Dateset]. https://doi.org/10.15770/EUM_SAF_OSI_NRT_2000

Forsythe, M. (2008). *Atmospheric Motion Vectors: Past, Present and Future*. Seminar on Recent developments in the use of satellite observations in numerical weather prediction, Shinfield Park, Reading. https://www.ecmwf.int/en/elibrary/74512-atmospheric-motion-vectors-past-present-and-future

Forsythe, M., & Halloran, G. (2022, September 8). *Impact of Aeolus Doppler Wind Lidar at the UK Met Office*. Towards an operational Doppler Wind Lidar Programm, Darmstadt, Germany. https://www.eventsforce.net/eumetsat/frontend/reg/tAgendaWebsite.csp?pageID=15588&ef_sel_menu=247&eventID=38&mode=

Gao, C., Li, Y., & Chen, H. (2019). Diurnal Variations of Different Cloud Types and the Relationship between the Diurnal Variations of Clouds and Precipitation in Central and East China. *Atmosphere*, *10*(6), 304. https://doi.org/10.3390/atmos10060304

Garrett, K., Liu, H., Ide, K., Hoffman, R. N., & Lukens, K. E. (2022). Optimization and impact assessment of Aeolus HLOS wind assimilation in NOAA's global forecast system. *Quarterly Journal of the Royal Meteorological Society*, *148*(747), 2703–2716. https://doi.org/10.1002/qj.4331

Goodberlet, M. A., Swift, C. T., & Wilkerson, J. C. (1990). Ocean surface wind speed measurements of the Special Sensor Microwave/Imager (SSM/I). *IEEE Transactions on Geoscience and Remote Sensing*, *28*(5), 823–828. https://doi.org/10.1109/36.58969

Guo, J., Liu, B., Gong, W., Shi, L., Zhang, Y., Ma, Y., Zhang, J., Chen, T., Bai, K., Stoffelen, A., de Leeuw, G., & Xu, X. (2021). Technical note: First comparison of wind observations from ESA's satellite mission Aeolus and ground-based radar wind profiler network of China. *Atmospheric Chemistry and Physics*, *21*(4), 2945–2958. https://doi.org/10.5194/acp-21-2945-2021

Ingleby, B. (2016). *On the accuracy of different radiosonde types*. 1–10. https://www.wmocimo.net/eventpapers/session4/O4(8)_Ingleby_RadiosondeTypes.pdf

Ingleby, B. (2023). *Data availability*. https://confluence.ecmwf.int/display/TCBUF/Data+availability

Ingmann, P., & Straume, A. G. (2016). *ADM-Aeolus Mission Requirements Document*. ESA. https://esamultimedia.esa.int/docs/EarthObservation/ADM-Aeolus_MRD.pdf

Iwai, H., Aoki, M., Oshiro, M., & Ishii, S. (2021). Validation of Aeolus Level 2B wind products using wind profilers, ground-based Doppler wind lidars, and radiosondes in Japan. *Atmospheric Measurement Techniques*, *14*(11), 7255–7275. https://doi.org/10.5194/amt-14-7255-2021

Kodera, K., Yamazaki, K., Chiba, M., & Shibata, K. (1990). Downward propagation of upper stratospheric mean zonal wind perturbation to the troposphere. *Geophysical Research Letters*, *17*(9), 1263–1266. https://doi.org/10.1029/GL017i009p01263

Kramer, H. J. (2012). *QuikSCAT*. https://www.eoportal.org/satellite-missions/quikscat#references

Krisna, T. C., & Wernham, D. (2023, May 22). *In-Orbit Performance of the ALADIN Instrument*. Aeolus Science Conference 2023, Rhodes Island, Greece. https://az659834.vo.msecnd.net/eventsairwesteuprod/production-nikal-public/9d8d8d83582b411eb60e612f0f502914

Krisna, T., & Wernham, D. (2023, May 22). *In-Orbit Performance of the ALADIN Instrument*. Aeolus Science Conference 2023, Rhodes Island, Greece. https://az659834.vo.msecnd.net/eventsairwesteuprod/production-nikal-public/9d8d8d83582b411eb60e612f0f502914

Laroche, S., & St-James, J. (2022). Impact of the Aeolus Level-2B horizontal line-of-sight winds in the Environment and Climate Change Canada global forecast system. *Quarterly Journal of the Royal Meteorological Society*, *148*(745), 2047–2062. https://doi.org/10.1002/qj.4300

Lee, S., Song, H., Kwon, I., & Kang, J. (2023). Impacts of Aeolus horizontal LINE-OF-SIGHT (HLOS) wind assimilation on the Korean integrated model (KIM) forecast system. *Atmospheric Science Letters*, *24*(3). https://doi.org/10.1002/asl.1138

Lehmann, V., & Brown, W. (2021). Radar Wind Profiler. In T. Foken (Ed.), *Springer Handbook of Atmospheric Measurements* (pp. 901–933). Springer, Cham. https://doi.org/10.1007/978-3-030-52171-4_31

Lin, W., Portabella, M., Stoffelen, A., Vogelzang, J., & Verhoef, A. (2016). On mesoscale analysis and ASCAT ambiguity removal. *Quarterly Journal of the Royal Meteorological Society*, *142*(697), 1745–1756. https://doi.org/10.1002/qj.2770

Liu, S., Lin, W., Portabella, M., & Wang, Z. (2022). Characterization of Tropical Cyclone Intensity Using the HY-2B Scatterometer Wind Data. *Remote Sensing*, *14*(4), 1035. https://doi.org/10.3390/rs14041035

Liu, Z., Barlow, J. F., Chan, P.-W., Fung, J. C. H., Li, Y., Ren, C., Mak, H. W. L., & Ng, E. (2019). A Review of Progress and Applications of Pulsed Doppler Wind LiDARs. *Remote Sensing*, *11*(21), 2522. https://doi.org/10.3390/rs11212522

Lorenz, E. N. (1963). Deterministic Nonperiodic Flow. *Journal of the Atmospheric Sciences*, *20*(2), 130–141. https://doi.org/10.1175/1520-0469(1963)020<0130:DNF>2.0.CO;2

Martin, A., Weissmann, M., Reitebuch, O., Rennie, M., Geiß, A., & Cress, A. (2021). Validation of Aeolus winds using radiosonde observations and numerical weather prediction model equivalents. *Atmospheric Measurement Techniques*, *14*(3), 2167–2183. https://doi.org/10.5194/amt-14-2167-2021

Mason, G. (2022, September 8). *Towards an Operational DWL Programme – ESA Aeolus-2 Programme –*. Towards an operational Doppler Wind Lidar Programm, Darmstadt, Germany. https://www.eventsforce.net/eumetsat/frontend/reg/thome.csp?pageID=15575&eventID=38&traceRedir=2

Met Office. (2008). *Wind Profiler Observations, Part of the Met Office MetDB System, NCAS British Atmospheric Data Centre [data set]*. NCAS British Atmospheric Data Centre. https://catalogue.ceda.ac.uk/uuid/9e22544a66ba7aa902ae431b1ed609d6

Mile, M., Azad, R., & Marseille, G. (2022). Assimilation of Aeolus Rayleigh-Clear Winds Using a Footprint Operator in AROME-Arctic Mesoscale Model. *Geophysical Research Letters*, *49*(10), 1–11. https://doi.org/10.1029/2021GL097615

Minin, V. A., & Furtaev, A. I. (2019). Principal Directions of the Wind Energy Possible Use in the Western Sector of the Russian Arctic. *2019 International Multi-Conference on Industrial Engineering and Modern Technologies (FarEastCon)*, 1–6. https://doi.org/10.1109/FarEastCon.2019.8933878

National Centers for Environmental Information. (n.d.). *Global Hourly—Integrated Surface Database (ISD)* [dataset]. Retrieved 11 August 2022, from https://www.ncei.noaa.gov/products/land-based-station/integrated-surface-database#:~:text=Global%20Climate%20Station%20Summaries%20Summaries%20are%20simple%20indicators,or%20longer%20time%20periods%20or%20for%20customized%20periods.

National Oceanic and Atmospheric Administration. (2023). *Radiosondes*. https://www.noaa.gov/jetstream/upperair/radiosondes

National Satellite Ocean Application Service. (n.d.). *HY-2B*. Retrieved 11 August 2023, from http://www.nsoas.org.cn/eng/item/206.html

Ocean and Sea Ice Satellite Application Facilities/EUMETSAT Advanced Retransmission Service Winds Team. (2021). *ASCAT Wind Product User Manual*. EUMETSAT. https://scatterometer.knmi.nl/publications/pdf/ASCAT_Product_Manual.pdf

OSI SAF Winds Team. (2021). *Product User Manual (PUM) for the HY-2 winds*. EUMETSAT. https://scatterometer.knmi.nl/publications/pdf/osisaf_cdop3_ss3_pum_hy-2_winds.pdf

Pacific Marine Environmental Laboratory. (n.d.). *Global Tropical Moored Buoy Array* [dataset]. Retrieved 3 August 2022, from https://www.pmel.noaa.gov/gtmba/

Pourret, V., Šavli, M., Mahfouf, J., Raspaud, D., Doerenbecher, A., Bénichou, H., & Payan, C. (2022). Operational assimilation of Aeolus winds in the Météo-France global NWP model ARPEGE. *Quarterly Journal of the Royal Meteorological Society*, *148*(747), 2652–2671. https://doi.org/10.1002/qj.4329

Prósper, M. A., Otero-Casal, C., Fernández, F. C., & Miguez-Macho, G. (2019). Wind power forecasting for a real onshore wind farm on complex terrain using WRF high resolution simulations. *Renewable Energy*, *135*, 674–686. https://doi.org/10.1016/j.renene.2018.12.047

Pryor, S. C., & Barthelmie, R. J. (2021). A global assessment of extreme wind speeds for wind energy applications. *Nature Energy*, *6*(3), 268–276. https://doi.org/10.1038/s41560-020-00773-7

Pu, Z., & Kalnay, E. (2018). Numerical Weather Prediction Basics: Models, Numerical Methods, and Data Assimilation. In Q. Duan, F. Pappenberger, J. Thielen, A. Wood, H. Cloke, & J. Schaake (Eds.), *Handbook of Hydrometeorological Ensemble Forecasting* (pp. 1–31). Springer.

Ratynski, M., Khaykin, S., Hauchecorne, A., Wing, R., Cammas, J.-P., Hello, Y., & Keckhut, P. (2023). Validation of Aeolus wind profiles using ground-based lidar and radiosonde observations at Réunion island and the Observatoire de Haute-Provence. *Atmospheric Measurement Techniques*, *16*(4), 997–1016. https://doi.org/10.5194/amt-16-997-2023

Reitebuch, O., Krisch, I., Lemmerz, C., Lux, O., Marksteiner, U., Masoumzadeh, N., Weiler, F., Witschas, B., Filomarino, V. C., Meringer, M., Schmidt, K., Huber, D., Nikolaus, I., Fabre, F., Vaughan, M., Reissig, K., Dabas, A., Flament, T., Lacour, A., … Parrinello, T. (2022, March 28). *Contributions from the DISC to accomplish the Aeolus mission objectives* [Conference or Workshop Item (Speech)]. Aeolus 3rd Anniversary Conference, Taormina, Italien. https://elib.dlr.de/186034/

Rennie, M., & Isaksen, L. (2023). *The NWP impact of Aeolus Level-2B winds at ECMWF* (AED-TN-ECMWF-NWP-025; p. 265). ECMWF. https://confluence.ecmwf.int/display/AEOL/L2B+team+technical+reports+and+relevant+papers?preview=/46596815/348788257/AED-TN-ECMWF-NWP-025--20230809_v7.0.pdf

Rennie, M., Isaksen, L., Weiler, F., de Kloe, J., Kanitz, T., & Reitebuch, O. (2021). The impact of Aeolus wind retrievals on ECMWF global weather forecasts. *Quarterly Journal of the Royal Meteorological Society*, *147*(740), 3555–3586. https://doi.org/10.1002/qj.4142

Ribal, A., & Young, I. R. (2020). Global Calibration and Error Estimation of Altimeter, Scatterometer, and Radiometer Wind Speed Using Triple Collocation. *Remote Sensing*, *12*(12), 1997. https://doi.org/10.3390/rs12121997

Ruppert, D. (2011). *Statistics and Data Analysis for Financial Engineering* (1st ed.). Springer. https://doi.org/10.1007/978-1-4419-7787-8

Salonen, K., Cotton, J., Bormann, N., & Forsythe, M. (2015). Characterizing AMV Height-Assignment Error by Comparing Best-Fit Pressure Statistics from the Met Office and ECMWF Data Assimilation Systems. *Journal of Applied Meteorology and Climatology*, *54*(1), 225–242. https://www.jstor.org/stable/26176489

Sandu, I., Bechtold, P., Nuijens, L., Beljaars, A., & Brown, A. (2020). *On the causes of systematic forecast biases in near-surface wind direction over the oceans*. ECMWF. https://www.ecmwf.int/sites/default/files/elibrary/2020/19545-causes-systematic-forecast-biases-near-surface-wind-direction-over-oceans.pdf

Skamarock, W. C. (2004). Evaluating Mesoscale NWP Models Using Kinetic Energy Spectra. *Monthly Weather Review*, *132*(12), 3019–3032. https://doi.org/10.1175/MWR2830.1

Stoffelen, A. (1998). Toward the true near-surface wind speed: Error modeling and calibration using triple collocation. *Journal of Geophysical Research: Oceans*, *103*(C4), 7755–7766. https://doi.org/10.1029/97JC03180

Stoffelen, A., Benedetti, A., Borde, R., Dabas, A., Flamant, P., Forsythe, M., Hardesty, M., Isaksen, L., Källén, E., Körnich, H., Lee, T., Reitebuch, O., Rennie, M., Riishøjgaard, L.-P., Schyberg, H., Straume, A. G., & Vaughan, M. (2020). Wind Profile Satellite

Observation Requirements and Capabilities. *Bulletin of the American Meteorological Society*, *101*(11), E2005–E2021. https://doi.org/10.1175/BAMS-D-18-0202.1

Stoffelen, A., Vogelzang, J., & Marseille, G.-J. (2020). *High-resolution wind data-assimilation guide*. EUMETSAT OSI SAF. https://nwp-saf.eumetsat.int/site/download/documentation/scatterometer/reports/High_Resolution_Wind_Data_Assimilation_Guide_1.3.pdf

Straume-Lindner, A. G. (2018). *Aeolus Sensor and Product Description*. ESA. https://earth.esa.int/eogateway/documents/20142/37627/Aeolus-Sensor-and-Product-Description.pdf

Straume-Lindner, A. G., Parrinello, T., Von Bismarck, J., Bley, S., Wernham, D., Kanitz, T., Alvarez, E., Fischey, P., De Laurentis, M., Fehr, T., Ehlers, F., Duc Tran, V., Krisch, I., Reitebuch, O., & Renni, M. (2021). ESA'S Wind Mission Aeolus—Overview, Status and Outlook. *2021 IEEE International Geoscience and Remote Sensing Symposium IGARSS*, 755–758. https://doi.org/10.1109/IGARSS47720.2021.9554007

Stull, R. (2017a). Numerical Weather Prediction (NWP). In *Practical Meteorology: An Algebra-based Survey of Atmospheric Science* (1.02b, pp. 745–792). University of British Columbia. https://www.eoas.ubc.ca/books/Practical_Meteorology/

Stull, R. (2017b). REGIONAL WINDS. In *Practical Meteorology: An Algebra-based Survey of Atmospheric Science* (v1.02, pp. 645–686). University of British Columbia. https://www.eoas.ubc.ca/books/Practical_Meteorology/

Tan, D. G. H., Andersson, E., de Kloe, J., Marseille, G.-J., Stoffelen, A., Poli, P., Denneulin, M.-L., Dabas, A., Huber, D., Reitebuch, O., Flamant, P., Le Rille, O., & Nett, H. (2008). The ADM-Aeolus wind retrieval algorithms. *Tellus A: Dynamic Meteorology and Oceanography*, *60*(2), 191. https://doi.org/10.1111/j.1600-0870.2007.00285.x

Tozer, B., Sandwell, D. T., Smith, W. H. F., Olson, C., Beale, J. R., & Wessel, P. (2019). Global Bathymetry and Topography at 15 Arc Sec: SRTM15+. *Earth and Space Science*, *6*(10), 1847–1864. https://doi.org/10.1029/2019EA000658

Tripathi, O. P., Baldwin, M., Charlton-Perez, A., Charron, M., Eckermann, S. D., Gerber, E., Harrison, R. G., Jackson, D. R., Kim, B., Kuroda, Y., Lang, A., Mahmood, S., Mizuta, R., Roff, G., Sigmond, M., & Son, S. (2015). The predictability of the extratropical stratosphere on monthly time-scales and its impact on the skill of tropospheric forecasts. *Quarterly Journal of the Royal Meteorological Society*, *141*(689), 987–1003. https://doi.org/10.1002/qj.2432

Uieda, L., Tian, D., Leong, W. J., Jones, M., Schlitzer, Toney, L., Grund, M., Yao, J., Magen, Y., Materna, K., Newton, T., Anant, A., Ziebarth, M., Wessel, P., & Quinn, J. (2021). *PyGMT: A Python interface for the Generic Mapping Tools* (v0.5.0) [Computer software]. Zenodo. https://doi.org/10.5281/ZENODO.5607255

Vallejos-Burgos, F., Coudert, F.-X., & Kaneko, K. (2018). Air separation with graphene mediated by nanowindow-rim concerted motion. *Nature Communications*, *9*(1), 1812. https://doi.org/10.1038/s41467-018-04224-6

Vogelzang, J., & Stoffelen, A. (2012). *Triple collocation*. EUMETSAT. https://cdn.knmi.nl/system/data_center_publications/files/000/068/914/original/triplecollocation_nwpsaf_tr_kn_021_v1.0.pdf?1495621500

Vogelzang, J., & Stoffelen, A. (2021). Quadruple Collocation Analysis of In-Situ, Scatterometer, and NWP Winds. *Journal of Geophysical Research: Oceans*, *126*(5). https://doi.org/10.1029/2021JC017189

Wallace, J. M., & Hobbs, P. V. (2006). Cloud Microphysics. In *Atmospheric Science An Introductory Survey* (2nd ed., Vol. 92, pp. 209–263). Elsevier.

Wang, Z., Stoffelen, A., Zou, J., Lin, W., Verhoef, A., Zhang, Y., He, Y., & Lin, M. (2020). Validation of New Sea Surface Wind Products From Scatterometers Onboard the HY-2B and MetOp-C Satellites. *IEEE Transactions on Geoscience and Remote Sensing*, *58*(6), 4387–4394. https://doi.org/10.1109/TGRS.2019.2963690

Wessel, P., Luis, J. F., Uieda, L., Scharroo, R., Wobbe, F., Smith, W. H. F., & Tian, D. (2019). The Generic Mapping Tools Version 6. *Geochemistry, Geophysics, Geosystems*, *20*(11), 5556–5564. https://doi.org/10.1029/2019GC008515

Witschas, B., Lemmerz, C., Geiß, A., Lux, O., Marksteiner, U., Rahm, S., Reitebuch, O., Schäfler, A., & Weiler, F. (2022). Validation of the Aeolus L2B wind product with airborne wind lidar measurements in the polar North Atlantic region and in the tropics. *Atmospheric Measurement Techniques*, *15*(23), 7049–7070. https://doi.org/10.5194/amt-15-7049-2022

Wood, R. (2012). Stratocumulus Clouds. *Monthly Weather Review*, *140*(8), 2373–2423. https://doi.org/10.1175/MWR-D-11-00121.1

World Meteorological Organization (WMO). (2020). *Vision for the WMO Integrated Global Observing System in 2040*. https://library.wmo.int/index.php?lvl=notice_display&id=21716

World Meteorological Organization (WMO). (2022). *AMDAR Observing System*. https://public.wmo.int/en/programmes/global-observing-system/amdar-observing-system

World Meteorological Organization (WMO). (2022). *Global Observing System*. https://public.wmo.int/en/programmes/global-observing-system

Žagar, N., Rennie, M., & Isaksen, L. (2021). Uncertainties in Kelvin Waves in ECMWF Analyses and Forecasts: Insights From Aeolus Observing System Experiments. *Geophysical Research Letters*, *48*(22). https://doi.org/10.1029/2021GL094716

Zhang, W., Guo, J., Miao, Y., Liu, H., Zhang, Y., Li, Z., & Zhai, P. (2016). Planetary boundary layer height from CALIOP compared to radiosonde over China. *Atmospheric Chemistry and Physics*, *16*(15), 9951–9963. https://doi.org/10.5194/acp-16-9951-2016

Zuo, H., & Hasager, C. B. (2023). The impact of Aeolus winds on near-surface wind forecasts over tropical ocean and high-latitude regions. *Atmospheric Measurement Techniques*, *16*, 3901–3913. https://doi.org/10.5194/amt-16-3901-2023

Zuo, H., Hasager, C. B., Karagali, I., Stoffelen, A., Marseille, G.-J., & de Kloe, J. (2022). Evaluation of Aeolus L2B wind product with wind profiling radar measurements and numerical weather prediction model equivalents over Australia. *Atmospheric Measurement Techniques*, *15*(13), 4107–4124. https://doi.org/10.5194/amt-15-4107-2022

Zuo, H., Stoffelen, A., Rennie, M., & Hasager, C. B. (2023). *The Contribution of Aeolus Wind Observations to ECMWF Sea Surface Wind Forecasts* [Manuscript submitted for publication].

Part II Appendix

A Publication contributions

A.1 Article I: Evaluation of Aeolus L2B wind product with wind profiling radar measurements and numerical weather prediction model equivalents over Australia

Zuo, H., Hasager, C. B., Karagali, I., Stoffelen, A., Marseille, G.-J., & de Kloe, J. (2022). Evaluation of Aeolus L2B wind product with wind profiling radar measurements and numerical weather prediction model equivalents over Australia. *Atmospheric Measurement Techniques*, *15*(13), 4107–4124. https://doi.org/10.5194/amt-15-4107-2022

Atmos. Meas. Tech., 15, 4107–4124, 2022
https://doi.org/10.5194/amt-15-4107-2022

Atmospheric Measurement Techniques
Open Access
EGU

Evaluation of Aeolus L2B wind product with wind profiling radar measurements and numerical weather prediction model equivalents over Australia

Haichen Zuo[1], Charlotte Bay Hasager[1], Ioanna Karagali[2], Ad Stoffelen[3], Gert-Jan Marseille[3], and Jos de Kloe[3]

[1]Department of Wind and Energy Systems, Technical University of Denmark, Roskilde, 4000, Denmark
[2]National Centre for Climate Research, Danish Meteorological Institute, Copenhagen, 2100, Denmark
[3]Research & Development Satellite Observations, Royal Netherlands Meteorological Institute, De Bilt, 3730 AE, the Netherlands

Correspondence: Haichen Zuo (hazu@dtu.dk)

Received: 23 February 2022 – Discussion started: 25 February 2022
Revised: 30 May 2022 – Accepted: 14 June 2022 – Published: 15 July 2022

Abstract. Carrying a laser Doppler instrument, the Aeolus satellite was launched in 2018, becoming the first mission for atmospheric wind profile measurements from space. Before utilizing the Aeolus winds for different applications, evaluating their data quality is essential. With the help of ground-based wind profiling radar measurements and the European Centre for Medium-Range Weather Forecasts (ECMWF) model equivalents, this study quantifies the error characteristics of Aeolus L2B (baseline-11) near-real-time horizontal line-of-sight winds across Australia during October 2020–March 2021 by using both inter-comparison and triple collocation analysis. The results of the inter-comparison analysis indicate that both Rayleigh-clear winds and Mie-cloudy winds are in good agreement with the ground-based radar measurements with overall absolute mean biases smaller than 0.7 m s^{-1} and correlation coefficients larger than or equal to 0.9. Moreover, assuming the radar measurements as the reference data set, Mie-cloudy winds are shown to be more precise than Rayleigh-clear winds with an overall random error of 4.14 and 5.81 m s^{-1}, respectively. Similar results were also found from triple collocation analysis, with error standard deviations of 5.61 and 3.50 m s^{-1} for Rayleigh-clear winds and Mie-cloudy winds. In addition, the Mie channel is shown to be more capable of capturing the wind in the planetary boundary layer (< 1500 m). The findings of this study demonstrate the good performance of space-borne Doppler lidar for wind profiling and provide valuable information for data assimilation in numerical weather prediction.

1 Introduction

The lack of wind profiles is still one of the major deficiencies in the Global Observing System (GOS), which limits our knowledge of atmospheric dynamics and the performance of numerical weather prediction (NWP) (World Meteorological Organization, WMO, 2005). To help close this gap, after more than 15 years of design, the Aeolus satellite carrying an Atmospheric Laser Doppler Instrument (ALADIN) was launched by the European Space Agency (ESA) in 2018, becoming the first satellite mission in the world for measuring wind profiles from space. After a successful launch, Aeolus is in a sun-synchronous orbit with a 7 d repeat cycle. It crosses the Equator at 18:00 LT (local time) during ascending orbits (from south to north) and at 06:00 LT during descending orbits (from north to south). The azimuth angle of Aeolus is ∼ 260° for ascending orbits and ∼ 100° for descending orbits, away from the poles. The viewing angle of ALADIN toward the atmosphere is 35° off-nadir. The measured wind along the laser beam line-of-sight (LOS) is then converted to the horizontal to give the horizontal line-of-sight (HLOS) wind component, which is approximately east–west oriented for most of the orbits (Andersson et al., 2008).

Wind retrievals of ALADIN are based on light scattering by atmospheric molecules and particulates (aerosol, cloud droplets, and ice crystals), which move with the ambient wind, and on the Doppler effect (Andersson et al., 2008). The laser system of ALADIN emits a beam of powerful light in the ultraviolet part of the electromagnetic spectrum at 355 nm

Published by Copernicus Publications on behalf of the European Geosciences Union.

towards the Earth. Then, the backscattered light from the atmosphere is collected by the telescope and transferred to the receiver for analysis. Since the laser light can be backscattered by both molecules and particulates in the atmosphere, ALADIN has two separate detection channels. One is for Rayleigh scattering from molecules, such as oxygen and nitrogen, with the diameter being about 0.3–0.4 nm, which is smaller than the light wavelength; the other is for Mie scattering from the large particles such as cloud droplets and ice crystals, dust, and aerosols, the diameters of which are usually greater than 1 µm (Calvert, 1990; Wallace and Hobbs, 2006b; Ingmann and Straume, 2016; Vallejos-Burgos et al., 2018). From the backscattered signal, winds from the surface to about 30 km in height can be derived, depending on the range bin settings, i.e. the size of the 24 bins defining the wind profile.

By detecting global wind profiles from space, the Aeolus satellite has the potential to serve a variety of applications, including further exploring atmospheric dynamics, improving numerical weather predictions, and better estimating the dispersion of air pollutants (Banyard et al., 2021; ESA, 2020a; Rennie et al., 2021). However, before employing Aeolus winds for different applications, it is essential to know the error characteristics of the wind products. In situ measurements (e.g. radiosondes), ground-based remote sensing observations (e.g. lidar or radar), and NWP model equivalents are the three main reference products used for wind validation. After the successful launch, Aeolus winds have been intercompared with different reference data over many regions. For example, Aeolus winds in the early mission stage were compared with radiosonde observations in different climate zones over the Atlantic Ocean and NWP model equivalents for the Northern Hemisphere, and larger biases were reported for both Rayleigh-clear and Mie-cloudy winds (Baars et al., 2020; Martin et al., 2021). This is associated with the early processing algorithms which have since been developed further to account for such issues. Later, Guo et al. (2021) compared the Aeolus winds with radar wind profiler (RWP) measurements over China, showing that the mean differences are -0.64 and $-0.28\,\mathrm{m\,s^{-1}}$ with the standard deviations of 6.82 and $4.2\,\mathrm{m\,s^{-1}}$ for Rayleigh-clear and Mie-cloudy winds, respectively. Validation was also conducted over the polar regions, and a good agreement with ground-based RWP measurements was obtained in most cases (Belova et al., 2021). More recently, Iwai et al. (2021) validated Aeolus 2B02 and 2B10 wind products by comparing with wind profilers, ground-based coherent Doppler wind lidars, and GPS radiosondes over Japan, with the inter-comparison results for wind profilers and radiosondes showing improved quality of Aeolus 2B10 winds as both biases and random errors were smaller compared to those for the 2B02 product. Although validation and calibration have been carried out over many regions, the data quality of Aeolus measurements across Australia has not been investigated so far.

Moreover, regarding the validation method, most works related to Aeolus are based on inter-comparison analysis. In addition to this, triple collocation analysis is another advantageous method to evaluate space-borne remote sensing products. Unlike inter-comparison that treats a reference data set free of errors, triple collocation analysis requires three independent measurement systems and assumes that each system contributes to the truth. The outputs are the error standard deviation of each system and calibration relations based on a reference data set, which can provide valuable information for cost function in data assimilation (Stoffelen, 1998; Vogelzang et al., 2011). Triple collocation analysis has been widely employed to assess the wind measurements from different instruments, including scatterometers, altimeters, and radiometers (Caires and Sterl, 2003; Portabella and Stoffelen, 2009; Ribal and Young, 2020). However, very few studies have evaluated wind products from the space-borne lidar by this method so far. To complement to earlier validation studies, this study evaluates the Aeolus L2B HLOS wind product over Australia by inter-comparison with ground-based wind profiling radar (WPR) measurements. In addition, a triple collocation analysis for Aeolus HLOS winds is conducted with the help of WPR measurements and NWP model equivalents.

A description of the data and methods used in this study is available in Sect. 2. Key research findings from data analysis are presented in Sect. 3, followed by the discussions in Sect. 4. The final section summarizes the study briefly and draws conclusions.

2 Data and methods

2.1 Aeolus L2B wind product

Aeolus Level-2B baseline 11 near-real-time HLOS winds during the Australian summer from October 2020 to March 2021 were used for validation, being the most recent available near-real-time wind product when conducting this study. The data were obtained from the ESA Aeolus Online Dissemination System (https://aeolus-ds.eo.esa.int/oads/access/) (ESA, 2021). According to signal-to-noise ratio, Aeolus L2B winds are categorized into four types, which are Rayleigh-clear, Rayleigh-cloudy, Mie-clear, and Mie-cloudy (de Kloe et al., 2022). The measurements from the Rayleigh channel have better performance in a clear sky (Rayleigh-clear), for which there is little or no contamination from Mie scattering; the wind measurements in the Mie channel need strong backscattering from aerosols, water droplets, or ice crystals (Mie-cloudy) (Rennie et al., 2020). In addition, Rayleigh-clear and Mie-cloudy winds are currently the only two types of Aeolus winds that are assimilated into the ECMWF model for operational weather forecast (Rennie et al., 2021). Based on these considerations, only Rayleigh-clear and Mie-cloudy winds were extracted for evaluation.

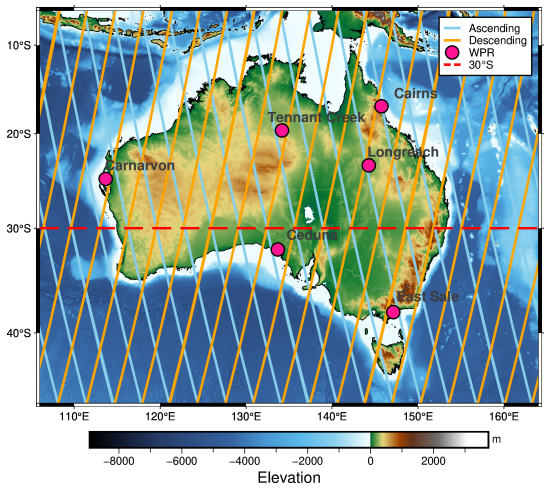

Figure 1. Location of wind profiling radars and Aeolus ground tracks over Australia. The pink marks on the map represent the sites of WPR used in this study, and the blue and orange lines indicate the Aeolus ground tracks for ascending and descending orbits, respectively. The red dashed line at 30° S is the boundary between the tropics and extratropics. Shading with different colours represents the earth relief. The elevation data were accessed and the map was created by the authors using PyGMT (Wessel et al., 2019; Tozer et al., 2019; Uieda et al., 2021).

The horizontal accumulation along the ground track of each observation is typically 87 km for Rayleigh winds (which takes 12 s) and 15 km for Mie winds (which takes around 2 s), but it may be shorter locally due to the classification in cloudy and clear scenes. Vertically, there are 24 range bins with sizes varying from 250 m to 2 km. To capture the characteristics of atmospheric circulation over different climate zones, range bin settings vary along the orbit according to geographic location and in time, as requested by special measurement requests and to adapt to seasons and climate zones. Over Australia, there are two different range bin setting regions (Fig. 1), i.e. the tropical setting region (30° S–30° N) and the extratropical setting region (30–60° S). The differences in range bin settings are measurement heights and range bin thickness. For tropical setting, the measurements can reach just over 20 km in height with a range bin thickness of 750 m between 12 and 15 km to capture the gravity waves, while the maximum measurement height of the extratropical setting is about 17.5 km with a higher vertical resolution of 500 m between 5 and 10 km for jet stream detection (ESA, 2020b).

Referring to the existing recommendations for quality control, the HLOS wind speed with a validity flag of 0 and estimated error larger than 8 m s^{-1} for Rayleigh-clear winds and 4 m s^{-1} for Mie-cloudy winds were removed (Rennie and Isaksen, 2020).

2.2 Wind profiling radar measurements

Wind profiling radar (WPR) is remote sensing equipment that can measure the three-dimensional wind field (Dolman et al., 2018). The Australian WPR network is operated by the Australian Government Bureau of Meteorology, and the data are available from the Centre for Environmental Data Analysis (CEDA) archive (Met Office, 2008). There are two main types of WPR in the Australian network: stratospheric tropospheric profilers (STPs) and boundary layer profilers (BLPs) (Dolman et al., 2018). Both operate at 55 MHz. The maximum detection heights of STPs are 8 km for low mode and 20 km for high mode with a range resolution of 250 and 500 m, respectively. For BLPs, the maximum detection height for low mode is 7 km, and it is 14 km for high mode, with a range resolution of 100 and 250 m, respectively. Both types of WPR measurements have been validated and calibrated with radiosonde data, achieving the slope of the least-squares line of best fit close to 1 for both zonal winds and meridional winds and the random difference between WPR and radiosonde data of about 2 m s^{-1} (Dolman et al., 2016). The wind vectors of WPR measurements from the CEDA archive are 30 min averaged winds.

2.3 NWP model winds

In order to carry out the triple collocation analysis, predicted winds were extracted from the Aeolus Auxiliary Meteorological Data (AUX_MET) files. AUX_MET contains forecasted meteorological information at Aeolus observation locations (e.g. temperature and pressure) that is required for processing the L2B product (de Kloe et al., 2022). These meteorological parameters are generated by the fifth-generation European Centre for Medium-Range Weather Forecasts (ECMWF) Integrated Forecast System (IFS) model. Predicted winds from the AUX_MET files, rather than model winds from analyses, are selected to avoid dependency between model analyses and observed winds during validation, as Aeolus winds used for validation have not yet been assimilated. In addition, although WPR measurements have been assimilated, the dependency of predicted winds with WPR measurements becomes weaker with forecast time. As a result, these three data sets are assumed independent of each other, which is required for triple collocation analyses.

The ECMWF IFS model uses octahedral reduced Gaussian grid $T_{co}1279$ with the grid spacing of about 9 km at mid-latitudes. Vertically, there are 137 model levels. The effective spatial resolution in the free atmosphere of a model is usually 7–10 times the grid distance (Skamarock, 2004), so the effective resolution of the ECMWF IFS model is around 90 km in the free atmosphere. Although the effective spatial resolution may be higher in the planetary boundary layer (PBL) due to

orographic forcing, the upper air where Aeolus mainly operates is generally uninformed. Therefore, in this study, we take about 90 km as the model effective resolution. It is noted that the AUX_MET extracts data from the ECMWF IFS model every 3 s along the Aeolus predicted ground track. With moving speed at around 7 km s^{-1} with respect to the surface, each AUX_MET vertical profile is placed at an interval of about 21 km for a given off-nadir prediction (Michael Rennie, personal communication, 2021), which does not affect the effective resolution of the model. Regarding the data quality, the typical differences between radiosonde and ECMWF winds are 2–3 m s^{-1} (Houchi et al., 2010).

2.4 Collocation criteria

To carry out error analyses, all data should be collocated both in time and in space. First, the nearest Aeolus L2B wind profiles were extracted based on their distance from WPR sites, which should be less than 75 km (Zhang et al., 2016; Guo et al., 2021). This is because many WPR sites in Australia are in coastal regions. The Aeolus ground tracks 100 km or more away from the WPR sites would be either over the ocean or inland. Thus, the wind difference caused by two different representative regions may have much impact on the intercomparison analysis between Aeolus observations and WPR measurements, especially for the Mie-cloudy winds that are usually sampled at a lower level. Additionally, we would like to keep consistency with the existing Aeolus wind validation using radar profiler measurements, to enable comparison results easily. The validation for China from Guo et al. (2021) was the only study available when we carried out this work. Therefore, we chose the WPR sites within 75 km to the Aeolus profiles. The vector winds from WPR measurements with time closest to Aeolus observations were selected. The vector winds from AUX_MET were extracted from the profiles closest to each Aeolus L2B wind profile. Based on this criterion, there are six WPR sites available over Australia, shown in Fig. 1. Over the study period, there should be 5016 Aeolus data samples in total for each detection channel. After quality control based on the criteria in Sect. 2.1, there are 2171 and 394 data samples remaining, accounting for 43.28 % and 7.85 % of the Rayleigh and Mie wind measurements, respectively. The site information and available Aeolus data samples are summarized in Table 1.

Wind vectors from the WPR and AUX_MET data sets were converted to HLOS winds by using the following Eq. (1):

$$\mathrm{HLOS} = -u_{\mathrm{Ref}} \sin A - v_{\mathrm{Ref}} \cos A, \tag{1}$$

where A is the azimuth angle of the Aeolus satellite, and Ref represents either WPR or AUX_MET. The geometry of Aeolus wind measurements is shown in Fig. 2.

Vertically, the HLOS winds from WPR and AUX_MET were converted to winds corresponding to Aeolus range bins by averaging the winds between the top and bottom heights of each vertical bin, shown in Fig. 3.

2.5 Inter-comparison analysis

For inter-comparison analysis, we assumed that WPR is the ground truth. After data filtering and collocation, the mean bias (BIAS), standard deviation of wind difference (SD), scaled median absolute deviation (scaled MAD), and correlation coefficient (R) of both Rayleigh-clear winds and Mie-cloudy winds were quantified based on Eqs. (2), (3), (4), and (5). Scaled MAD is used to represent random error because it is a robust statistic to measure data variability. When random errors are purely Gaussian distributed, scaled MAD is identical to SD; when distributions are not purely Gaussian, scaled MAD is less sensitive to outliers (Ruppert, 2011).

$$\mathrm{BIAS} = \frac{1}{N}\sum_{\mathrm{i}=1}^{N}\left(\mathrm{HLOS}_{\mathrm{Aeolus},i} - \mathrm{HLOS}_{\mathrm{Ref},i}\right) \tag{2}$$

$$\mathrm{SD} = \sqrt{\frac{1}{N-1}\sum_{i=1}^{N}\left(\left(\mathrm{HLOS}_{\mathrm{Aeolus},i} - \mathrm{HLOS}_{\mathrm{Ref},i}\right) - \mathrm{BIAS}\right)^2} \tag{3}$$

$$\begin{aligned}\text{scaled MAD} = 1.4826 \\ \times \text{median}\left(\left|\left(\mathrm{HLOS}_{\mathrm{Aeolus},i} - \mathrm{HLOS}_{\mathrm{Ref},i}\right)\right.\right. \\ \left.\left. -\text{median}\left(\mathrm{HLOS}_{\mathrm{Aeolus},i} - \mathrm{HLOS}_{\mathrm{Ref},i}\right)\right|\right)\end{aligned} \tag{4}$$

$$R = \frac{\left[\begin{array}{c}\sum_{i=1}^{N}\left(\mathrm{HLOS}_{\mathrm{Aeolus},i} - \overline{\mathrm{HLOS}_{\mathrm{Aeolus}}}\right) \\ \left(\mathrm{HLOS}_{\mathrm{Ref},i} - \overline{\mathrm{HLOS}_{\mathrm{Ref}}}\right)\end{array}\right]}{\left[\begin{array}{c}\sqrt{\sum_{i=1}^{N}\left(\mathrm{HLOS}_{\mathrm{Aeolus},i} - \overline{\mathrm{HLOS}_{\mathrm{Aeolus}}}\right)^2} \\ \sqrt{\sum_{i=1}^{N}\left(\mathrm{HLOS}_{\mathrm{Ref},i} - \overline{\mathrm{HLOS}_{\mathrm{Ref}}}\right)^2}\end{array}\right]} \tag{5}$$

Here the subscript Ref represents WPR; N is the total number of data points; i is from 1, 2, 3, …, N.

The confidence limits (uncertainty) for the biases are defined at a 95 % confidence interval. Since the distributions of wind differences are not always Gaussian, the confidence limits were estimated using the bootstrap method when the sample size is greater than 2.

Analyses were performed for all data, but also separated in ascending and descending orbits. In addition, errors as a function of height were also investigated. Since Aeolus observations over Australia have different vertical range bin settings for tropical and extratropical regions, we defined 12 new range bins based on the number of match-up samples in each range bin and the characteristics of the atmospheric circulation. Within the PBL and at a higher height, available match-up samples are limited. So, we defined several new groups at these heights by increasing the spacing. The 500 hPa pressure surface is usually around 5.5 km above sea level, which is important for weather analysis and forecast, so we defined a group between 4.5 and 6 km; the jet stream is usually from 8 to 12 km in height, so two new groups were defined, which are 7.5–10 and 10–12.5 km (Wallace and

Table 1. Information of ground-based WPR sites and Aeolus measurements.

Sites	Latitude	Longitude	Elevation	Aeolus ascending		Aeolus descending	
(type)	(°)	(°)	(m)	Overpass time (UTC)	Available samples (Rayleigh/Mie)	Overpass time (UTC)	Available samples (Rayleigh/Mie)
Longreach (STP)	−23.44	144.28	192	08:41 Thursday	301/57	20:01 Wednesday	320/15
Carnarvon (STP)	−24.89	113.67	4	–	–	22:00 Friday	368/13
Tennant Creek (STP)	−19.64	134.18	376	–	–	20:40 Saturday	151/35
Cairns (BLP)	−16.95	145.75	4	08:31 Wednesday	198/94	20:00 Wednesday	173/49
East Sale (BLP)	−38.12	147.13	5	08:37 Thursday	245/56	19:40 Monday	321/49
Ceduna (BLP)	−32.13	133.70	15	09:32 Monday	94/26	–	–

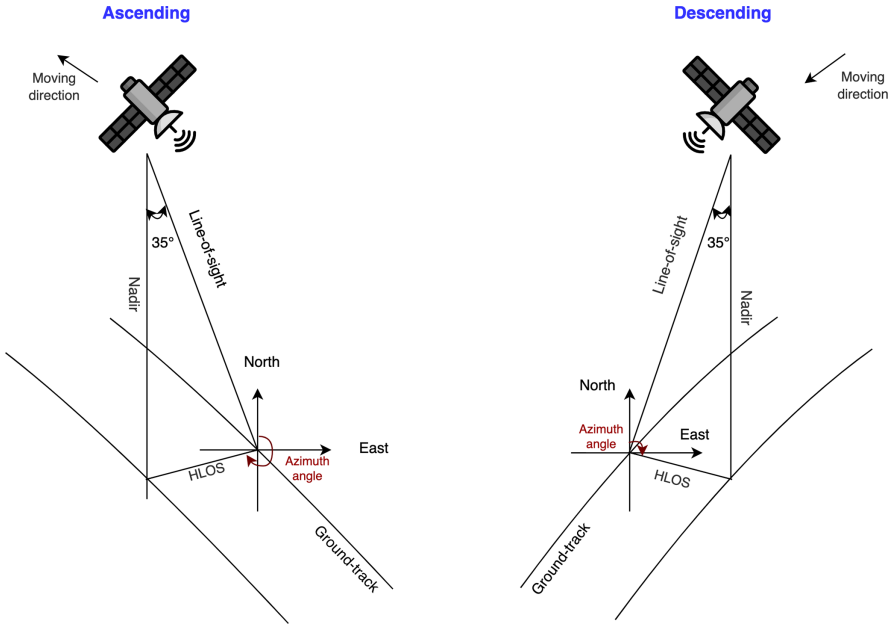

Figure 2. Geometry of Aeolus wind measurements.

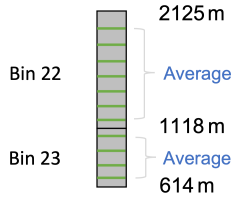

Figure 3. Sketch map of WPR and AUX_MET wind conversion to Aeolus range bins, where green bars represent the heights of WPR or AUX_MET winds.

Hobbs, 2006a). HLOS winds from their original range bins were grouped to defined range bins based on their centre of gravity (COG) heights. Moreover, to investigate the impact of range bin settings on error characteristics, we separated the results for the tropics and extratropics.

2.6 Triple collocation analysis

To carry out triple collocation analysis, two other measurement systems are required besides Aeolus. In this study, they are WPR measurements and ECMWF IFS model equivalents. The temporal and spatial resolutions of these three systems are summarized in Table 2. We choose WPR measurement as the reference, which is system 1. Aeolus L2B winds and NWP winds are systems 2 and 3, respectively. All three systems are linearly correlated with the true HLOS winds,

which can be described by Eqs. (6), (7), and (8).

$$\mathrm{HLOS}_1 = T + e_1 \tag{6}$$

$$\mathrm{HLOS}_2 = a_2 + b_2 T + e_2 \tag{7}$$

$$\mathrm{HLOS}_3 = a_3 + b_3 T + e_3 \tag{8}$$

Here T is the true value of HLOS winds; a_i and b_i are the intercept and the slope of the calibration for each system; e_i is the random error of each system.

The method and equation derivation of triple collocation analysis are formulated in Vogelzang and Stoffelen (2012). To simplify the study, we assume the true measurement errors of each system are independent. Hence, no representation error contributes to the error covariances. Thus, the equations to calculate the error standard deviation of each system can be simplified to Eqs. (9), (10), and (11).

$$\sigma_1 = \sqrt{\langle e_1^2 \rangle} = \sqrt{C_{11} - \frac{C_{12}C_{13}}{C_{23}}} \tag{9}$$

$$\sigma_2 = \sqrt{\langle e_2^2 \rangle} = \sqrt{C_{22} - \frac{C_{12}C_{23}}{C_{13}}} \tag{10}$$

$$\sigma_3 = \sqrt{\langle e_3^2 \rangle} = \sqrt{C_{33} - \frac{C_{23}C_{13}}{C_{12}}} \tag{11}$$

Here C_{ii} is the variance of each system, and C_{ij} is the covariance between systems i and j, and $\langle\rangle$ represents the statistical averaging.

The calibration coefficients can be described by Eqs. (12), (13), (14), and (15), and the calibration relations are shown in Eqs. (16) and (17).

$$b_2 = \frac{C_{23}}{C_{13}} \tag{12}$$

$$b_3 = \frac{C_{23}}{C_{12}} \tag{13}$$

$$a_2 = \langle \mathrm{HLOS}_2 \rangle - b_2 \langle \mathrm{HLOS}_1 \rangle \tag{14}$$

$$a_3 = \langle \mathrm{HLOS}_3 \rangle - b_3 \langle \mathrm{HLOS}_1 \rangle \tag{15}$$

$$\mathrm{HLOS}_2^* = \frac{\mathrm{HLOS}_2}{b_2} - \frac{a_2}{b_2} \tag{16}$$

$$\mathrm{HLOS}_3^* = \frac{\mathrm{HLOS}_3}{b_3} - \frac{a_3}{b_3} \tag{17}$$

Here HLOS_2^* and HLOS_3^* are the calibrated wind speed of system 2 and system 3.

2.7 Wind variability analysis

Wind observations are closely connected to the local atmospheric conditions. To investigate the influence of convection on Aeolus wind measurements, for every Rayleigh or Mie spatial sample, we employed the wind vectors from WPR measurements ±2 h around the collocation points to quantify wind variability in each component and the turbulence kinetic energy (TKE); see Eqs. (18), (19), (20), and (21). The results were averaged for Rayleigh and Mie channels, and the Student t test was performed.

$$\mathrm{Var}(u) = \frac{\sum_{i=1}^{n}(u_i - \overline{u})^2}{n} \tag{18}$$

$$\mathrm{Var}(v) = \frac{\sum_{i=1}^{n}(v_i - \overline{v})^2}{n} \tag{19}$$

$$\mathrm{Var}(w) = \frac{\sum_{i=1}^{n}(w_i - \overline{w})^2}{n} \tag{20}$$

$$\mathrm{TKE} = \frac{\mathrm{Var}(u) + \mathrm{Var}(v) + \mathrm{Var}(w)}{2} \tag{21}$$

Here u_i, v_i, and w_i are WPR east–west, north–south, and vertical winds at each time step (30 min) of ±2 h ($n = 9$) around the collocation points, and $\overline{u}$, $\overline{v}$, and $\overline{w}$ are the corresponding mean winds, respectively.

3 Results

After filtering out the invalid data and collocating all HLOS winds from the three data sets, results were derived from 1011 match-up samples of Rayleigh-clear winds and 224 match-up samples of Mie-cloudy winds.

3.1 Inter-comparison

The results of the inter-comparison analysis with WPR being the ground truth are summarized in Table 3 and presented in Fig. 4. From the scatter plots, it can be seen that the winds detected by the Rayleigh channel range from −40 to 60 m s^{-1}, while the wind speed from the Mie channel is lower, mainly ranging between −20 and 30 m s^{-1}. Overall, both Rayleigh-clear winds and Mie-cloudy winds are in good agreement with WPR measurements with R no less than 0.9 for all data. For Rayleigh-clear winds, the overall bias is −0.48 m s^{-1} with a SD of 6.22 m s^{-1} and a scaled MAD of 5.81 m s^{-1}. A larger bias (−0.71 m s^{-1}) was found during descending orbits, but no significant difference in random errors was detected during ascending and descending orbits. For Mie-cloudy winds, the bias for all data is 0.69 m s^{-1}, and the SD and the scaled MAD are 4.77 and 4.14 m s^{-1}, respectively. Moreover, the Mie channel has better performance on descending orbits (bias: −0.24 m s^{-1}; scaled MAD: 3.63 m s^{-1}) than ascending orbits (bias: 1.35 m s^{-1}; scaled MAD: 4.11 m s^{-1}).

The wind difference as a function of height for all data (a) and ascending (b) and descending (c) orbits is presented in Fig. 5. Overall, there are more valid paired samples from the Rayleigh channel, except for heights below 750 m. Most of the Rayleigh-WPR samples distribute between 1500 and 20 000 m, while Mie-WPR samples mainly distribute below 10 000 m. Regarding the bias at each height, the Aeolus Rayleigh channel shows negative biases of about −1.7 m s^{-1} between 750 and 7500 m for ascending orbits

Table 2. Spatial and temporal resolution of the three data sets.

	1: WPR	2: Aeolus L2B	3: AUX_MET
Horizontal	Point-based	87 km (Rayleigh)/10–15 km (Mie)	∼ 90 km
Vertical	100/250/500 m	From 250 to 2 km	137 model levels
Temporal	30 min	∼ 10 s/∼ 1–2 s	Instantaneous

Table 3. Results of inter-comparison with ground-based WPR measurements.

	Orbit	Bias ($m\,s^{-1}$)	SD ($m\,s^{-1}$)	Scaled MAD ($m\,s^{-1}$)	R	N
Rayleigh-clear	All	−0.48 [−0.86, −0.09]	6.22	5.81	0.92	1011
	Ascending	−0.06 [−0.73, 0.61]	6.59	5.76	0.89	368
	Descending	−0.71 [−1.18, −0.26]	5.99	5.73	0.88	643
Mie-cloudy	All	0.69 [0.08, 1.33]	4.77	4.14	0.90	224
	Ascending	1.35 [0.57, 2.19]	4.76	4.11	0.86	132
	Descending	−0.24 [−1.23, 0.67]	4.64	3.63	0.90	92

and about $-0.8\,m\,s^{-1}$ between 1500 and 10 000 m for descending orbits, with the scaled MADs fluctuating at around $5\,m\,s^{-1}$. Above 10 000 m, for most heights, biases and scaled MADs become larger and/or more variable for Rayleigh wind match-ups. For the Mie channel, positive biases were detected between 750 and 10 000 m with about $1.8\,m\,s^{-1}$ for ascending orbits and about $0.6\,m\,s^{-1}$ for descending orbits except for the height of 6000–7500 m, and the scaled MADs are almost within $5\,m\,s^{-1}$. Negative biases and smaller scaled MADs were found below 750 m and above 10 000 m for both ascending and descending orbits for the Mie channel.

To investigate the error characteristics for regions with different range bin settings, we separated the results from two regions, shown in Fig. 6. For the tropics, larger biases from Rayleigh-clear winds and Mie-cloudy winds were found for the lower range bins with a thickness of 500 m. The random errors of Rayleigh-clear winds fluctuated at around $5\,m\,s^{-1}$ over the range bins of 1 km thickness, and the larger random errors were detected in range bins with a smaller thickness of 500 or 750 m. For Mie-cloudy winds, the random errors for all range bins are lower than $5\,m\,s^{-1}$. For the sites over the extratropics, negative (positive) biases were found over most range bins for Rayleigh-clear (Mie-cloudy) winds. Random errors of Rayleigh-clear winds become smaller with height increasing, except for the range bin of 500 m thickness from higher heights, while the opposite is true for Mie-cloudy winds. The uncertainties of biases increase with height due to the limited number of match-up samples. Overall, based on Fig. 6, smaller range bin thickness may contribute to larger random errors, especially for Rayleigh-clear winds.

3.2 Triple collocation

The result of the triple collocation analysis is shown in Table 4. For the combination of Rayleigh-clear winds, WPR, and NWP model equivalents, the Aeolus measurements have the largest error standard deviation of $5.61\,m\,s^{-1}$ followed by WPR observations of $2.01\,m\,s^{-1}$. NWP model equivalent is most precise, with an error standard deviation of $1.17\,m\,s^{-1}$. Similar results were also obtained from the combination with Mie-cloudy winds, and the error standard deviations are 3.50, 2.60, and $1.70\,m\,s^{-1}$ for Aeolus measurements, WPR observations, and NWP model equivalents, respectively.

The calibration coefficients and relations for Aeolus L2B and NWP winds are shown in Table 5. For Rayleigh wind comparison, the Aeolus and the NWP model have similar patterns in wind estimation with intercepts of −0.404 and $-0.236\,m\,s^{-1}$ and slopes of 1.044 and 1.033, respectively. Regarding the Mie wind comparison, the intercepts are 0.388 and $0.064\,m\,s^{-1}$ with the slopes of 1.106 and 1.075 for the Aeolus and the NWP model winds, respectively.

3.3 Wind variability

According to Table 6, all metrics of WPR wind variability for Mie-cloudy winds are higher than that of Rayleigh-clear winds, but only the difference in w wind component is statistically significant (p value < 0.001). For Rayleigh wind detection, there is no big difference in wind variability during ascending and descending orbits, except for the w component. For Mie wind detection, wind variability (v, w, and TKE) during ascending orbits is significantly higher than that during descending orbits, implying more convection in the late afternoon. Overall, the result suggests that the atmosphere may have larger variability during Mie-cloudy wind sampling, especially for ascending orbits.

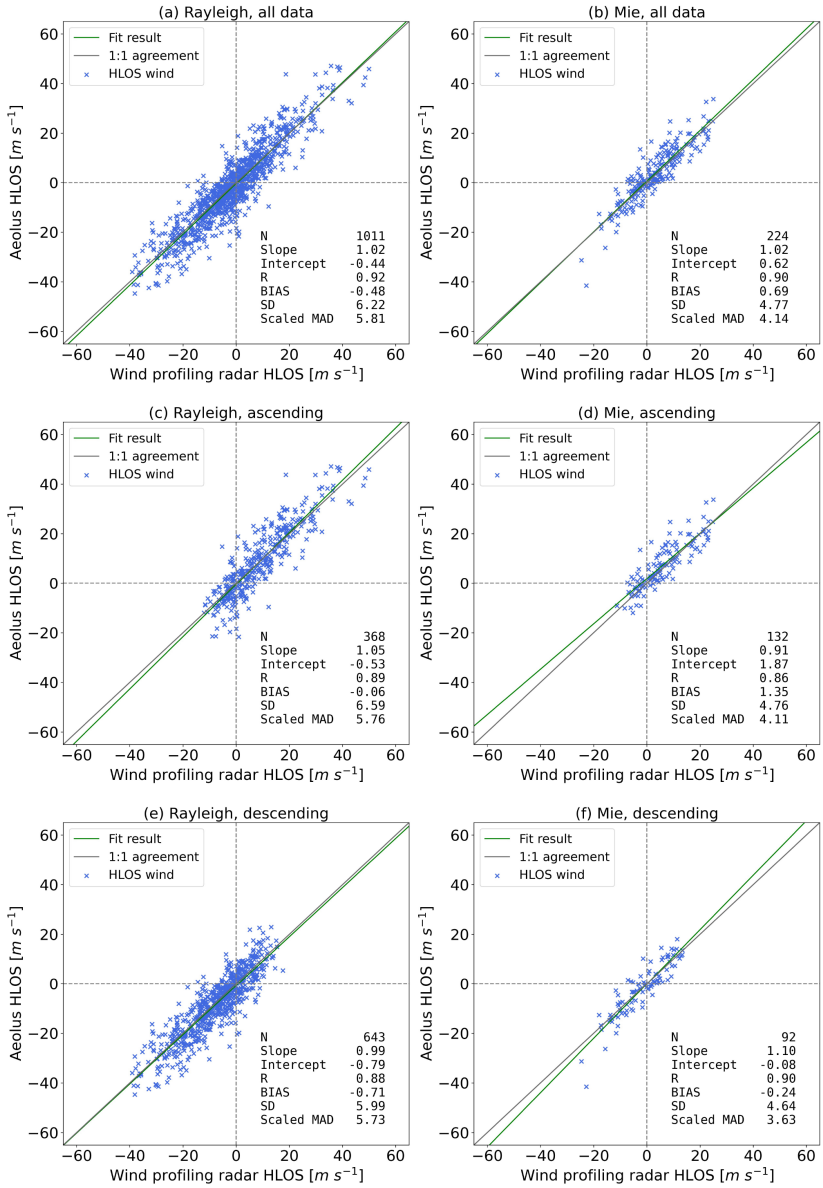

Figure 4. Scatter plots of Aeolus HLOS winds against WPR HLOS winds for all data, ascending orbits, and descending orbits. Panels **(a)**, **(c)**, and **(e)** are for the Rayleigh-clear winds, and **(b)**, **(d)**, and **(f)** are for the Mie-cloudy winds. Green and grey lines indicate the fitted regression result and 1 : 1 agreement, respectively.

4 Discussion

The findings from the inter-comparison analysis indicate that both Rayleigh-clear and Mie-cloudy winds are in good agreement with the ground-based radar measurements with the biases for all data meeting the mission requirement of $0.7\,\mathrm{m\,s^{-1}}$ (Ingmann and Straume, 2016). However, the random errors represented by scaled MADs from both channels are larger than the specified random error of $< 3\,\mathrm{m\,s^{-1}}$ below 20 km (Ingmann and Straume, 2016), especially from

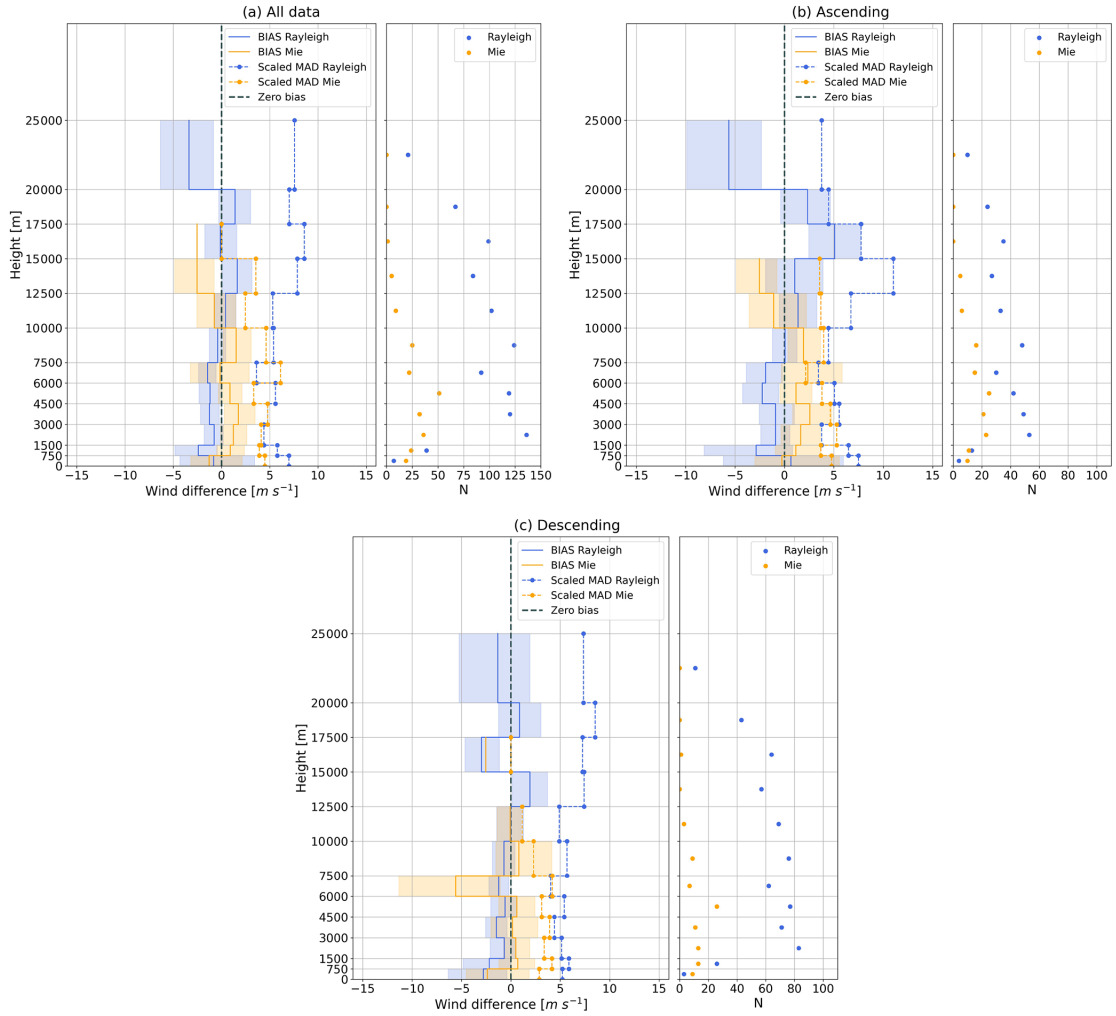

Figure 5. Wind differences (Aeolus-WPR) with height for **(a)** all data, **(b)** ascending orbits, and **(c)** descending orbits. Left: bias and scaled MAD of wind differences as a function of height, with shading areas representing the uncertainty. Right: the number of available match-ups at each height. Blue and orange colours indicate the results for the Rayleigh and Mie channels, respectively.

Table 4. Error standard deviation of three different systems.

	1: WPR ($m\,s^{-1}$)	2: Aeolus L2B ($m\,s^{-1}$)	3: AUX_MET ($m\,s^{-1}$)	N
Rayleigh-clear	2.01	5.61	1.17	1011
Mie-cloudy	2.60	3.50	1.70	224

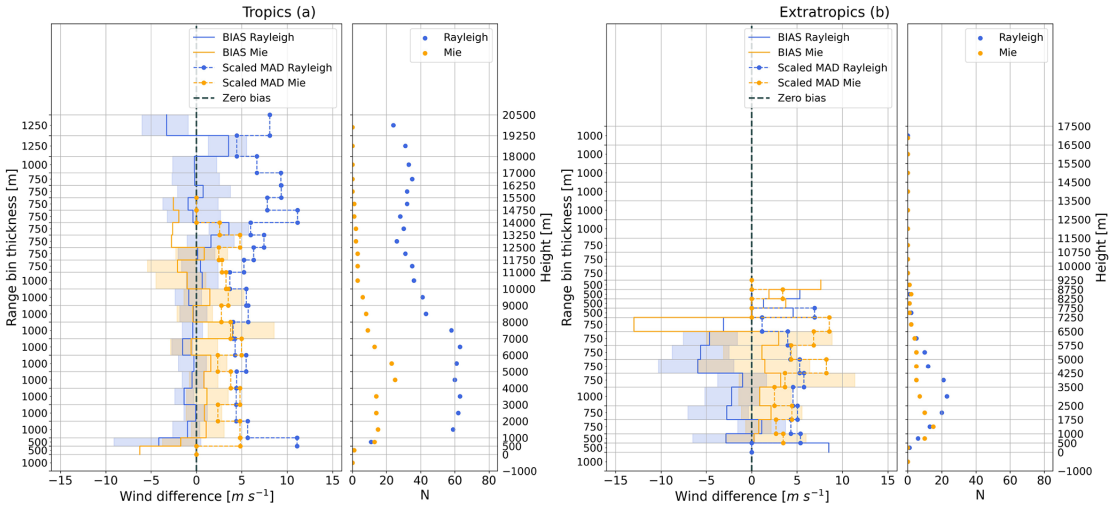

Figure 6. Wind differences (Aeolus-WPR) with range bins for the **(a)** tropics and **(b)** extratropics. Left: distributions of bias and scaled MAD of wind differences over different range bins, with shading areas representing the uncertainty. Right: the number of available match-ups at each range bin. Blue and orange colours indicate the results for the Rayleigh and Mie channels, respectively. Note: the heights on the y axis are just for reference, which are not exactly same with the actual heights of each vertical range bin.

Table 5. Calibration coefficients of Aeolus L2B and NWP winds.

	2: Aeolus L2B			3: AUX_MET		
	a2	b2	$HLOS_2^*$	a3	b3	$HLOS_3^*$
Rayleigh-clear	−0.404	1.044	$0.958HLOS2 + 0.387$	−0.236	1.033	$0.968HLOS3 + 0.228$
Mie-cloudy	0.388	1.106	$0.904HLOS2 - 0.351$	0.064	1.075	$0.930HLOS3 - 0.060$

the Rayleigh detection channel. These results are in line with many existing studies over different regions (Baars et al., 2020; Guo et al., 2021; Iwai et al., 2021; Chen et al., 2021). The large random errors are mainly because of unwanted signal losses in the instrument transmission and detection chain since the Aeolus launch (Krisch and the Aeolus DISC, 2020), which impact the wind quality, especially for the Rayleigh channel. Regarding the performance during different orbit phases, a larger absolute mean bias was found for Rayleigh-clear winds during descending orbits, which is consistent with the results for the Northern Hemisphere (Martin et al., 2021), but the magnitudes of the biases ($< 1\ m\ s^{-1}$) are smaller in this study. No big difference in random errors was found from Rayleigh-clear winds. For Mie-cloudy winds, a large mean bias ($1.35\ m\ s^{-1}$) and random error ($4.11\ m\ s^{-1}$) were identified during ascending orbits. One possible reason would be different representativeness conditions in the morning (descending) and afternoon (ascending). Figure 4d and f show different wind distributions during ascending and descending orbits, hence suggesting a different circulation in the morning (descending) and afternoon (ascending). Moreover, Fig. 5 shows clouds peak at about 5 km height during descending orbits (at about 06:00 LT), while during ascending orbits, there are more uniform clouds from 2 to 8 km height at the end of the day (at about 18:00 LT). In addition, Table 6 shows higher wind variability for ascending orbits during Mie-cloudy wind sampling, implying more convection in the late afternoon. So, the meteorological conditions during Mie wind measurements for the ascending and descending orbit phases appear quite different, which may imply different representativeness conditions and hence different random errors.

The vertical distributions of wind differences indicate that Mie-cloudy winds are more precise compared to Rayleigh-clear winds below 1500 m for all data, which is consistent with the studies for China and Japan (Iwai et al., 2021; Wu et al., 2022). Higher random errors for Rayleigh-clear winds can partly be attributed to the smaller range bin thickness in the PBL. Below 750 m, large biases for both Rayleigh-clear and Mie-cloudy winds were found during descending orbits. This low accuracy may be related to the inhomogeneous topography at Cairns and at East Sale, which may have

Table 6. Results of wind variability based on WPR measurements.

	Var (u)	Var (v)	Var (w)	TKE
Rayleigh-clear ($m^2\,s^{-2}$)	2.24	2.09	0.01	2.15
Mie-cloudy ($m^2\,s^{-2}$)	2.48	2.45	0.03	2.48
p value	0.358	0.181	< 0.001	0.110
Rayleigh-clear ascending ($m^2\,s^{-2}$)	2.08	1.80	0.02	1.94
Rayleigh-clear descending ($m^2\,s^{-2}$)	2.34	2.25	0.01	2.26
p value	0.298	0.070	< 0.001	0.097
Mie-cloudy ascending ($m^2\,s^{-2}$)	2.78	2.95	0.03	2.89
Mie-cloudy descending ($m^2\,s^{-2}$)	2.06	1.76	0.02	1.92
p value	0.143	0.029	0.002	0.033

a larger impact on descending wind measurements, shown in Fig. 1. The large bias of Mie-cloudy winds between 6500 and 7250 m in the extratropical region mainly comes from the East Sale site during descending orbit on 30 November 2020. The WPR data quality on that day is not good, with missing data on many range bins. To collocate with Aeolus wind at the COG height of 6907 m (6530–7285 m), WPR winds should be converted by averaging the winds at the height of 6755, 7005, and 7255 m, but only wind at 6755 m is available. After conversion, the $HLOS_{WPR}$ ($-22.76\,m\,s^{-1}$) is much lower than the Aeolus measurements ($-41.5\,m\,s^{-1}$). Moreover, the higher accuracies of Mie-cloudy winds during both ascending and descending orbits below 1500 m suggest that the Mie channel is more capable of capturing winds within the PBL. This may also suggest the potential large impact of Mie-cloudy winds on data assimilation at these heights. In addition, during the descending orbit phase, for the Mie channel, the biases between 750 and 6000 m are smaller than $0.7\,m\,s^{-1}$, achieving the mission requirement.

The vertical distributions of available match-ups show most Rayleigh-WPR match-ups between 1500 and 20 000 m, since below 1500 m less Rayleigh-clear winds are available due to the attenuation of the molecular signal because of Mie scattering within the PBL. Above 1500 m, the number of available match-ups decreases with height. This is because the maximum measurement height of BLP is 7 km (10 km) and of STP is 8 km (20 km) for the low mode (high mode), so fewer data samples are available at higher heights. The majority of match-ups for Mie-cloudy winds distribute below 10 000 m, which is consistent with where Mie-scattering is expected to take place. Moreover, the number of Mie-WPR match-ups peaks between 4500 and 6000 m during the descending orbits (about 06:00 LT) due to the mid-level clouds, such as altocumulus clouds that are mostly observed in warm spring and summer mornings (Gao et al., 2019).

The error standard deviations or random errors estimated by the triple collocation analysis for Rayleigh-clear winds ($5.61\,m\,s^{-1}$) and Mie-cloudy winds ($3.50\,m\,s^{-1}$) are roughly comparable with the results from inter-comparison analysis ($5.81\,m\,s^{-1}$ for Rayleigh-clear winds and $4.14\,m\,s^{-1}$ for Mie-cloudy winds), indicating the Mie-cloudy winds are more precise than Rayleigh-clear winds. For the WPR, the temporal and spatial representation errors associated with the collocation criteria and the aggregated Aeolus observations are the main contribution to the random errors. The NWP random errors obtained are in line with expectations. Taking the spatial representation error into account, Skamarock (2004) argues that the effective spatial resolution of a model in the free atmosphere is 7–10 times the grid distance; thus the horizontal resolution of Aeolus measurements for Rayleigh-clear winds and NWP model equivalents are almost alike, with the WPR-resolving small-scale variance not detected by the Aeolus or the NWP model. Given the coarse NWP resolution, the common variance of the coarse Rayleigh-clear winds and WPR will be small, and hence the impact of representativeness error on the Rayleigh comparison is limited. For the Mie comparison, the remaining common variance between the moderate-resolution Mie-cloudy winds and WPR is not resolved by the NWP model, which is coarsest, leading to the higher error standard deviation of NWP. Assuming a spatial representativeness error for NWP of $1\,m\,s^{-1}$ (Stoffelen et al., 2020), then the error standard deviations with respect to NWP become 1.37, 2.79, and $3.64\,m\,s^{-1}$ for NWP, WPR, and Mie-cloudy winds, respectively. Compared with the results of triple collocation for Rayleigh winds, the random errors for NWP and WPR are higher. The study from Lin et al. (2016) explicitly showed that model wind accuracy near the ocean surface over convective areas is 4 times larger than that of clear areas. Moreover, based on the wind variability results in Sect. 3.3, these higher values may be related to the vertical wind shear and convective conditions during Mie wind sampling. Additionally, the number of collocated samples for Mie comparison is just 224, which is much lower than the optimal number (at least 1000 samples) for triple collocation analysis; thus the results contain some uncertainty. When performing interpretation with respect to the system with the intermediate spatial resolution, that is the Mie scale, the spatial represen-

tation error represents part of the common resolved signal in WPR and Mie-cloudy winds, but the NWP model does not resolve this part of the signal. Thus, the error standard deviations with respect to the Mie scale become 1.97, 2.40, and 3.35 $m\,s^{-1}$ for NWP, WPR, and Mie-cloudy winds, respectively, where the NWP winds still appear as the most precise.

This study is based on the Aeolus near-real-time 2B11 data. It is known that Mie-cloudy winds show systematic biases, for which a solution has been in place for operational processing since July 2021 (Marseille et al., 2022). The needed correction for non-linearities of the Mie spectral response performs better when derived from an NWP-based method than from in-orbit instrument calibration (Marseille et al., 2022). The L2B processing was adjusted accordingly. As a result, systematic biases for moderate winds were removed, and overestimation of strong winds was reduced. In order to evaluate whether these systematic errors impact the current validation results, we applied the correction method to the near-real-time 2B11 data during October 2020–March 2021 to yield corrected Mie winds. The method of correction and validation results are shown in Appendix A. The analysis based on corrected Mie-cloudy winds suggests that the non-linearity bias correction has a potential to reduce the biases and random errors, especially for the samples from low- to mid-level heights. These results do not affect above discussion.

In addition, at the beginning of this study, we also tried the threshold values of 7 $m\,s^{-1}$ for Rayleigh-clear and 5 $m\,s^{-1}$ for Mie-cloudy winds for quality control referenced from the study from Guo et al. (2021). The main results for inter-comparison analysis and triple collocation are summarized in Appendix B. We found that the threshold values obviously impact the number of available data points. When we increase (decrease) the threshold value for Mie-cloudy (Rayleigh-clear) winds, more (fewer) data points become available. Regarding the statistics, the threshold values do not have much impact on the determined systematic and random errors for Rayleigh-clear winds that have around 1000 data points in total. For Mie-cloudy winds, the systematic and random errors are more sensitive to the threshold value partly because of fewer data points.

5 Conclusions

With the successful launch and operation of the Aeolus satellite, this study was undertaken evaluating the Level-2B baseline 11 HLOS wind product during the Australian summer from October 2020 to March 2021. To achieve this, the Aeolus Rayleigh-clear and Mie-cloudy winds were inter-compared with ground-based WPR measurements. In addition, the triple collocation analysis was attempted for the combination of Aeolus winds (Rayleigh-clear and Mie-cloudy), WPR measurements, and NWP model equivalents.

When comparing with the ground-based radar measurements, no obvious biases (absolute mean bias $< 0.7\,m\,s^{-1}$) and good agreements ($R \geq 0.9$) were found for both Rayleigh-clear and Mie-cloudy winds for all match-up samples, but the bias for Mie-cloudy winds has a larger uncertainty. Moreover, the error characteristics are different between ascending and descending orbits. For the Rayleigh channel, the wind detection during ascending orbits has higher accuracy but larger uncertainty than during descending orbits, while for the Mie channel, larger bias and random error were detected during ascending orbits. Vertically, the Mie channel was found to be more capable of detecting winds within the PBL, suggesting a larger impact of Mie winds in data assimilation at these heights. In addition, both difference statistics and triple collocation analysis showed that Mie-cloudy winds are more precise than Rayleigh-clear winds. Moreover, triple collocation analysis showed that the NWP winds are most precise in representing Aeolus measurement scales, followed by WPR measurements, and Aeolus observations have the largest errors for both Rayleigh and Mie comparisons. Overall, the evidence from this study demonstrates that the space-borne lidar is able to detect winds with sufficient accuracy, which implies the potential benefit of Aeolus winds for data assimilation in numerical weather prediction, feeding different applications such as aeroplane route optimization or wind energy prediction.

Appendix A

The Mie-cloudy winds from 2B11 were corrected following Marseille et al. (2022). The corrected Mie-cloudy winds were sampled along the same profiles and range bins as the original 2B11 data and were extracted for further validation. The employed method is the same as for the original 2B11 Mie-cloudy winds.

After filtering out the outliers, there are 227 match-ups for analysis. Overall, the results from inter-comparison analysis are almost the same as the original Mie-cloudy winds, with bias and scaled MAD becoming slightly smaller for all data (Table A1 and Fig. A1). However, for ascending orbits, the scaled MAD increased by 0.28 $m\,s^{-1}$. This may be caused by the low data quality over complex terrain at East Sale and Cairns. For descending orbits, both bias and scaled MAD increased somewhat, but not obviously.

Regarding the wind difference as a function of height (Fig. A2), some improvements in accuracy and precision can be found mainly below 10 000 m. In particular, for data from all orbits, the random error below 3000 m reduced by at least 0.6 $m\,s^{-1}$; the biases between 1500 and 6000 m during descending orbits are close to 0. The reduction in random error can also be seen below 4000 m and between 6000 and 8000 m in the tropics; the reduction in both biases and random errors can be found from 1750 to 3500 m and from 4250 to 5000 m

in the extratropics (Fig. A3). These are in line with the fact that most of the corrected Mie winds are from the moderate wind speed range.

The results from triple collocation analysis (Table A2) indicate that the correction can reduce the random error of Mie-cloudy winds to some extent, but there is some uncertainty due to the limited number of collocated samples. The calibration coefficients (Table A3) are almost comparable with the results based on original 2B11 winds.

The results based on corrected Mie-cloudy winds suggest that the non-linearity bias correction has a potential to reduce the bias and random errors, especially for the low- to mid-level heights, which needs to be further demonstrated by enlarging the data samples or extending the study period.

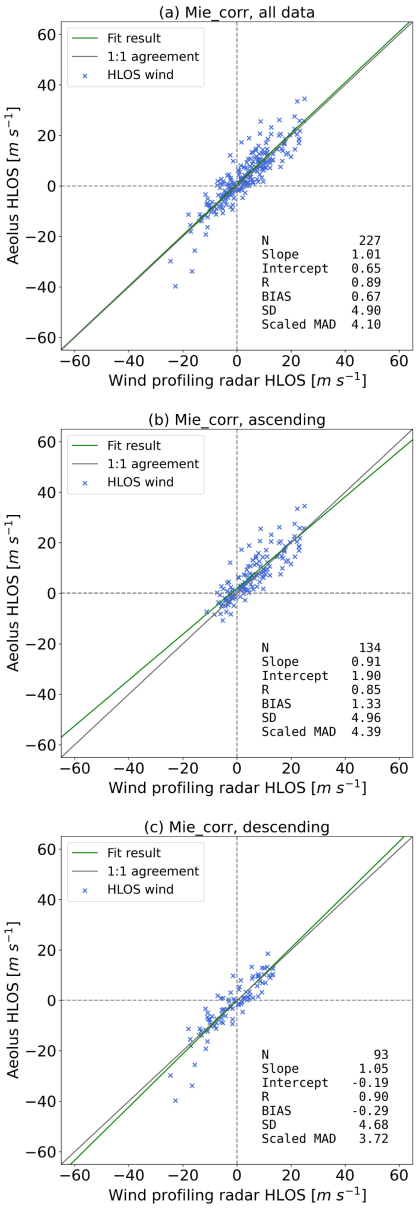

Figure A1. Scatter plots of corrected Mie-cloudy winds against WPR HLOS winds for all data **(a)**, ascending orbits **(b)**, and descending orbits **(c)**. Green and grey lines indicate the fitted regression result and 1 : 1 agreement, respectively.

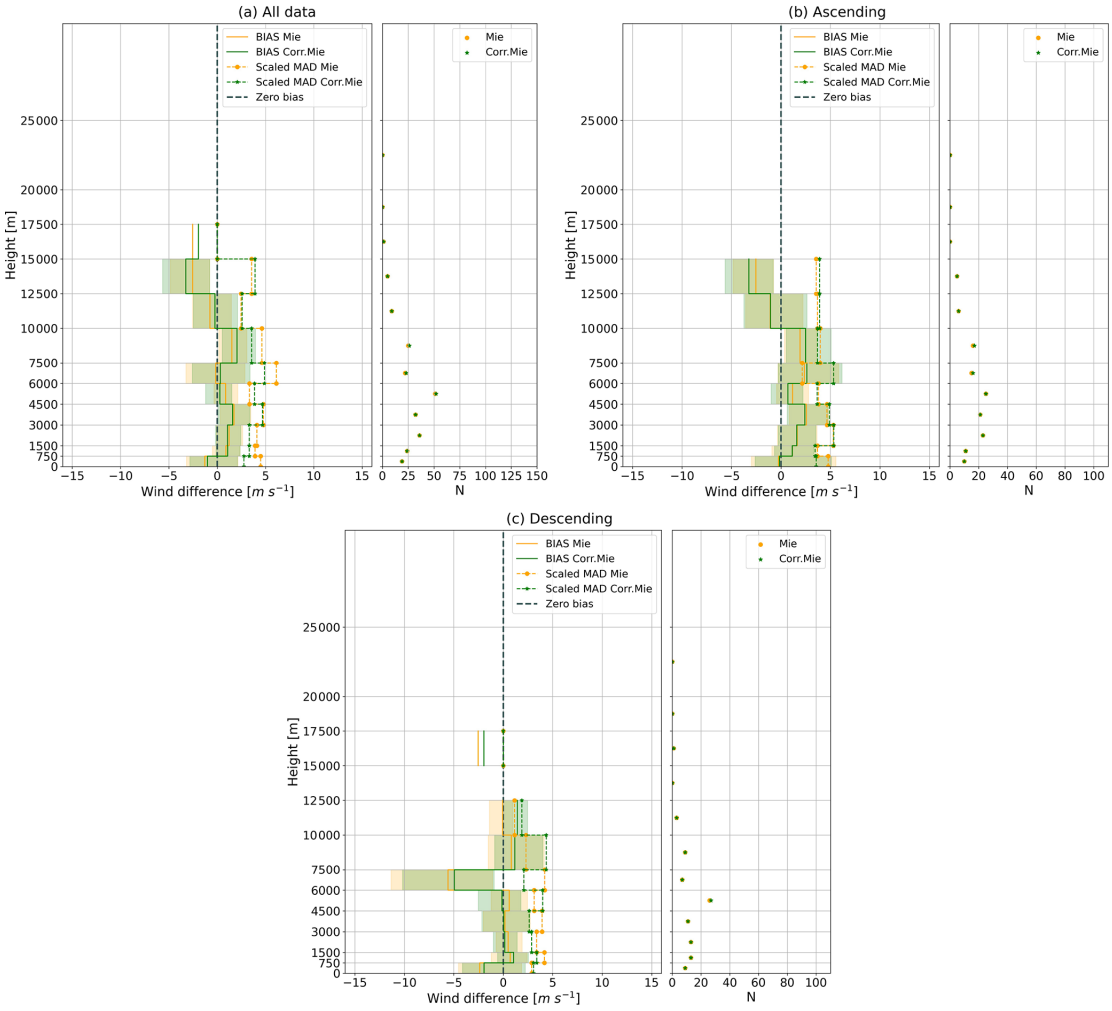

Figure A2. Wind differences (Aeolus-WPR) with height for **(a)** all data, **(b)** ascending orbits, and **(c)** descending orbits. Left: bias and scaled MAD of wind differences as a function of height, with shaded areas representing the uncertainty. Right: the number of available match-ups at each height. Orange and green colours indicate the results for Mie-cloudy and corrected Mie-cloudy winds, respectively.

Table A1. Results of inter-comparison with ground-based WPR measurements for corrected Mie-cloudy winds.

	Orbit	Bias ($m\,s^{-1}$)	SD ($m\,s^{-1}$)	Scaled MAD ($m\,s^{-1}$)	R	N
Corrected Mie-cloudy	All	0.67 [0.03, 1.31]	4.90	4.10	0.89	227
	Ascending	1.33 [0.52, 2.20]	4.96	4.39	0.85	134
	Descending	−0.29 [−1.28, 0.61]	4.68	3.72	0.90	93

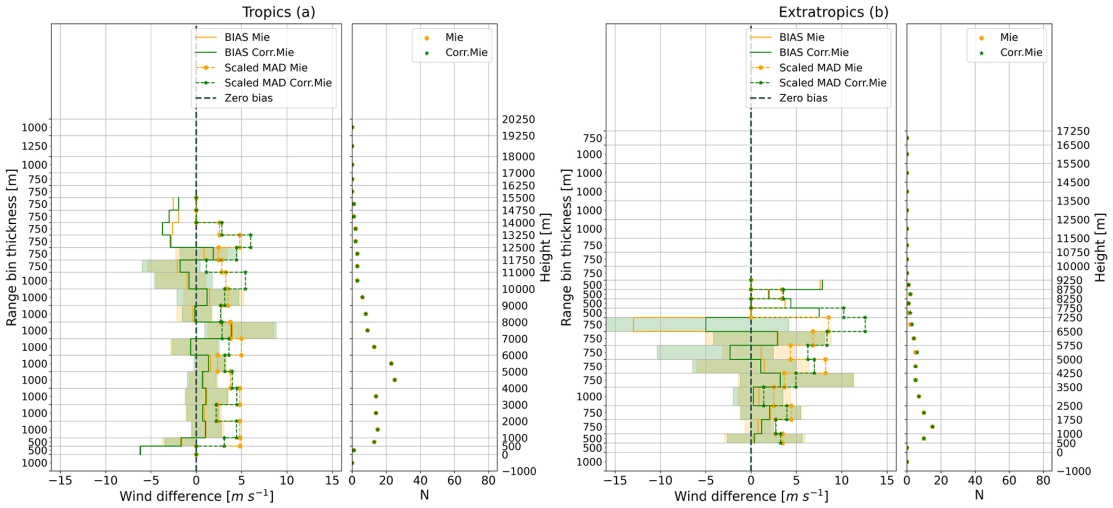

Figure A3. Wind differences (Aeolus-WPR) with range bins for the **(a)** tropics and **(b)** extratropics. Left: distributions of bias and scaled MAD of wind differences over different range bins, with shaded areas representing the uncertainty. Right: the number of available match-ups at each range bin. Orange and green colours indicate the results for Mie-cloudy and corrected Mie-cloudy winds, respectively. Note: the heights on the y axis are just for reference, which are not exactly the same as the actual heights of each vertical range bin.

Table A2. Error standard deviation of three different systems.

	1: WPR ($\mathrm{m\,s^{-1}}$)	2: Aeolus L2B ($\mathrm{m\,s^{-1}}$)	3: AUX_MET ($\mathrm{m\,s^{-1}}$)	N
Corrected Mie-cloudy	3.00	3.34	1.63	227

Table A3. Calibration coefficients of Aeolus L2B and NWP winds.

	2: Aeolus L2B			3: AUX_MET		
	a2	b2	HLOS_2^*	a3	b3	HLOS_3^*
Corrected Mie-cloudy	0.337	1.115	$0.897\mathrm{HLOS2}-0.302$	-0.031	1.129	$0.886\mathrm{HLOS3}+0.027$

Appendix B

Regarding quality control, error estimate threshold values of $7\,m\,s^{-1}$ for Rayleigh-clear and $5\,m\,s^{-1}$ for Mie-cloudy winds were applied at the beginning of this study. The main results of inter-comparison and triple collocation analysis are summarized in Tables B1 and B2.

Table B1. Results of inter-comparison with ground-based WPR measurements based on the error estimate threshold values of $7\,m\,s^{-1}$ for Rayleigh-clear and $5\,m\,s^{-1}$ for Mie-cloudy winds.

	Orbit	Bias ($m\,s^{-1}$)	SD ($m\,s^{-1}$)	Scaled MAD ($m\,s^{-1}$)	R	N
Rayleigh-clear	All	−0.51 [−0.89, −0.13]	6.10	5.80	0.92	998
	Ascending	−0.17 [−0.81, 0.48]	6.27	5.62	0.89	360
	Descending	−0.70 [−1.17, −0.23]	6.00	5.76	0.88	638
Mie-cloudy	All	0.72 [0.06, 1.38]	5.13	4.19	0.89	231
	Ascending	1.54 [0.69, 2.42]	5.13	4.16	0.85	136
	Descending	−0.46 [−1.49, 0.49]	4.91	3.63	0.89	95

Table B2. Error standard deviation of three different systems based on the error estimate threshold values of $7\,m\,s^{-1}$ for Rayleigh-clear and $5\,m\,s^{-1}$ for Mie-cloudy winds.

	1: WPR ($m\,s^{-1}$)	2: Aeolus L2B ($m\,s^{-1}$)	3: AUX_MET ($m\,s^{-1}$)	N
Rayleigh-clear	2.01	5.51	1.17	998
Mie-cloudy	2.49	3.96	1.86	231

Code and data availability. The Aeolus Level-2B11 wind product is available at the ESA Aeolus Online Dissemination System (https://aeolus-ds.eo.esa.int/oads/access/, last access: 5 January 2022, ESA, 2021). The wind profiling radar measurements can be obtained from the CEDA Archive (https://catalogue.ceda.ac.uk/uuid/9e22544a66ba7aa902ae431b1ed609d6, last access: 18 December 2021, Met Office, 2008). Aeolus AUX_MET files were created by the ECMWF and obtained from the workstation at the Royal Netherlands Meteorological Institute (KNMI) upon reasonable request. Earth relief data are from Tozer et al. (2019) and were accessed through PyGMT (https://doi.org/10.5281/zenodo.5607255, Uieda et al., 2021; Wessel et al., 2019).

Author contributions. All authors have made a contribution to the paper preparation. JdK assisted in AUX_MET data preparation. GJM conducted the Mie wind correction. HZ performed the data analysis and drafted the manuscript. AS, GJM, CBH, and IK discussed the validation methods and helped interpret the research findings. HZ revised the manuscript critically with help from all co-authors.

Competing interests. Some authors are members of the editorial board of the journal *Atmospheric Measurement Techniques*. The peer-review process was guided by an independent editor, and the authors also have no other competing interests to declare.

Disclaimer. Publisher's note: Copernicus Publications remains neutral with regard to jurisdictional claims in published maps and institutional affiliations.

Special issue statement. This article is part of the special issue "Aeolus data and their application (AMT/ACP/WCD inter-journal SI)". It is not associated with a conference.

Acknowledgements. This study is a part of the PhD project Aeolus Satellite Lidar for Wind Mapping that is a sub-project of the Innovation Training Network Marie Skłodowska-Curie Actions: Lidar Knowledge Europe (LIKE) supported by the European Union Horizon 2020 (grant number: 858358). The authors thank the ESA Aeolus Online Dissemination System (https://aeolus-ds.eo.esa.int/oads/access/) for access to Aeolus Level-2B baseline 11 near-real-

time HLOS winds. We also acknowledge the Australian Government Bureau of Meteorology for operating the WPR network over Australia and the CEDA for archiving and providing the WPR measurements. The authors are very thankful to KNMI for access to the AUX_MET data files and for being the secondment host institution. Our appreciation also goes to Michael Rennie for the information of NWP model equivalents.

Financial support. This research has been supported by the Horizon 2020 (LIKE (grant no. 858358)).

Review statement. This paper was edited by Oliver Reitebuch and reviewed by two anonymous referees.

References

Andersson, E., Dabas, A., Endemann, M., Ingmann, P., Källén, E., Offiler, D., and Stoffelen, A.: ADM-Aeolus Science Report, SP-1311, ESA, 121 pp., https://esamultimedia.esa.int/multimedia/publications/SP-1311/SP-1311.pdf (last access: 2 May 2022), 2008.

Baars, H., Herzog, A., Heese, B., Ohneiser, K., Hanbuch, K., Hofer, J., Yin, Z., Engelmann, R., and Wandinger, U.: Validation of Aeolus wind products above the Atlantic Ocean, Atmos. Meas. Tech., 13, 6007–6024, https://doi.org/10.5194/amt-13-6007-2020, 2020.

Banyard, T. P., Wright, C. J., Hindley, N. P., Halloran, G., Krisch, I., Kaifler, B., and Hoffmann, L.: Atmospheric Gravity Waves in Aeolus Wind Lidar Observations, Geophys. Res. Lett., 48, e2021GL092756, https://doi.org/10.1029/2021GL092756, 2021.

Belova, E., Kirkwood, S., Voelger, P., Chatterjee, S., Satheesan, K., Hagelin, S., Lindskog, M., and Körnich, H.: Validation of Aeolus winds using ground-based radars in Antarctica and in northern Sweden, Atmos. Meas. Tech., 14, 5415–5428, https://doi.org/10.5194/amt-14-5415-2021, 2021.

Caires, S. and Sterl, A.: Validation of ocean wind and wave data using triple collocation, J. Geophys. Res., 108, 3098, https://doi.org/10.1029/2002JC001491, 2003.

Calvert, J. G.: Glossary of atmospheric chemistry terms (Recommendations 1990), Pure Appl. Chem., 62, 2167–2219, https://doi.org/10.1351/pac199062112167, 1990.

Chen, S., Cao, R., Xie, Y., Zhang, Y., Tan, W., Chen, H., Guo, P., and Zhao, P.: Study of the seasonal variation in Aeolus wind product performance over China using ERA5 and radiosonde data, Atmos. Chem. Phys., 21, 11489–11504, https://doi.org/10.5194/acp-21-11489-2021, 2021.

de Kloe, J., Stoffelen, A., Tan, D., Andersson, E., Rennie, M., Dabas, A., Poli, P., and Huber, D.: Aeolus Data Innovation Science Cluster DISC ADM-Aeolus Level-2B/2C Processor Input/Output Data Definitions Interface Control Document, ESA, https://earth.esa.int/eogateway/documents/20142/37627/Aeolus-L2B-2C-Input-Output-DD-ICD.pdf, last access: 10 February 2022.

Dolman, B., Reid, I., and Kane, T.: The Australian Wind Profiler Network, WMO Technical Conference on Meteorological and Environmental Instruments and Methods of Observation (TECO-2016), 27–30 September 2016, Madrid, Spain, https://www.wmocimo.net/eventpapers/session2/O2(3)_Dolman_The%20Australian%20Wind%20Profiler%20Network.pdf (last access: 10 January 2022), 2016.

Dolman, B. K., Reid, I. M., and Tingwell, C.: Stratospheric tropospheric wind profiling radars in the Australian network, Earth Planets Space, 70, 170, https://doi.org/10.1186/s40623-018-0944-z, 2018.

ESA: Satellites track unusual Saharan dust plume, European Space Agency, https://www.esa.int/Applications/Observing_the_Earth/Satellites_track_unusual_Saharan_dust_plume (last access: 28 August 2021), 2020a.

ESA: A Guide to Aeolus Range Bin Settings, European Space Agency, https://earth.esa.int/eogateway/news/a-guide-to-aeolus-range-bin-settings (last access: 18 February 2022), 2020b.

ESA: ESA Aeolus Online Dissemination System, ESA [data set], https://aeolus-ds.eo.esa.int/oads/access/ (last access: 5 January 2022), 2021.

Gao, C., Li, Y., and Chen, H.: Diurnal Variations of Different Cloud Types and the Relationship between the Diurnal Variations of Clouds and Precipitation in Central and East China, Atmosphere, 10, 304, https://doi.org/10.3390/atmos10060304, 2019.

Guo, J., Liu, B., Gong, W., Shi, L., Zhang, Y., Ma, Y., Zhang, J., Chen, T., Bai, K., Stoffelen, A., de Leeuw, G., and Xu, X.: Technical note: First comparison of wind observations from ESA's satellite mission Aeolus and ground-based radar wind profiler network of China, Atmos. Chem. Phys., 21, 2945–2958, https://doi.org/10.5194/acp-21-2945-2021, 2021.

Houchi, K., Stoffelen, A., Marseille, G. J., and De Kloe, J.: Comparison of wind and wind shear climatologies derived from high-resolution radiosondes and the ECMWF model, J. Geophys. Res., 115, D22123, https://doi.org/10.1029/2009JD013196, 2010.

Ingmann, P. and Straume, A. G.: ADM-Aeolus Mission Requirements Document, ESA, 57 pp., https://esamultimedia.esa.int/docs/EarthObservation/ADM-Aeolus_MRD.pdf (last access: 5 January 2022), 2016.

Iwai, H., Aoki, M., Oshiro, M., and Ishii, S.: Validation of Aeolus Level 2B wind products using wind profilers, ground-based Doppler wind lidars, and radiosondes in Japan, Atmos. Meas. Tech., 14, 7255–7275, https://doi.org/10.5194/amt-14-7255-2021, 2021.

Krisch, I. and the Aeolus DISC: Data quality of Aeolus wind measurements, EGU General Assembly 2020, Online, 4–8 May 2020, EGU2020-9471, https://doi.org/10.5194/egusphere-egu2020-9471, 2020.

Lin, W., Portabella, M., Stoffelen, A., Vogelzang, J., and Verhoef, A.: On mesoscale analysis and ASCAT ambiguity removal, Q. J. Roy. Meteor. Soc., 142, 1745–1756, https://doi.org/10.1002/qj.2770, 2016.

Marseille, G.-J., de Kloe, J., Marksteiner, U., Reitebuch, O., Rennie, M., and de Haan, S.: NWP calibration applied to Aeolus Mie channel winds, Q. J. Roy. Meteor. Soc., 148, 1020–1034, https://doi.org/10.1002/qj.4244, 2022.

Martin, A., Weissmann, M., Reitebuch, O., Rennie, M., Geiß, A., and Cress, A.: Validation of Aeolus winds using radiosonde observations and numerical weather prediction

model equivalents, Atmos. Meas. Tech., 14, 2167–2183, https://doi.org/10.5194/amt-14-2167-2021, 2021.

Met Office: Wind Profiler Observations, Part of the Met Office MetDB System, NCAS British Atmospheric Data Centre [data set], https://catalogue.ceda.ac.uk/uuid/9e22544a66ba7aa902ae431b1ed609d6 (last access: 18 December 2021), 2008.

Portabella, M. and Stoffelen, A.: On Scatterometer Ocean Stress, J. Atmos. Ocean. Tech., 26, 368–382, https://doi.org/10.1175/2008JTECHO578.1, 2009.

Rennie, M., Tan, D., Andersson, E., Poli, P., Dabas, A., De Kloe, J., Marseille, G.-J., and Stoffelen, A.: Aeolus Level-2B Algorithm Theoretical Basis Document (Mathematical Description of the Aeolus L2B Processor), ESA, 124 pp., https://earth.esa.int/eogateway/documents/20142/37627/Aeolus-L2B-Algorithm-ATBD.pdf (last access: 17 October 2021), 2020.

Rennie, M. P. and Isaksen, L.: The NWP impact of Aeolus Level-2B Winds at ECMWF, Technical memorandum, ECMWF, 110 pp., https://doi.org/10.21957/alift7mhr, 2020.

Rennie, M.P., Isaksen, L., Weiler, F., de Kloe, J., Kanitz, T., and Reitebuch, O.: The impact of Aeolus wind retrievals on ECMWF global weather forecasts, Q. J. Roy. Meteor. Soc., 147, 3555–3586, https://doi.org/10.1002/qj.4142, 2021.

Ribal, A. and Young, I. R.: Global Calibration and Error Estimation of Altimeter, Scatterometer, and Radiometer Wind Speed Using Triple Collocation, Remote Sens., 12, 1997, https://doi.org/10.3390/rs12121997, 2020.

Ruppert, D.: Statistics and Data Analysis for Financial Engineering, 1st edn., Springer Texts in Statistics, Springer, New York, NY, USA, https://doi.org/10.1007/978-1-4419-7787-8, 2011.

Skamarock, W. C.: Evaluating Mesoscale NWP Models Using Kinetic Energy Spectra, Mon. Weather Rev., 132, 3019–3032, https://doi.org/10.1175/MWR2830.1, 2004.

Stoffelen, A.: Toward the true near-surface wind speed: Error modeling and calibration using triple collocation, J. Geophys. Res., 103, 7755–7766, https://doi.org/10.1029/97JC03180, 1998.

Stoffelen, A., Vogelzang, J., and Marseille, G.-J.: High-resolution wind data-assimilation guide, Royal Netherlands Meteorological Institute, 26 pp., https://nwp-saf.eumetsat.int/site/download/documentation/scatterometer/reports/High_Resolution_Wind_Data_Assimilation_Guide_1.3.pdf (last access: 27 January 2022), 2020.

Tozer, B, Sandwell, D. T., Smith, W. H. F., Olson, C., Beale, J. R., and Wessel, P.: Global bathymetry and topography at 15 arc sec: SRTM15+, Earth Space Sci., 6, 1847–1864, https://doi.org/10.1029/2019EA000658, 2019.

Uieda, L., Tian, D., Leong, W. J., Jones, M., Schlitzer, W., Toney, L., Grund, M., Yao, J., Magen, Y., Materna, K., Newton, T., Anant, A., Ziebarth, M., Quinn, J., and Wessel, P.: PyGMT: A Python interface for the Generic Mapping Tools (v0.5.0), Zenodo [code], https://doi.org/10.5281/zenodo.5607255, 2021.

Vallejos-Burgos, F., Coudert, F.-X., and Kaneko, K.: Air separation with graphene mediated by nanowindow-rim concerted motion, Nat. Commun., 9, 1812, https://doi.org/10.1038/s41467-018-04224-6, 2018.

Vogelzang, J. and Stoffelen, A.: Triple collocation, Royal Netherlands Meteorological Institute, 22 pp., https://cdn.knmi.nl/system/data_center_publications/files/000/068/914/original/triplecollocation_nwpsaf_tr_kn_021_v1.0.pdf?1495621500 (last access: 27 January 2022), 2012.

Vogelzang, J., Stoffelen, A., Verhoef, A., and Figa-Saldaña, J.: On the quality of high-resolution scatterometer winds, J. Geophys. Res., 116, C10033, https://doi.org/10.1029/2010JC006640, 2011.

Wallace, J. M. and Hobbs, P. V.: Atmospheric Science An Introductory Survey, 2nd edn., International geophysics series, 92, Elsevier, USA, ISBN 978-0-12-732951-2, 2006a.

Wallace, J. M. and Hobbs, P. V.: Cloud Microphysics, in: Atmospheric Science An Introductory Survey, Elsevier, USA, 209–263, ISBN 978-0-12-732951-2, 2006b.

Wessel, P., Luis, J. F., Uieda, L., Scharroo, R., Wobbe, F., Smith, W. H. F., and Tian, D.: The Generic Mapping Tools Version 6, Geochem. Geophys. Geosyst., 20, 5556–5564, https://doi.org/10.1029/2019GC008515, 2019.

World Meteorological Organization (WMO): Proceedings of the 3rd WMO Workshop on The Impact of Various Observing Systems on Numerical Weather Prediction, WMO Workshop on the impact of various observing systems on numerical weather prediction 3rd session, 9–12 March 2004, Alpbach, Austria, WMO/TD-No. 1228, https://library.wmo.int/index.php?lvl=notice_display&id=9214#.YsvaXuxBycY (last access: 22 January 2022), 2005.

Wu, S., Sun, K., Dai, G., Wang, X., Liu, X., Liu, B., Song, X., Reitebuch, O., Li, R., Yin, J., and Wang, X.: Inter-comparison of wind measurements in the atmospheric boundary layer and the lower troposphere with Aeolus and a ground-based coherent Doppler lidar network over China, Atmos. Meas. Tech., 15, 131–148, https://doi.org/10.5194/amt-15-131-2022, 2022.

Zhang, W., Guo, J., Miao, Y., Liu, H., Zhang, Y., Li, Z., and Zhai, P.: Planetary boundary layer height from CALIOP compared to radiosonde over China, Atmos. Chem. Phys., 16, 9951–9963, https://doi.org/10.5194/acp-16-9951-2016, 2016.

A.2 Article II: The impact of Aeolus winds on near-surface wind forecasts over tropical ocean and high-latitude regions

Zuo, H., & Hasager, C. B. (2023). The impact of Aeolus winds on near-surface wind forecasts over tropical ocean and high-latitude regions. *Atmospheric Measurement Techniques*, *16*, 3901–3913. https://doi.org/10.5194/amt-16-3901-2023

Atmos. Meas. Tech., 16, 3901–3913, 2023
https://doi.org/10.5194/amt-16-3901-2023

Atmospheric Measurement Techniques
Open Access
EGU

The impact of Aeolus winds on near-surface wind forecasts over tropical ocean and high-latitude regions

Haichen Zuo and Charlotte Bay Hasager

Department of Wind and Energy Systems, Technical University of Denmark, 4000 Roskilde, Denmark

Correspondence: Haichen Zuo (hazu@dtu.dk)

Received: 15 November 2022 – Discussion started: 6 December 2022
Revised: 24 June 2023 – Accepted: 6 July 2023 – Published: 24 August 2023

Abstract. To detect global wind profiles and improve numerical weather prediction (NWP), the European Space Agency (ESA) launched the Aeolus satellite carrying a spaceborne Doppler wind lidar in 2018. After the successful launch, the European Centre for Medium-Range Weather Forecasts (ECMWF) performed the observing system experiments (OSEs) to evaluate the contribution of Aeolus data to NWP. This study aims to assess the impact of Aeolus wind assimilation in the ECMWF model on near-surface (10 m height) wind forecasts over tropical ocean regions by taking buoy measurements for reference and over high-latitude regions by taking weather station data for reference for the year 2020. The assessments were conducted mainly through intercomparison analysis. The results show that Aeolus data assimilation has a limited impact on sea surface wind forecasts for tropical regions when compared with buoy measurements. For the high-latitude regions in the Northern Hemisphere, Aeolus is able to improve near-surface wind forecasts. This positive impact is more evident as the forecast time step is extended, during the first half year of 2020 and during the winter months. In addition, the v component tends to benefit more from the Aeolus observations than the u component. For the Southern Hemisphere, a few error reductions are observed but exist randomly. Overall, this in situ data-based assessment expands our understanding of the role of Aeolus data assimilation with the global NWP model in predicting near-surface wind for tropical oceans and high-latitude regions.

1 Introduction

For characterizing global wind profiles and improving numerical weather prediction (NWP), the first spaceborne Doppler wind lidar (DWL) carried by the Aeolus satellite was launched in August 2018 by the European Space Agency (ESA). The mission operated for more than 4 years and ended in April 2023. Following a sun-synchronous orbit, Aeolus passed over the Equator at 06:00 local time (LT) during descending orbits and 18:00 LT during ascending orbits and sampled the whole globe every 12 h with eight orbits. Wind retrieval of Aeolus is based on the Doppler-shifted frequency between emitted light pulses and backscattered light from air molecules (i.e. Rayleigh scattering) as well as from large particles, such as cloud droplets and ice crystals, in the atmosphere (i.e. Mie scattering). By measuring this small difference, wind velocity along the line of sight (LOS) can be obtained, which is further converted to the approximately east–west horizontal LOS wind component using the off-nadir angle of 35° (Andersson et al., 2008). The detected wind profiles, ranging from the surface to about 30 km in height with 24 vertical bins, can be used to improve NWP, capture gravity waves, track volcanic eruptions, etc. (Banyard et al., 2021; Rennie et al., 2021; Parrington et al., 2022).

After the successful launch, calibration and validation work has been widely carried out worldwide. Owing to the continually improved data processing chain, from baseline 10 with M1-temperature-based bias correction and daily updates of global offset bias removal (Data Innovation and Science Cluster, 2020), the systematic errors in both Rayleigh-clear winds and Mie-cloudy winds are almost within 0.5 m s^{-1}, with the exception of some cases in the polar regions, and the random errors mainly vary between 4 and 8 m s^{-1} for Rayleigh-clear winds and between 2.0 and

Published by Copernicus Publications on behalf of the European Geosciences Union.

$5\,m\,s^{-1}$ for Mie-cloudy winds (Belova et al., 2021; Iwai et al., 2021; Witschas et al., 2022; Zuo et al., 2022). However, what should be noted is that Aeolus has suffered unexpected signal loss since the launch, probably due to the decreasing emitted laser energy for the FM-A period (August 2018–June 2019) and/or laser-induced contamination for the FM-B period (July 2019–September 2022) (Straume-Lindner et al., 2021). The data quality assessment based on the second reprocessed data set (2B11) by the European Centre for Medium-Range Weather Forecasts (ECMWF) revealed that the estimated random error in Rayleigh-clear wind increased by 40 % from ~ 5 to $\sim 7\,m\,s^{-1}$ during July 2019–October 2020 due to the gradual signal reduction in DWL, while this instrument issue has less influence on Mie-cloudy winds, with estimated random errors remaining at $\sim 3.5\,m\,s^{-1}$ (Rennie and Isaksen, 2023).

Although Aeolus suffers from unexpected signal loss and growing errors, its wind products have been employed to improve NWP through data assimilation, an approach that integrates recent observations with a previous forecast to achieve the best estimate of the current atmospheric state (ECMWF, 2020). For evaluating the contribution of Aeolus observations to NWP, the observing system experiments (OSEs) with and without Aeolus data assimilation have been performed with global NWP models at many institutions, including the ECMWF, National Oceanic and Atmospheric Administration (NOAA), Deutscher Wetterdienst (DWD), Météo-France, and UK Met Office (Cress et al., 2022; Garrett et al., 2022; Forsythe and Halloran, 2022; Pourret et al., 2022; Rennie and Isaksen, 2023). The assessment of the ECMWF OSEs demonstrated that Aeolus winds are able to improve vector wind and temperature forecasts, especially in the upper troposphere and/or lower stratosphere over tropical and polar regions (Rennie et al., 2021). Similar results were also found from the OSEs with the NOAA's Global Forecast System, the DWD model, and the Environment and Climate Change Canada Global Forecast System (Cress et al., 2022; Garrett et al., 2022; Laroche and St-James, 2022). Moreover, regarding the weather and climate events, Aeolus is able to improve the track forecasts for tropical cyclones in the eastern Pacific basin and Atlantic basin (Garrett et al., 2022) and benefits the forecasts of the West African Monsoon as well as the changes in the El Niño–Southern Oscillation (ENSO) state over the eastern Pacific by capturing the large-scale atmospheric circulation (Cress et al., 2022).

However, the existing assessments mainly focused on the forecasts at pressure levels or upper air, while the impacts of Aeolus data assimilation on near-surface wind forecasts lack detailed study. This research gap needs to be complemented since the relevant scientific investigation could provide valuable information for future applications in wind-related activities, such as ocean shipping and wind farm operation and maintenance. Due to the relatively low spatial and temporal resolution of Aeolus wind observations, global models are more likely to benefit from Aeolus data assimilation than high-resolution regional models (Hagelin et al., 2021; Mile et al., 2022; Rennie and Isaksen, 2023). Therefore, as a starting point, we would like to focus on the ECMWF model first. This will give us a better understanding of the influence of Aeolus on near-surface wind forecasts, which in turn guides us in applying Aeolus winds to regional models for practical applications. Considering that tropical oceans and polar regions are favourable to extreme weather but lack in situ measurements, and the model performance is usually not satisfactory in these regions, yielding, for example, large bias over the Intertropical Convergence Zone (ITCZ) (Sandu et al., 2020), we would like to investigate whether Aeolus can contribute to more reliable wind forecasts for these regions.

Regarding the reference data set for evaluation, many verifications related to Aeolus OSEs were conducted by intercomparing with model analysis that has global coverage and deals with the representation error between the model scale and scales of observations (Garrett et al., 2022; Laroche and St-James, 2022; Rennie and Isaksen, 2023). However, there are fewer in situ measurements available over tropical and polar regions, and the mesoscale convections are not resolved well in the global NWP models, which leads to the large uncertainties in model analysis data in these regions (Sandu et al., 2020; King et al., 2022). Given this, taking in situ measurements as the reference can avoid this issue to some extent.

Hence, to complement the existing studies, this study aims to assess the impact of Aeolus wind assimilation on near-surface wind forecasts over tropical ocean regions between 30° N and 30° S by taking buoy measurements for reference. Furthermore, we investigated the high-latitude region $> 60°$ N in the Northern Hemisphere (NH) and the high-latitude region $> 60°$ S in the Southern Hemisphere (SH) by taking weather station data for reference. Our hypothesis is that the assimilation of Aeolus winds will reduce the forecast error. Since the overall data quality of Aeolus is reduced in the second half year of 2020 compared to the first half year due to the weakening signals, our hypothesis is that the assimilation of Aeolus winds can reduce the forecast error relatively more during the first half year compared to the second half year. In the tropics, seasonal effects are very limited, while in the high-latitude regions, the seasonal variability is high, so for those we also investigated the forecast for the seasons. The assessments were conducted mainly through inter-comparison analysis based on the high-resolution $T_{co}639$ OSEs in the ECMWF model for the entire year of 2020.

Sections 2 and 3 introduce the data and methods used in this study. Section 4 presents the main research findings, followed by Sect. 5 for discussions. The final section makes a short summary of the study and draws conclusions.

2 Data

2.1 Observing system experiments with ECMWF model

This study is based on the ECMWF OSEs with the second reprocessed Aeolus L2B baseline 11 data and the near real-time L2B baseline 11/12 data assimilated during the FM-B period (Rennie and Isaksen, 2023). The applied model version is CY47R2 with an atmosphere outer-loop resolution of $T_{co}639$ L137 ($\sim$ 18 km grid size). Observations from nominally operational satellites and conventional sources were assimilated. The OSEs include a control experiment without Aeolus assimilation and an experiment with Aeolus Rayleigh-clear and Mie-cloudy wind assimilation through the four-dimensional variational (4D-Var) data assimilation technique. For the lower troposphere ($>$ 850 hPa), only Mie-cloudy winds with an estimated error smaller than 5 m s^{-1} were assimilated into the model. Detailed information on quality control decisions for the OSEs is documented in Rennie and Isaksen (2023). Figure 1 illustrates the geographical distribution of the averaged number of L2B Mie-cloudy winds assimilated per cycle below 850 hPa. More low-level Aeolus winds are assimilated over the ocean regions than inland regions and over low- to mid-latitude regions than high-latitude regions.

The 10 d forecasts based on the 00:00 UTC analysis of the zonal (u) and meridional (v) wind components at 10 m height were obtained from the ECMWF Meteorological Archival and Retrieval System (MARS) for evaluation (ECMWF Research Department, 2022). The interval of forecast steps is 24 h. The data cover the completed year of 2020.

2.2 Buoy measurements

The tropical moored-buoy measurements over the Atlantic Ocean, Indian Ocean and Pacific Ocean were obtained from the Global Tropical Moored Buoy Array (Pacific Marine Environmental Laboratory, 2022). The extracted parameters include the zonal (u) and meridional (v) wind components, wind speed, and wind direction with a temporal resolution of 10 min or 1 h. The missing values and data flagged as low-quality have been removed. Finally, there are 11 buoys available in the Atlantic Ocean, 9 in the Indian Ocean and 55 in the Pacific Ocean, the locations of which are displayed in Fig. 2. To make all measurements have an identical temporal resolution, we averaged the 10 min wind speeds to hourly wind speeds. Furthermore, to collocate with wind forecasts from the OSEs, the buoy winds were extrapolated from an anemometer height of 3.5 or 4 to 10 m by using the method described in Bidlot et al. (2002).

2.3 Weather station data

Surface synoptic observations over high-latitude regions ($>$ 60° N and $>$ 60° S) were extracted from the global hourly Integrated Surface Database (ISD) (National Centers for Environmental Information, 2022). Only the wind speeds and directions that passed all quality control checks were kept for further analysis. Additionally, we calculated the correlation coefficients (R) between in situ measurements and the control experiments at T+0 h, and the stations with weak correlations ($R < 0.5$) were removed. One reason is that when the poor correlations are caused by very limited data samples during the study period, such as due to freezing or instrument malfunction, we consider the data quality of those available samples to still be questionable. Another reason is that the weak correlations may imply a limited spatial representativeness of those stations, especially over the complex terrain. After quality control, there are 751 (223) and 56 (30) stations available (removed) over the high-latitude regions in the Northern Hemisphere and Southern Hemisphere, respectively (Fig. 2).

3 Method

To evaluate the wind forecasts from OSEs, we take buoy measurements or weather station observations for reference. We quantified the normalized change in the root-mean-square errors (RMSEs) with and without Aeolus data assimilation for all paired data samples, thus determining whether Aeolus can improve the model performance or not over each study region. The normalized change in RMSE (NCRMSE) is given as

$$\mathrm{NCRMSE} = \frac{\sqrt{\frac{\sum_{i=1}^{N}\left(f_{i,\text{with Aeolus}}-o_{i,\text{in situ}}\right)^2}{N}}-\sqrt{\frac{\sum_{i=1}^{N}\left(f_{i,\text{no Aeolus}}-o_{i,\text{in situ}}\right)^2}{N}}}{\sqrt{\frac{\sum_{i=1}^{N}\left(f_{i,\text{no Aeolus}}-o_{i,\text{in situ}}\right)^2}{N}}}, \quad (1)$$

where $f_{i,\text{with Aeolus/no Aeolus}}$ is the wind forecast with or without Aeolus data assimilation, $o_{i,\text{in situ}}$ is the in situ measurements from either buoys or weather stations, and N is the total number of paired data samples for each study region or each case. The statistical significance of NCRMSE was quantified at the 95 % confidence interval (not shown on plots).

The analyses were performed for each ocean basin, regions $>$ 60° N and $>$ 60° S, respectively, aiming to provide error information geographically. We focus on error information of each wind component as well as wind speed instead of vector wind as the former is more relevant to practical applications. We also divided the study period into 2 half years to evaluate the sensitivity of wind forecasts to Aeolus data quality. For high-latitude regions, the study was also carried out for each season. Moreover, for the region $>$ 60° N, we divided the data samples into four categories based on the in situ wind speeds (Table 1) and investigated the impact of Aeolus under different wind speed ranges (Met Office, 2023). Apart from these, the Pearson correlation coefficients

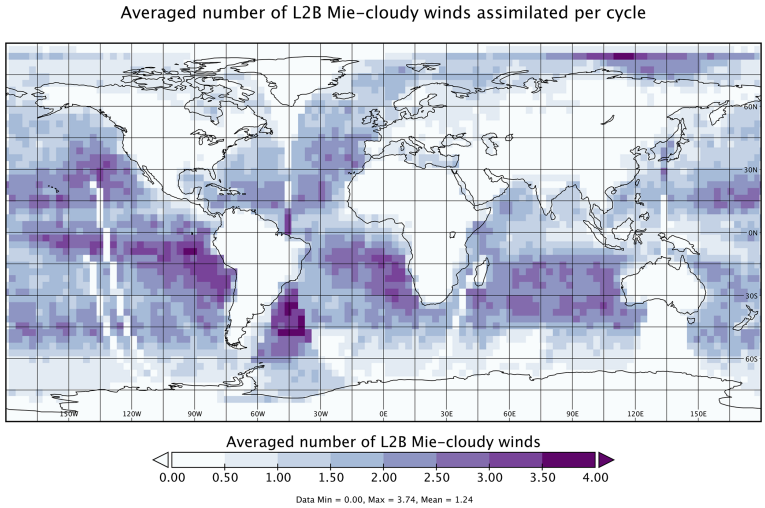

Figure 1. The averaged number of L2B Mie-cloudy winds at pressure > 850 hPa assimilated into the model.

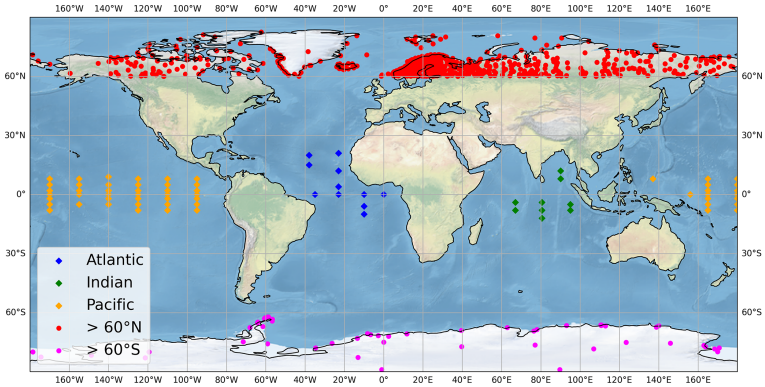

Figure 2. The geographical location of moored buoys in the tropical oceans and weather stations at high latitudes > 60° N and high latitudes > 60° S (background image made with Natural Earth. Free vector and raster map data at https://www.naturalearthdata.com/, last access: 18 June 2023).

Table 1. Wind speed (wspd) categories.

Category	Wind speed range ($m\,s^{-1}$)	Description
a	wspd $\leq$ 6.0	light air to gentle breeze
b	6.0 < wspd $\leq$ 11.0	moderate breeze to fresh breeze
c	11.0 < wspd $\leq$ 17.0	strong breeze to near gale
d	wspd > 17.0	gale to hurricane

between forecasts and reference data and between two forecasts with and without Aeolus were also calculated as the additional statistical information to facilitate the study.

4 Results

4.1 Tropical oceans

4.1.1 Inter-comparison analysis

Figure 3 shows the NCRMSEs from inter-comparison analyses for three ocean basins. For the tropical Atlantic Ocean, the negative values are mainly found within T+72 h for the v component and wind speed. The results for the tropical Indian Ocean do not show any trend in error reduction for wind components and wind speed. Compared to the tropical Atlantic Ocean and Indian Ocean, the Pacific witnesses

negative values at more forecast steps, but the magnitude is weaker, mainly within 1 %. The negative values at T+48 h for both wind components and wind speed are common for the three ocean basins. Unfortunately, none of the negative NCRMSEs are statistically significant at the 95 % confidence interval; thus, the overall impact of Aeolus on sea surface wind forecasts is neutral for tropical regions. In addition, Aeolus data quality appears to have no influence on improving surface wind forecasts over the tropical ocean regions, as shown in Fig. 4 by taking the Pacific Ocean as an example.

4.1.2 Correlations of data sets

The correlation coefficients show that the forecast experiment with and without Aeolus is highly correlated up to T+120 h, with R values greater than 0.9 for both the u and v components as well as wind speed. As the forecast is extended, the correlations between the two forecasts and between the forecasts and buoy measurements weaken but do not decrease too much for tropical ocean basins with R values greater than 0.7 at T+240 h for most cases. Figure 5 is an example of the tropical Pacific at the T+120 h forecast step. The results show the u and v components with R values around 0.95 for the forecasts with and without Aeolus, while for wind speed, the R value is around 0.90. The R values for the u and v components are around 0.81 (Fig. 5e and f) and 0.80 (Fig. 5h and i) for the forecasts (with and without Aeolus data) versus buoy data, which indicates that there is almost no increase in correlation after assimilating Aeolus winds. In summary, the zonal and meridional wind components are better resolved in the forecast model than the wind speed. The correlations do not reveal much improvement in forecast skill between the two forecasts. Similar results are also found for the tropical Atlantic Ocean and Indian Ocean (not shown).

4.2 High-latitude region in the Northern Hemisphere (> 60° N)

4.2.1 Inter-comparison analysis

Over the high-latitude region in the Northern Hemisphere, the NCRMSEs for the u and v components and wind speed are almost negative and decrease as the forecast time is extended, which implies that Aeolus tends to make a positive contribution to medium-range, near-surface wind forecasts (Fig. 6). A significant positive impact is found at T+120 h, T+216 h and T+240 h for the u component; from T+192 h for the v component; and at T+192 h and T+216 h for wind speed. Aeolus was found to have a more positive impact on the v component, with the largest error reduction of 2.4 % at T+216 h. Regarding the results for different wind speed categories (Fig. 7), the noticeable error reductions tend to exist earlier from the T+96 h forecast step for moderate to fresh breezes ($6 < \text{wspd} \leq 11\,\text{m s}^{-1}$) compared to the light-

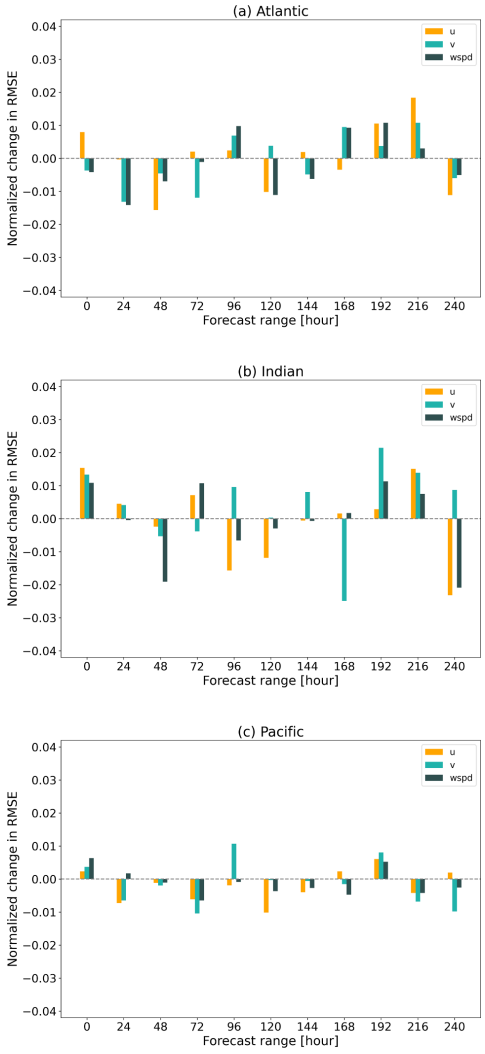

Figure 3. Normalized change in RMSE for the u and v wind components and wind speed (wspd) for the tropical Atlantic Ocean **(a)**, Indian Ocean **(b)** and Pacific Ocean **(c)** for the year 2020. The ECMWF OSE forecasts with and without Aeolus are compared against buoy data. Note that negative values indicate error reduction, implying an improvement in the forecast with Aeolus assimilation.

wind category; for the category of strong breeze to near gale ($11 < \text{wspd} \leq 17\,\text{m s}^{-1}$), the negative NCRMSEs for the v component exist from the T+120 h forecast step, while the largest impacts on the u and v components are observed at T+216 h and T+192 h, respectively, when wind speeds are greater than $17\,\text{m s}^{-1}$, but a further demonstration is required due to a limited number of data samples in this category (N

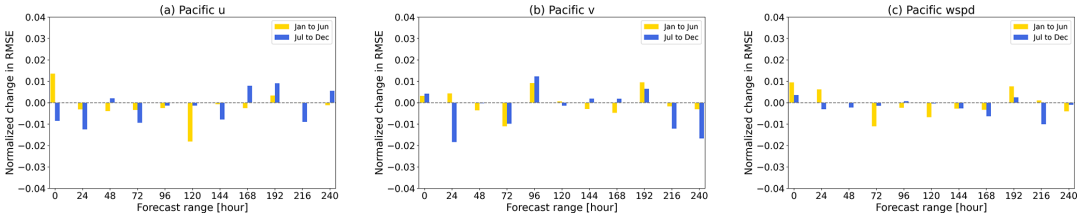

Figure 4. Normalized change in RMSE for the u and v wind components and wind speed (wspd) during the first and the second half year of 2020 for the tropical Pacific Ocean. The ECMWF OSE forecasts with and without Aeolus are compared against buoy data.

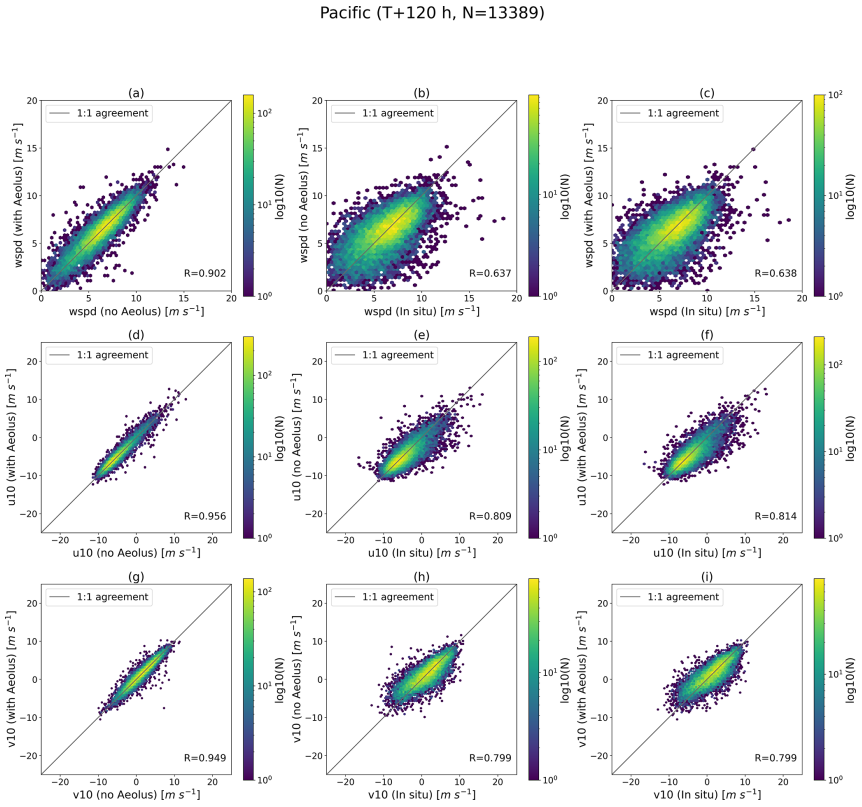

Figure 5. Hexagonal binning plots of the u and v components and wind speed (wspd) at the T+120 h forecast step for the tropical Pacific Ocean for the year 2020 based on ECMWF OSE forecasts with and without Aeolus and buoy data. The colour of each hexagon indicates the number of samples in it.

of around 1200). In terms of the results for 2 half years, the NCRMSEs of the u and v components are generally lower from T+120 h during the first half year compared with those for the second half year (Fig. 8a and b). This suggests that Aeolus's data quality is important for near-surface wind forecasts. With respect to the results for each season (Fig. 9), Aeolus makes a greater contribution from T+120 h onwards to the u component forecasts during boreal winter (January, February and December) than during boreal summer (June, July and August). For the v component, the most noticeable error reductions of 3.3 % exist at T+168 h during winter months and 4.4 % at T+216 h during spring (March, April and May).

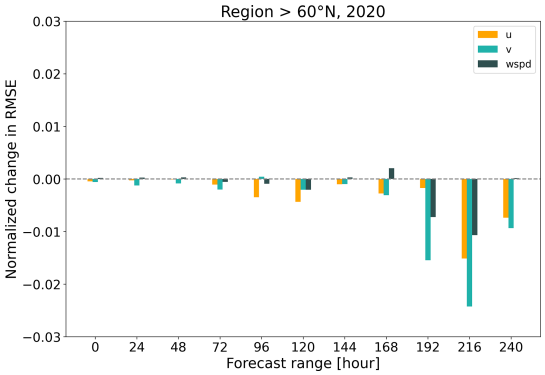

Figure 6. Normalized change in RMSE of the u and v components and wind speed (wspd) as a function of forecast range for the region > 60° N for the year 2020. The ECMWF OSE forecasts with and without Aeolus are compared against weather station data.

4.2.2 Correlations of data sets

Regarding the correlations for the region > 60° N, the wind components and wind speed between the two forecasts with and without Aeolus assimilation are well correlated as the forecast is extended, with R values greater than 0.90 until T+120 h (Fig. 10a, d and g). Moreover, with the forecast extended, the R values of the forecasts with Aeolus versus in situ measurements are slightly larger than the ones without Aeolus data, which is in line with the inter-comparison analysis, suggesting a minimal improvement in wind forecasts. However, in contrast to the inter-comparison analysis, the R value is not sensitive enough to reflect which wind component can benefit more from Aeolus data assimilation.

4.3 High-latitude region in the Southern Hemisphere (> 60° S)

4.3.1 Inter-comparison analysis

For the Southern Hemisphere, the impact of Aeolus on wind forecasts is nearly neutral when considering the whole study period, with a significant error reduction only at T+216 h for wind speed forecasts (Fig. 11). Regarding the results for 2 different half years, more negative NCRMSEs of the u component and wind speed were found within T+96 h and at T+216 h and T+240 h during the first half year of 2020 (Fig. 12). With respect to seasonal results (Fig. 13), as the forecast range is extended, there are more negative NCRMSEs in the u component than in the v component, although these exist randomly in any season.

4.3.2 Correlations of data sets

Regarding the correlations for the region > 60° S, the wind components and wind speed between the two forecasts show strong agreement as the forecast is extended, with R values consistently greater than 0.89 up to T+120 h (Fig. 14a, d and g). This pattern is comparable with the results for the region > 60° N, although the number of data samples is much lower in the region > 60° S. Moreover, the R values decrease gradually with forecast time, but the correlations for the u and v components are stronger than those for the wind speed for all forecast steps. In addition, the correlations between the forecasts and the in situ measurements are generally consistent with the inter-comparison results, with R values of the forecasts with Aeolus versus in situ data higher than the ones without Aeolus, corresponding to the negative NCRMSEs.

5 Discussion

By taking in situ measurements for reference, we evaluated the impact of Aeolus data assimilation on wind forecasts at the near-surface level based on the ECMWF OSEs. According to the results of inter-comparison analyses for tropical oceans, the impact of Aeolus on sea surface wind forecasts is nearly neutral overall. However, negative NCRMSE values are observed across all three ocean basins at the T+48 h forecast step. Despite not being statistically significant, this result is consistent with the verifications based on the model analysis at the ECMWF (Rennie and Isaksen, 2023), but further demonstration is required with more in situ measurements.

For the NH high-latitude region, Aeolus makes more positive impacts as the forecast is extended. This result is partly comparable with the analysis-based verifications at the ECMWF, with a noticeable positive impact obtained at the T+216 h forecast step (Rennie and Isaksen, 2023). The main difference is that in our study, this evident positive impact exists at more forecast steps from T+192 h to T+240 h, which is in part due to the different reference data we use and the different spatial coverage they have. In addition, since there are a limited number of low-level Aeolus winds inland assimilated into the ECMWF model, we suspect that this positive impact is probably associated with the downward propagation of Aeolus increments to the surface as the changes in stratospheric initial conditions can affect tropospheric circulation in subsequent forecasts (Kodera et al., 1990; Christiansen, 2001; Charlton et al., 2004; Tripathi et al., 2015). Moreover, the greater positive impact is found for the v component at many forecast steps. One possible reason is that at higher latitudes, Aeolus measurements are closer to meridional winds, thus leading to a greater impact on the v component.

To assess the impact of Aeolus data quality on its contribution to wind forecasts, we also divided the study period into two half-year periods. There are more evident error re-

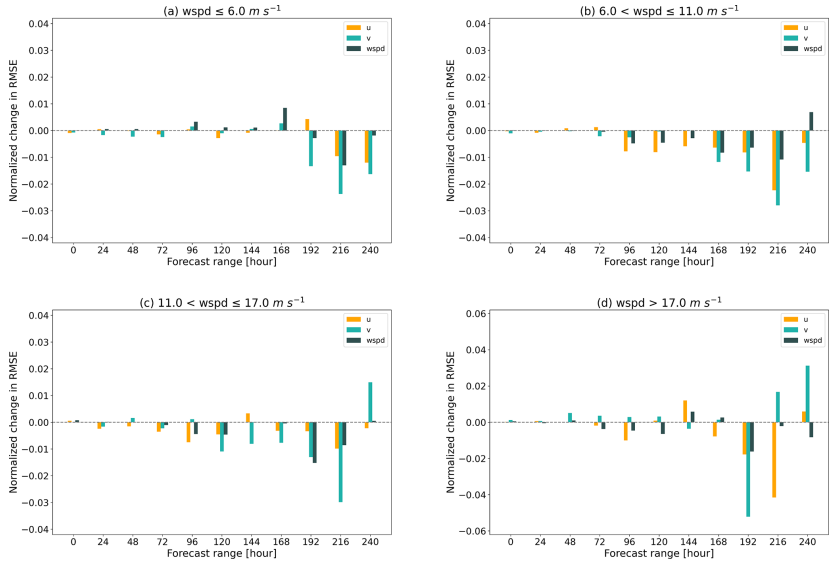

Figure 7. Same as Fig. 6 but for different wind speed ranges.

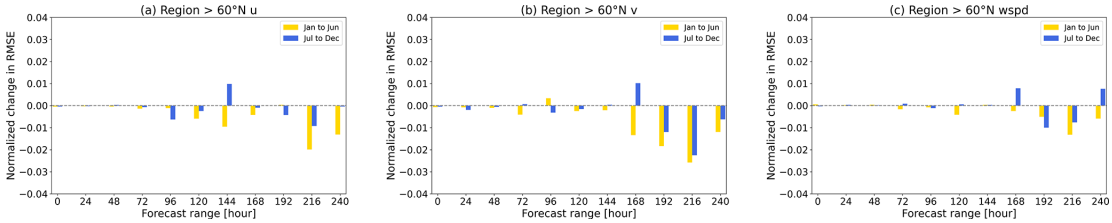

Figure 8. Normalized change in RMSE of the u and v components and wind speed (wspd) as a function of forecast range during each half year of 2020 for the region > 60° N. The ECMWF OSE forecasts with and without Aeolus are compared against weather station data.

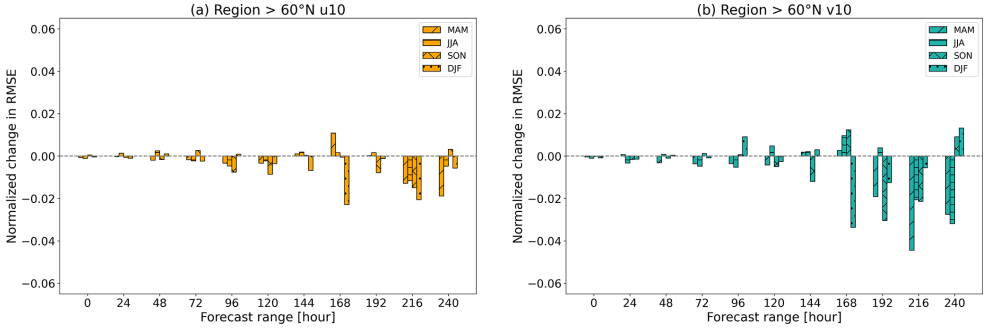

Figure 9. Seasonal variation in normalized change in RMSE of the u and v components as a function of forecast range for the region > 60° N for the year 2020. The ECMWF OSE forecasts with and without Aeolus are compared against weather station data. MAM: March, April and May; JJA: June, July and August; SON: September, October and November; DJF: December, January and February.

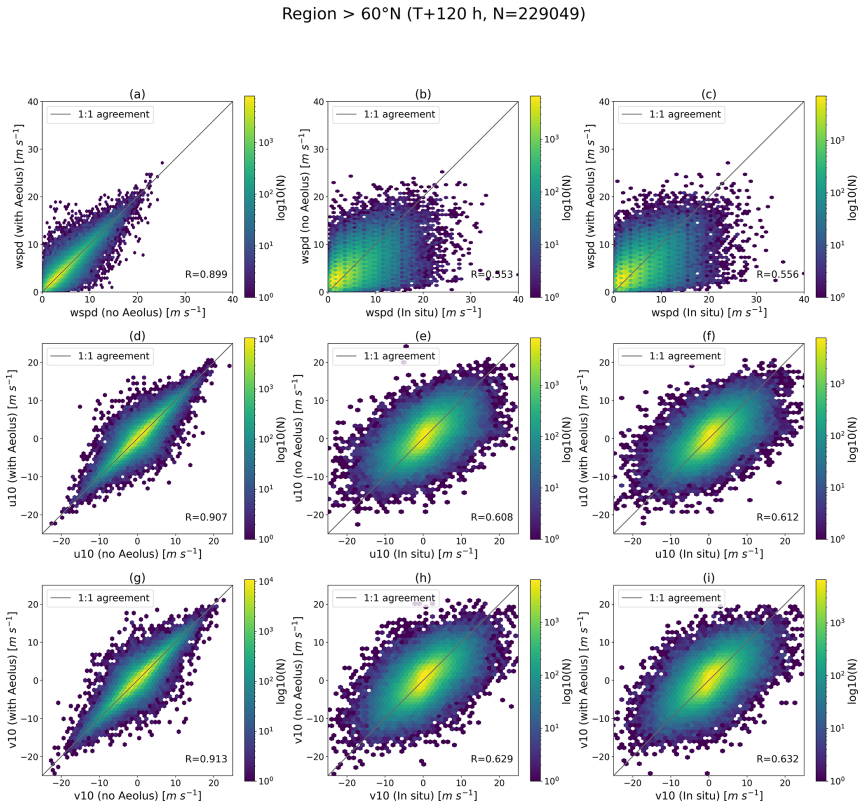

Figure 10. Hexagonal binning plots of the u and v components and wind speed at $T+120$ h for the region $> 60°$ N for the year 2020 based on the ECMWF OSE forecasts with and without Aeolus and weather station data. The colour of each hexagon indicates the number of samples in it.

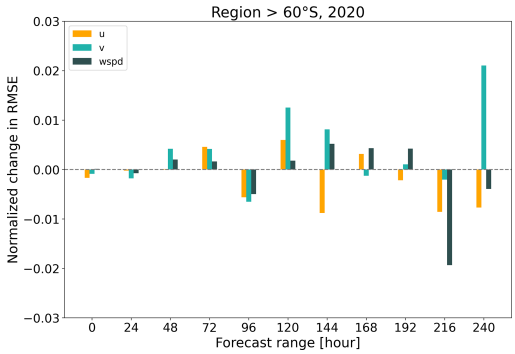

Figure 11. Normalized change in RMSE of the u and v components and wind speed (wspd) as a function of forecast range for the region $> 60°$ S for the year 2020. The ECMWF OSE forecasts with and without Aeolus are compared against weather station data.

ductions during the first half year than during the second half year for the high-latitude region in the NH, which suggests that the increasing random errors in Aeolus due to signal loss may degrade its impacts on wind forecasts at the surface level. With respect to the impact of different seasons, the results for the region $> 60°$ N show that Aeolus tends to have a more positive impact on wind forecasts during the winter months than during the summer months. This is partly attributed to the seasonal variation in solar background noise, which leads to larger random errors in Rayleigh-clear winds during summer months over polar regions and in the stratosphere (Reitebuch et al., 2022), thus resulting in larger forecast errors correspondingly. Another possible reason for the seasonal variation in error reduction is the different contributions of Aeolus data assimilation under different wind speed ranges. According to Fig. 7, more error reductions are found when wind speeds are greater than 6 m s^{-1} for the region $> 60°$ N. Thus, during the stormy season, which is usu-

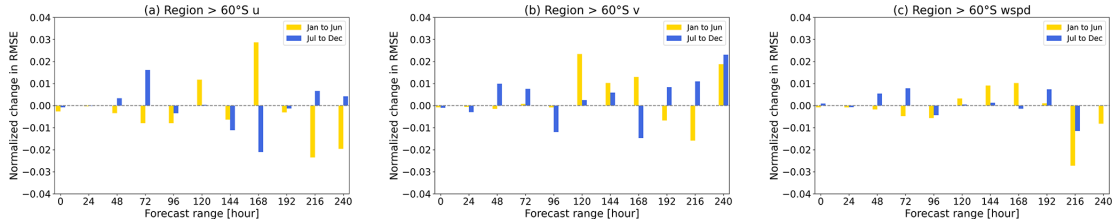

Figure 12. Normalized change in RMSE of the u and v components as a function of forecast range for 2 different half years of 2020 for the region > 60° S. The ECMWF OSE forecasts with and without Aeolus are compared against weather station data.

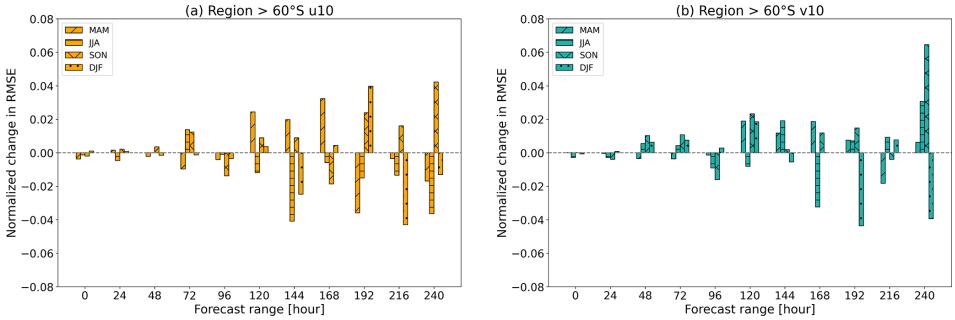

Figure 13. Seasonal variation in normalized change in RMSE of the u and v components as a function of forecast range for the region > 60° S for the year 2020. The ECMWF OSE forecasts with and without Aeolus are compared against weather station data. MAM: March, April and May; JJA: June, July and August; SON: September, October and November; DJF: December, January and February.

ally the wintertime for the high-latitude regions, there could be more evident error reductions.

Different from the results for the high-latitude region in the NH, Aeolus winds seem to have a limited impact on improving wind forecasts for the region > 60° S. This may be due to the poor spatial coverage of weather stations in Antarctica. Apart from this, the model may perform differently when applied to the region > 60° S due to the coarse model resolution in representing ice sheets and mountainous terrain in Antarctica (Bromwich et al., 2005), which could impair the contribution of Aeolus to surface wind forecasts.

In this study, the normalized change in the RMSEs between the control experiment and the experiment with Aeolus is not statistically significant at a significance level of 0.05 for many cases and forecast steps. We consider this in part to be due to the limited number of buoys and weather stations distributed over the study regions. Another possible reason could be the representativeness of the point-based measurements compared to the coarse model resolution, which makes the errors between in situ measurements and model outputs large and random.

In terms of the evaluation method, apart from the conventional inter-comparison analysis like what we used in this study, triple collocation (TC) analysis is another beneficial method for environmental parameter evaluation when there are three independent data sets (Stoffelen, 1998; Vogelzang and Stoffelen, 2012). Different from the inter-comparison analysis that regards a reference data set free of errors, TC analysis assumes that each data set is linearly correlated with the truth. Following the equation derivation documented in Vogelzang and Stoffelen (2012), the primary output of TC is the error standard deviation (ESD) of each data set, which allows us to compare the quality of different data sets. We made an attempt to implement the TC method in our cases (results are not shown). The results can generally reflect the impact of Aeolus on wind forecasts, with the ESD from the forecast with Aeolus lower than the one without Aeolus, implying a positive impact of Aeolus. But the ESD values may be inaccurate since the errors in the two forecasts are not fully independent because they are from the same NWP model. Theoretically, not taking this dependence into account may lead to the ESDs of two forecasts being underestimated and the ESD of in situ measurements overestimated since the error covariances of the two forecasts are greater than zero (Caires and Sterl, 2003). Therefore, to obtain accurate results when implementing the TC method to assess two correlated data sets, quantifying the non-zero covariance or making a further modification to the method may be required.

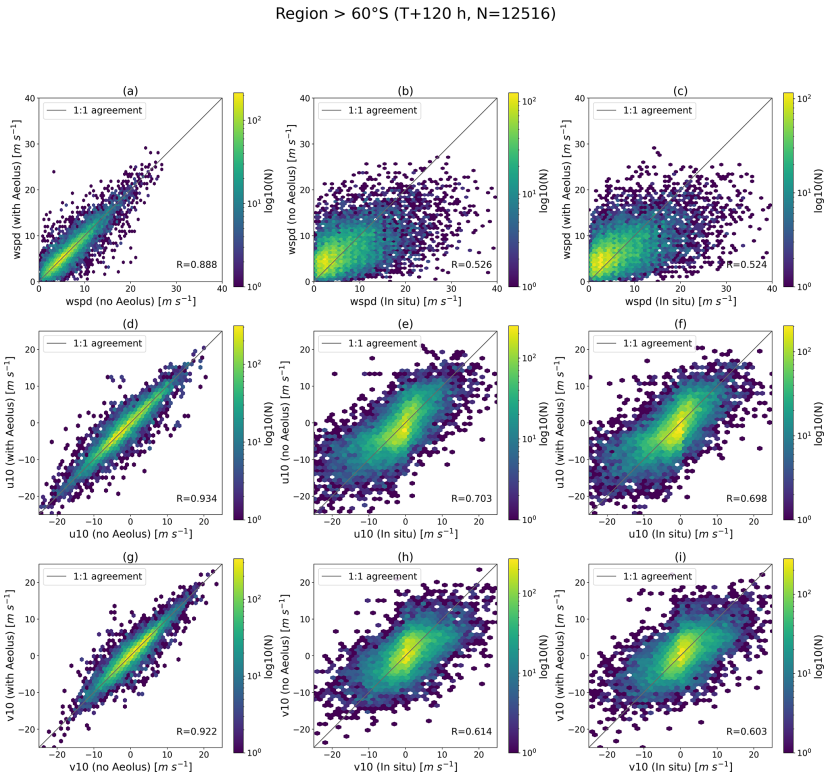

Figure 14. Hexagonal binning plots of the u and v components and wind speed at +120 h forecast for the region > 60° S for the year 2020 based on the ECMWF OSE forecasts with and without Aeolus and weather station data. The colour of each hexagon indicates the number of samples in it.

6 Conclusions

With the help of in situ measurements, the contribution of Aeolus wind assimilation to near-surface wind forecasts was assessed for tropical oceans (between 30° N and 30° S) and high-latitude regions (> 60° N and > 60° S) through both inter-comparison analysis and correlation analysis. The wind predictions come from the high-resolution $T_{co}639$ OSEs with the ECMWF model.

The results indicate that Aeolus wind assimilation has a limited impact on the sea surface wind forecasts for the tropical oceans, however, which requires further demonstration with more data samples. For the high-latitude region in the NH, error reductions are observed for many forecast steps, and this positive impact becomes more evident with extended forecasts. Moreover, more error reductions are found during the first half year of 2020 and during the winter months owing to the better behaviour of Aeolus and its greater contribution to the moderate to strong wind forecasts. Furthermore, the v wind component is likely to benefit more from Aeolus data assimilation than the u component for the region > 60° N. Unlike the NH, the contribution of Aeolus to the region > 60° S is not obvious, and further investigation with more in situ measurements is required. Correlation analysis also reflects the influence of Aeolus on surface wind forecasts to some extent.

Notwithstanding the limited spatial coverage of the reference data, the research findings of this study provide information on the role of Aeolus data assimilation with the ECMWF model in near-surface wind forecasts over the tropical ocean and the high-latitude regions.

Data availability. The OSEs were conducted by Michael Rennie and Lars Isaksen from the ECMWF, and the u and v wind components were extracted from MARS (https://www.ecmwf.int/en/forecasts/dataset/ecmwf-research-experiments, login required; ECMWF Research Department, 2022). The buoy measurements were obtained from the Global Tropical Moored Buoy Array (https://www.pmel.noaa.gov/tao/drupal/disdel/, last access: 4 August 2022; Pacific Marine Environmental Labora-

tory, 2022). Wind information at weather stations is accessed via Integrated Surface Database (https://www.ncei.noaa.gov/products/land-based-station/integrated-surface-database#:~:text=GlobalClimateStationSummariesSummariesaresimpleindicators,orlongertimeperiodsorforcustomizedperiods, last access: 11 August 2022; National Centers for Environmental Information, 2022).

Author contributions. HZ obtained the data, performed the data analysis and drafted the manuscript. CBH helped in interpreting the research findings. HZ revised the manuscript critically.

Competing interests. The contact author has declared that neither of the authors has any competing interests.

Disclaimer. Publisher's note: Copernicus Publications remains neutral with regard to jurisdictional claims in published maps and institutional affiliations.

Acknowledgements. We would like to thank the Royal Netherlands Meteorological Institute (KNMI) for being the secondment host institution. Our special appreciation goes to Ad Stoffelen from KNMI, who gave us the idea to conduct this study, and to Gert-Jan Marseille from KNMI for his assistance with OSE data retrieval. We would also like to show our gratitude to Michael Rennie and Lars Isaksen from the ECMWF for conducting the OSEs and MARS for data access. We thank the National Oceanic and Atmospheric Administration Pacific Marine Environmental Laboratory for buoy data and the National Centers for Environmental Information for wind measurements at weather stations.

Financial support. This study is a part of the Marie Skłodowska-Curie Actions Innovation Training Network: Lidar Knowledge Europe (LIKE), supported by the European Union's Horizon 2020 research and innovation programme (grant no. 858358). The Otto Mønsted Foundation supported half of the expenses for the secondment at KNMI.

Review statement. This paper was edited by Markus Rapp and reviewed by two anonymous referees.

References

Andersson, E., Dabas, A., Endemann, M., Ingmann, P., Källén, E., Offiler, D., and Stoffelen, A.: ADM-Aeolus Science Report, SP-1311, ESA, 121 pp., https://esamultimedia.esa.int/multimedia/publications/SP-1311/SP-1311.pdf (last access: 2 September 2022), 2008.

Banyard, T. P., Wright, C. J., Hindley, N. P., Halloran, G., Krisch, I., Kaifler, B., and Hoffmann, L.: Atmospheric Gravity Waves in Aeolus Wind Lidar Observations, Geophys. Res. Lett., 48, e2021GL092756, https://doi.org/10.1029/2021GL092756, 2021.

Belova, E., Kirkwood, S., Voelger, P., Chatterjee, S., Satheesan, K., Hagelin, S., Lindskog, M., and Körnich, H.: Validation of Aeolus winds using ground-based radars in Antarctica and in northern Sweden, Atmos. Meas. Tech., 14, 5415–5428, https://doi.org/10.5194/amt-14-5415-2021, 2021.

Bidlot, J.-R., Holmes, D. J., Wittmann, P. A., Lalbeharry, R., and Chen, H. S.: Intercomparison of the Performance of Operational Ocean Wave Forecasting Systems with Buoy Data, Weather Forecast., 17, 287–310, https://doi.org/10.1175/1520-0434(2002)017<0287:IOTPOO>2.0.CO;2, 2002.

Bromwich, D. H., Monaghan, A. J., Manning, K. W., and Powers, J. G.: Real-Time Forecasting for the Antarctic: An Evaluation of the Antarctic Mesoscale Prediction System (AMPS), Mon. Weather Rev., 133, 579–603, https://doi.org/10.1175/MWR-2881.1, 2005.

Charlton, A. J., O'neill, A., Lahoz, W. A., and Massacand, A. C.: Sensitivity of tropospheric forecasts to stratospheric initial conditions, Q. J. Roy. Meteor. Soc., 130, 1771–1792, https://doi.org/10.1256/qj.03.167, 2004.

Christiansen, B.: Downward propagation of zonal mean zonal wind anomalies from the stratosphere to the troposphere: Model and reanalysis, J. Geophys. Res., 106, 27307–27322, https://doi.org/10.1029/2000JD000214, 2001.

Caires, S. and Sterl, A.: Validation of ocean wind and wave data using triple collocation, J. Geophys. Res., 108, 3098, https://doi.org/10.1029/2002JC001491, 2003.

Cress, A., Martin, A., Born, M., and Weismann, M.: Impact of Aeolus HLOS winds in the global NWP System of DWD, Towards an operational Doppler Wind Lidar Programme, Darmstadt, Germany, 8–9 September 2022, EUMETSAT, https://www.eventsforce.net/eumetsat/frontend/reg/tAgendaWebsite.csp?pageID=15588&ef_sel_menu=247&eventID=38&mode= (last access: 1 November 2022), 2022.

Data Innovation and Science Cluster (DISC): Summary of Quality of Aeolus Data Products from 1st Reprocessing Campaign covering June to December 2019, ESA, https://earth.esa.int/eogateway/documents/20142/0/Aeolus-Summary-Reprocessing-1-DISC.pdf (last access: 2 November 2022), 2020.

ECMWF: Fact sheet: Earth system data assimilation, ECMWF, https://www.ecmwf.int/sites/default/files/medialibrary/2020-05/ecmwf-fact-sheet-data-assimilation.pdf (last access: 10 November 2022), 2020.

ECMWF Research Department: ECMWF Research Experiments (RD), ECMWF [data set], https://www.ecmwf.int/en/forecasts/dataset/ecmwf-research-experiments, last access: 28 July 2022.

Forsythe, M. and Halloran, G.: Impact of Aeolus Doppler Wind Lidar at the UK Met Office, Towards an operational Doppler Wind Lidar Programme, Darmstadt, Germany, 8–9 September 2022, EUMETSAT, https://www.eventsforce.net/eumetsat/frontend/reg/tAgendaWebsite.csp?pageID=15588&ef_sel_menu=247&eventID=38&mode= (last access: 1 November 2022), 2022.

Garrett, K., Liu, H., Ide, K., Hoffman, R. N., and Lukens, K. E.: Optimization and impact assessment of Aeolus HLOS wind assimilation in NOAA's global forecast system, Q. J. Roy. Meteor. Soc., 148, 2703–2716, https://doi.org/10.1002/qj.4331, 2022.

Hagelin, S., Azad, R., Lindskog, M., Schyberg, H., and Körnich, H.: Evaluating the use of Aeolus satellite observa-

tions in the regional numerical weather prediction (NWP) model Harmonie–Arome, Atmos. Meas. Tech., 14, 5925–5938, https://doi.org/10.5194/amt-14-5925-2021, 2021.

Iwai, H., Aoki, M., Oshiro, M., and Ishii, S.: Validation of Aeolus Level 2B wind products using wind profilers, ground-based Doppler wind lidars, and radiosondes in Japan, Atmos. Meas. Tech., 14, 7255–7275, https://doi.org/10.5194/amt-14-7255-2021, 2021.

King, G. P., Portabella, M., Lin, W., and Stoffelen, A.: Correlating Extremes in Wind Divergence with Extremes in Rain over the Tropical Atlantic, Remote Sensing, 14, 1147, https://doi.org/10.3390/rs14051147, 2022.

Kodera, K., Yamazaki, K., Chiba, M., and Shibata, K.: Downward propagation of upper stratospheric mean zonal wind perturbation to the troposphere, Geophys. Res. Lett., 17, 1263–1266, https://doi.org/10.1029/GL017i009p01263, 1990.

Laroche, S. and St-James, J.: Impact of the Aeolus Level-2B horizontal line-of-sight winds in the Environment and Climate Change Canada global forecast system, Q. J. Roy. Meteor. Soc., 148, 2047–2062, https://doi.org/10.1002/qj.4300, 2022.

Met Office: Beaufort wind force scale, Met Office, https://www.metoffice.gov.uk/weather/guides/coast-and-sea/beaufort-scale, last access: 24 February 2023.

Mile, M., Azad, R., and Marseille, G.-J.: Assimilation of Aeolus Rayleigh-Clear Winds Using a Footprint Operator in AROME-Arctic Mesoscale Model, Geophys. Res. Lett., 49, e2021GL097615, https://doi.org/10.1029/2021GL097615, 2022.

National Centers for Environmental Information (NCEI): Integrated Surface Database (ISD), NCEI, National Oceanic and Atmospheric Administration, https://www.ncei.noaa.gov/products/land-based-station/integrated-surface-database#:~:text=Global%20Climate%20Station%20Summaries%20Summaries%20are%20simple%20indicators,or%20longer%20time%20periods%20or%20for%20customized%20periods, last access: 11 August 2022.

Pacific Marine Environmental Laboratory (PMEL): Global Tropical Moored Buoy Array, National Oceanic and Atmospheric Administration, PMEL, National Oceanic and Atmospheric Administration, https://www.pmel.noaa.gov/tao/drupal/disdel/, last access: 4 August 2022.

Parrington, M., Rennie, M., Inness, A., and Duncan, D.: Monitoring the atmospheric impacts of the Hunga-Tonga eruption, ECMWF, https://www.ecmwf.int/en/newsletter/171/news/monitoring-atmospheric-impacts-hunga-tonga-eruption (last access: 2 November 2022), 2022.

Pourret, V., Šavli, M., Mahfouf, J., Raspaud, D., Doerenbecher, A., Bénichou, H., and Payan, C.: Operational assimilation of Aeolus winds in the Météo-France global NWP model ARPEGE, Q. J. Roy. Meteor. Soc., 148, 2652–2671, https://doi.org/10.1002/qj.4329, 2022.

Reitebuch, O., Krisch, I., Lemmerz, C., Lux, O., Marksteiner, U., Masoumzadeh, N., Weiler, F., Witschas, B., Filomarino, V. C., Meringer, M., Schmidt, K., Huber, D., Nikolaus, I., Fabre, F., Vaughan, M., Reissig, K., Dabas, A., Flament, T., Lacour, A., Mahfouf, J.-F., Seck, I., Trapon, D., Abdalla, S., Isaksen, L., Rennie, M., Benedetti, A., McLean, W., Henry, K., Donovan, D., de Kloe, J., Marseille, G.-J., Stoffelen, A., Wang, P., van Zadelhoff, G.-J., Perron, G., Jupin-Langlois, S., Pijnacker-Hordijk, B., Veneziani, M., Bucci, S., Gostinicchi, G., Di Ciolo, L., Bley, S., Geiss, A., Kanitz, T., Straume, A.-G., Wernham, D., Krisna, T., von Bismarck, J., Colangeli, G., Trivigno, V., Romanazzo, M., Aprile, S., and Parrinello, T.: Contributions from the DISC to accomplish the Aeolus mission objectives, Aeolus 3rd Anniversary Conference, Taormina, Italy, 23–27 March 2022, https://elib.dlr.de/186034/ (last access: 20 October 2022), 2022.

Rennie, M. and Isaksen, L.: The NWP impact of Aeolus Level-2B winds at ECMWF, ECMWF, 265 pp., https://confluence.ecmwf.int/display/AEOL/L2B+team+technical+reports+and+relevant+papers?preview=/46596815/348788257/AED-TN-ECMWF-NWP-025--20230809_v7.0.pdf (last access: 17 August 2023), 2023.

Rennie, M. P., Isaksen, L., Weiler, F., de Kloe, J., Kanitz, T., and Reitebuch, O.: The impact of Aeolus wind retrievals on ECMWF global weather forecasts, Q. J. Roy. Meteor. Soc., 147, 3555–3586, https://doi.org/10.1002/qj.4142, 2021.

Sandu, I., Bechtold, P., Nuijens, L., Beljaars, A., and Brown, A.: On the causes of systematic forecast biases in near-surface wind direction over the oceans, ECMWF, 21 pp., https://www.ecmwf.int/sites/default/files/elibrary/2020/19545-causes-systematic-forecast-biases-near-surface-wind-direction-over-oceans.pdf (last access: 22 February 2023), 2020.

Stoffelen, A.: Toward the true near-surface wind speed: Error modeling and calibration using triple collocation, J. Geophys. Res., 103, 7755–7766, https://doi.org/10.1029/97JC03180, 1998.

Straume-Lindner, A. G., Parrinello, T., Von Bismarck, J., Bley, S., Wernham, D., Kanitz, T., Alvarez, E., Fischey, P., De Laurentis, M., Fehr, T., Ehlers, F., Duc Tran, V., Krisch, I., Reitebuch, O., and Renni, M.: ESA'S Wind Mission Aeolus - Overview, Status and Outlook, in: 2021 IEEE International Geoscience and Remote Sensing Symposium IGARSS, IGARSS 2021 - 2021 IEEE International Geoscience and Remote Sensing Symposium, Brussels, Belgium, 12–16 July 2021, IEEE, 755–758, https://doi.org/10.1109/IGARSS47720.2021.9554007, 2021.

Tripathi, O. P., Baldwin, M., Charlton-Perez, A., Charron, M., Eckermann, S. D., Gerber, E., Harrison, R. G., Jackson, D. R., Kim, B., Kuroda, Y., Lang, A., Mahmood, S., Mizuta, R., Roff, G., Sigmond, M., and Son, S.: The predictability of the extratropical stratosphere on monthly time-scales and its impact on the skill of tropospheric forecasts, Q. J. Roy. Meteor. Soc., 141, 987–1003, https://doi.org/10.1002/qj.2432, 2015.

Vogelzang, J. and Stoffelen, A.: Triple collocation, Royal Netherlands Meteorological Institute, 22 pp., https://cdn.knmi.nl/system/data_center_publications/files/000/068/914/original/triplecollocation_nwpsaf_tr_kn_021_v1.0.pdf?1495621500 (last access: 27 January 2022), 2012.

Witschas, B., Lemmerz, C., Geiß, A., Lux, O., Marksteiner, U., Rahm, S., Reitebuch, O., Schäfler, A., and Weiler, F.: Validation of the Aeolus L2B wind product with airborne wind lidar measurements in the polar North Atlantic region and in the tropics, Atmos. Meas. Tech., 15, 7049–7070, https://doi.org/10.5194/amt-15-7049-2022, 2022.

Zuo, H., Hasager, C. B., Karagali, I., Stoffelen, A., Marseille, G.-J., and de Kloe, J.: Evaluation of Aeolus L2B wind product with wind profiling radar measurements and numerical weather prediction model equivalents over Australia, Atmos. Meas. Tech., 15, 4107–4124, https://doi.org/10.5194/amt-15-4107-2022, 2022.

A.3 Article III: The Contribution of Aeolus Wind Observations to ECMWF Sea Surface Wind Forecasts

Zuo, H., Stoffelen, A., Rennie, M., & Hasager, C. B. (2023). *The Contribution of Aeolus Wind Observations to ECMWF Sea Surface Wind Forecasts* [Manuscript submitted for publication]

Article III has been submitted to the Journal of Geophysical Research: Atmospheres for publication and is currently in revision.

The Contribution of Aeolus Wind Observations to ECMWF Sea Surface Wind Forecasts

Haichen Zuo[1], Ad Stoffelen[2], Michael Rennie[3], and Charlotte Bay Hasager[1]

[1]Technical University of Denmark, Roskilde, Denmark, [2]The Royal Netherlands Meteorological Institute, De Bilt, The Netherlands, [3]European Centre for Medium-Range Weather Forecasts, Reading, UK.

Corresponding author: Haichen Zuo (hazu@dtu.dk)

Key Points:

- Aeolus is able to slightly improve the short-range sea surface wind forecasts for global oceans except for the tropics.
- Aeolus can generally reduce zonal biases of short-range forecasts, while the impact on meridional biases is mixed.
- As forecast step extends, the positive impact of Aeolus becomes more evident, especially for Southern Hemisphere extratropical ocean regions.

Abstract

Aeolus is the first satellite mission focusing on wind profile detection on a global scale. This study evaluates the contribution of Aeolus winds to sea surface wind forecasts by further analyzing the Observing System Experiments (OSE) from the European Centre for Medium-Range Weather Forecasts (ECMWF) with scatterometer winds. We find that Aeolus has the potential to reduce the short-range forecast errors at the global scale, for the ocean regions in the Northern Hemisphere (>20°N) and in the Southern Hemisphere (>20°S). Also, Aeolus can generally reduce zonal biases, while the impact on meridional biases is mixed. In addition, as the forecast step extends, the positive impact becomes more significant, especially for the extratropical ocean regions in the Southern Hemisphere.

Plain Language Summary

Wind information plays a vital role in understanding atmosphere dynamics and improving weather forecasts. Aeolus is the first satellite to detect global wind profiles from the surface to about 30 km in height. These wind profiles can be used to assist in Numerical Weather Prediction (NWP). In this study, we investigate whether the Aeolus winds can benefit the sea surface wind forecasts in the global NWP model at ECMWF by exploiting satellite-observed ocean winds. The finding is that Aeolus can slightly reduce the departure between forecasts and observations for wind vectors over most ocean regions, especially in the Southern Hemisphere as the forecast step extends up to day-5. In addition, Aeolus can generally reduce the short-range forecast biases of zonal winds, while only in the Northern Hemisphere extratropics are meridional biases beneficially influenced on average.

1 Introduction

Wind profile information is essential in understanding atmospheric dynamics and in improving Numerical Weather Prediction (NWP). However, one of the major deficiencies in the Global Observing System is the lack of distributed wind profile measurements, especially over the oceans, in the tropics and the Southern Hemisphere (SH) (Stoffelen et al., 2020; World Meteorological Organization (WMO), 2020). To begin to fill this gap, in August 2018, the European Space Agency (ESA) launched the Aeolus satellite that carries a direct-detection Doppler Wind Lidar (DWL) and is able to characterize global wind profiles from the surface to about 30 km in height. The satellite follows a sun-synchronous polar orbit with the descending node at 06:00 local time (LT) and the ascending node at 18:00 LT. The wind information acquired by Aeolus are approximately east-west oriented horizontal line-of-sight (HLOS) wind components. Since the emitted laser light is scattered back both from air molecules (i.e. Rayleigh scattering) and particles, such as aerosol, cloud droplets and ice crystals, in the atmosphere (i.e. Mie scattering), the DWL has two detection channels, a Rayleigh channel and a Mie channel. Correspondingly, the two main commonly used wind types are Rayleigh-clear winds and Mie-cloudy winds (Andersson et al., 2008). Aeolus is equipped with two redundant laser transmitters that are flight model A (FM-A) and flight model B (FM-B). The mission initially operated with FM-A, but due to the unexpected degrading laser pulse energy, it switched to FM-B in June 2019 and then switched back to FM-A in late-2022 (ESA, 2022; Lux et al., 2021). The nominal Aeolus mission operations ended in April 2023.

Following the successful launch, extensive calibration and validation works have been carried out, and the data processing algorithm has been continually improved. The data quality verification based on observation minus model background wind, o-b, departures for the second reprocessed data set (2B11 - Level 2 Baseline 11) at the European Centre for Medium-Range Weather Forecasts (ECMWF) shows that the biases are close to zero for both Rayleigh-clear and Mie-cloudy winds from June 2019 to October 2020. However, due to the unexpected signal loss of the Aeolus DWL after the launch (Straume-Lindner et al., 2021), the estimated random errors of Rayleigh-clear winds suffered a more than 100% increase, rising from ~2 m/s to ~5 m/s, while Mie-cloudy winds are rather insensitive to this instrument problem with stable random errors of ~3.5 m/s (Rennie & Isaksen, 2022). The validations worldwide by comparing to wind observations show similar results for the products after baseline 10 with the M1-temperature-based bias correction and daily updates of bias removal (Aeolus Data Innovation and Science Cluster (DISC), 2020; Belova et al., 2021; Iwai et al., 2021; Ratynski et al., 2023; Witschas et al., 2022; Zuo et al., 2022). The biases are commonly smaller than 0.7 m/s for both Rayleigh-clear winds and Mie-cloudy winds, despite some special cases (e.g., polar regions), which achieves the mission requirements; the random errors mainly range from 4 m/s to 8 m/s for Rayleigh-clear winds and from 2.0 m/s to 5 m/s for Mie-cloudy winds, most of which are much larger than the precision of the mission requirements (Ingmann & Straume, 2016).

Despite the unforeseen signal loss and lower precision, Aeolus winds have been assimilated into the ECWMF model through 4D-var data assimilation to improve operational weather forecasts (Rennie & Isaksen, 2020). To assess the added value of Aeolus observations to NWP, many institutions have carried out Observing System Experiments (OSEs) with their global NWP models, including ECMWF, National Oceanic and Atmospheric Administration (NOAA), Deutscher Wetterdienst (DWD), Météo-France, Environment and Climate Change Canada, Korean Integrated Model (KIM), etc. (Borne et al., 2023; Garrett et al., 2022; Laroche & St-James, 2022; Lee et al., 2023; Pourret et al., 2022; Rennie & Isaksen, 2022). The evaluations demonstrated that with Aeolus data assimilation, the wind vector forecasts are improved by up to 4%, particularly in the upper troposphere and/or lower stratosphere over the tropics and polar regions (Garrett et al., 2022; Laroche & St-James, 2022; Pourret et al., 2022; Rennie & Isaksen, 2022). In addition, Aeolus benefits forecasts for weather and climate events, such as for tropical cyclones' tracks in the Eastern Pacific basin and Atlantic basin, West African Monsoon circulation, and volcanic ash plume dispersion (Amiridis et al., 2023; Borne et al., 2023; Garrett et al., 2022).

However, to the best of our knowledge, none of the existing evaluations goes into depth on sea surface wind forecasts that highly affect our offshore activities and challenge the model performance. Noting the DWL signal loss, lower quality and less Rayleigh and Mie winds will emerge from the lower troposphere in particular, due to reduced signal penetration. Given its relevance, the purpose of this study is to assess the effects of Aeolus wind assimilation on sea surface wind forecasts geographically by comparing with Advanced Scatterometer (ASCAT) winds and Haiyang-2B Scatterometer (HSCAT) winds. By segregating different climate regions

on a global map, we may infer in which regions Aeolus brings improvement and in which regions Aeolus degrades the forecasts in the Marine Atmospheric Boundary Layer (MABL).

Winds slow down substantially in the MABL due to surface friction, where surface drag and the dissipation of momentum are parameterized in atmospheric models, as well as the associated exchanges of momentum, heat and moisture. In addition, processes of moist convection are not well resolved and are dependent on parameterizations. Substantial biases in NWP models have been reported in surface winds and surface wind gradients, such as divergence and curl (Belmonte Rivas & Stoffelen, 2019). Scatterometer vector winds have been well characterized and shown to have low biases against the global moored buoys, with wind component errors of about 0.5 m/s (Vogelzang & Stoffelen, 2021). Hence, scatterometer winds are well suited to geographically investigate the impact of Aeolus winds in the MABL in terms of model biases and random error. It will provide information on the consistency of improvements in the upper air winds and the MABL in different weather regimes.

Sections 2 and 3 introduce the data and methods used in this study. Section 4 presents the main research findings together with corresponding discussions. The final section provides a short summary of the study and its conclusions.

2 Data

2.1 ECMWF OSEs

This assessment is based on the ECMWF OSEs, which include a control experiment without Aeolus data assimilation (NoAeolus) and an experiment with the 2nd reprocessed Aeolus L2B baseline 11 data (Aeolus), assimilated during the FM-B period (Rennie and Isaksen, 2022). The applied model version is CY47R2 with an atmosphere outer loop resolution of T_{co} 639, which is around 18 km in grid size. Both Rayleigh-clear and Mie-cloudy winds were assimilated into the model through the four-dimensional variational (4D-Var) data assimilation technique with a 12-hour assimilation window. Observations from nominally operational satellites and conventional sources were also assimilated for the two model runs. For the lower troposphere (> 850 hPa), only Mie-cloudy winds with an estimated error smaller than 5 m/s were assimilated into the model. Detailed information on quality control decisions for the OSEs is documented in Rennie and Isaksen (2022). Figure 1 illustrates the geographical distribution of the averaged number of L2B Mie-cloudy winds assimilated per cycle below 850 hPa. Most Mie-cloudy winds were assimilated over the low-to-mid latitude ocean regions except for the convergence zones.

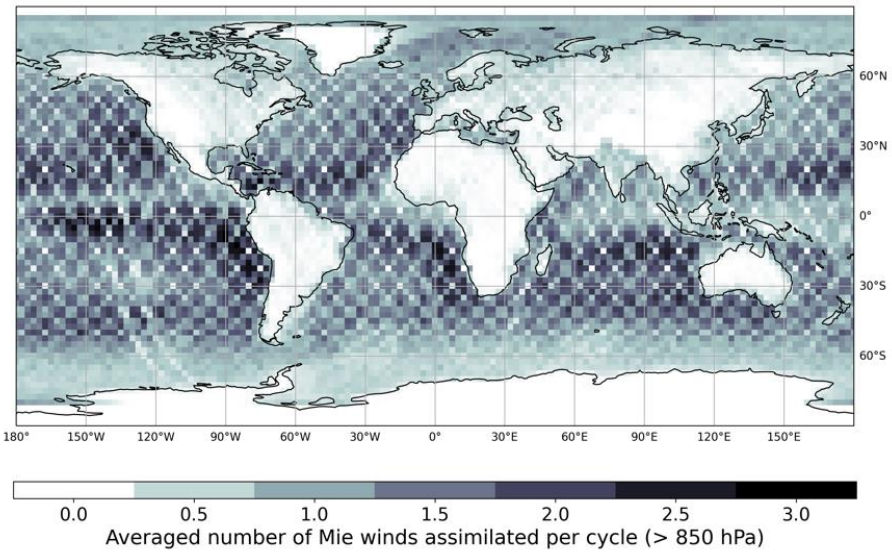

Figure 1. Geographical distribution of the averaged number of Mie-cloudy winds assimilated into the ECMWF OSE per cycle below 850 hPa in the Aeolus experiment.

The first-guess departure (o-b) of u and v components with ASCAT winds as reference were obtained for short-term forecast quality evaluation. Furthermore, 5-day forecasts of u and v components at 10 m height with a 24 h time interval were extracted for a medium-range forecast quality assessment. The above-mentioned OSE data were obtained via the ECMWF Meteorological Archival and Retrieval System (MARS) (ECMWF Research Department, 2022). The study period is one year from July 2019 to June 2020, during which Aeolus has the best data quality.

2.2 ASCAT winds

The Advanced Scatterometer (ASCAT) is a real-aperture radar carried on the series of Meteorological Operational (Metop) satellites, including Metop-A, Metop-B and Metop-C. The satellites follow a sun-synchronous orbit with 9:30 LT (21:30 LT) for descending node (ascending node). ASCAT operates at a C-Band frequency of 5.255 GHz, which makes the measurements unaffected by cloud cover and rain. The wind speed and direction are derived from the roughness of the sea by measuring the electromagnetic backscatter from ocean ripples, called gravity-capillary waves. There are two swath grid wind products, one at 25 km and one at 12.5 km. The wind speed bias of these two products is close to zero, and the Standard Deviations of wind component Error (SDE) is about 0.4 m/s for 25 km and 0.5 m/s for 12.5 km in the spatial representation of the scatterometer (Vogelzang & Stoffelen, 2021). In o-b statistics, when taking the Standard Deviation of Difference (SDD) with respect to ECMWF background winds, the SDD increases to about 1.4 m/s (Ocean and Sea Ice Satellite Application Facilities (OSI SAF)/ EUMETSAT Advanced Retransmission Service (EARS) Winds Team, 2021). In this study, we use the 25 km product as the reference data set (EUMETSAT OSI SAF, 2009).

2.3 HSCAT winds

Haiyang-2B (HY-2B), launched in 2018, is the second satellite of a series of marine dynamic environment satellites of China. It operates in a sun-synchronous orbit with a local time of descending (ascending) node at 6:00 LT (18:00 LT). Carrying a rotating pencil-beam scatterometer operating at the Ku-band frequency of 13.3 GHz, HY-2B is able to detect sea surface wind speed and direction within a single swath. The 25-km and 50-km swath grid products have a comparable bias of about 0.11 m/s when compared with the ECMWF background winds at 10-m height. The SDE of the wind components is about 0.6 m/s (Vogelzang & Stoffelen, 2021), where the o-b SDDs of the wind components are about 1.2 m/s for the 25 km products and about 1.1 m/s for the 50 km products (OSI SAF Winds Team, 2021). The higher SDE and lower SDD compared to ASCAT is due to the spatial processing and filtering of the pencil-beam scatterometer winds and the smoothness of the ECMWF model winds. To be most consistent with the ASCAT resolution, we use the 25-km swath grid product as a validation data set (EUMETSAT OSI SAF, 2021).

3 Methods

3.1 Wind vector interpolation and collocation

The short-range forecast assessment is based on the o-b departures, for which no wind vector interpolation and collocation are needed. Figure 2 displays the number of first-guess departure data samples in the 2.5°×2.5° grid boxes. Owing to the 12-hour assimilation window, the first-guess departure data has global coverage. To ensure the quality of assessment, the grid boxes with data sample numbers smaller than 25,000 have been removed since the ASCAT wind vector cells in those grids may be contaminated by land or sea ice.

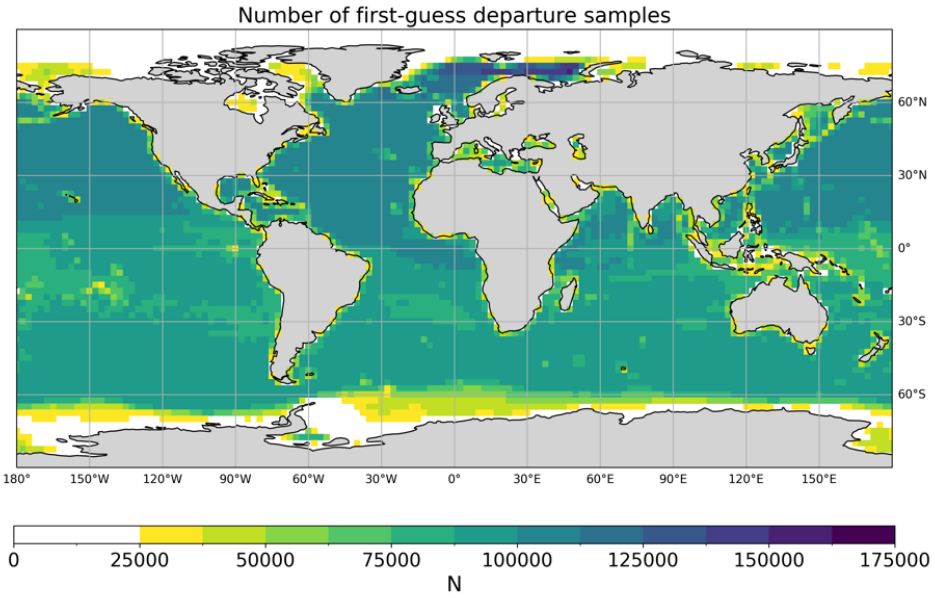

Figure 2. The number of first-guess departure (o-b) data samples in 2.5° × 2.5° grids.

For the medium-range forecast assessment, the two wind forecasts from the ECMWF OSE and the scatterometer winds need to be collocated first. The ASCAT Wind Data Processor (AWDP) software was employed for the wind vector interpolation of the two ECMWF forecasts to the ASCAT Wind Vector Cells (WVC) (EUMETSAT NWP SAF, 2020). For the assessment with HSCAT winds, the wind vector interpolation of the two forecasts from the ECMWF OSE was achieved by the Pencil Beam Wind Processor (PenWP) software (EUMETSAT NWP SAF, 2022). The collocation time window is ±30 mins of the forecast steps for both ASCAT and HSCAT winds.

After collocating with the forecasts at the time interval of 24 h, there are two bands available (Figure 3) since the satellites for scatterometer winds operate in sun-synchronous orbits. For the collocation with ASCAT winds, the data mainly cover the time zones of Coordinated Universal Time (UTC)+8, +9 and +10 and UTC-2, -3 and -4. For the collocation with HSCAT winds, the data samples are mainly over the time zones of UTC+5, +6 and +7 and UTC-5, -6 and -7. Note that due to the different LT of ASCAT and HSCAT, their evaluations are rather complementary. To ensure the quality of our analyses, we removed the grid boxes with data samples smaller than 50,000, as those grid boxes are usually close to polar regions or land. There are up to around 800,000 data samples available for the evaluation with ASCAT, owing to three Metop satellites operating during the study period. For the evaluation with HSCAT, the data samples for most grid boxes are between 200,000 and 400,000 since there is only one satellite available.

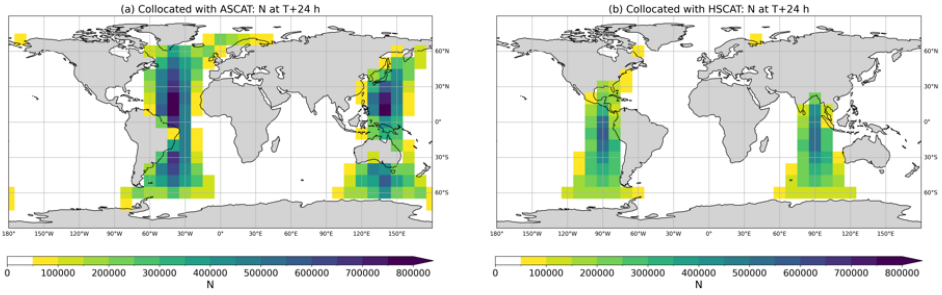

Figure 3. Available data regions after time collocating with (a) ASCAT winds and (b) HSCAT winds at the 24-hour forecast step. Grid boxes (10° × 10°) with data samples smaller than 50,000 have been removed as those grid boxes are mainly close to polar regions or land.

3.2 Statistical methods

To achieve the goal, we quantified the normalized change in root-mean-square difference (RMSD) for wind vector, u and v components geographically.

$$RMSD = \sqrt{\frac{\sum_{i=1}^{N}(o_i - b_i)^2}{N}} \quad (1)$$

$$RMSD_{vector\ wind} = \sqrt{RMSD_u^2 + RMSD_v^2} \quad (2)$$

$$NCRMSD = \frac{RMSD_{with\ Aeolus} - RMSD_{no\ Aeolus}}{RMSD_{no\ Aeolus}} \quad (3)$$

Where o_i are the observations and b_i are the forecasts.

In addition, the assessment is carried out for the Mean Bias Error (MBE) and the difference in MBE (DMBE) for u and v components, respectively.

$$MBE = \frac{\sum_{i=1}^{n}(o_i - b_i)}{N} \quad (4)$$

$$DMBE = MBE_{with\ Aeolus} - MBE_{no\ Aeolus} \quad (5)$$

The assessments, based on the observation feedback data, are for the global scale, tropical ocean regions (20°S – 20°N), and extratropical ocean regions in the Northern Hemisphere (>20°N) and Southern Hemisphere (>20°S). Furthermore, the assessment was also carried out for a medium-range forecast range until T+120 h with the time interval of 24 h by collocating with ASCAT and HSCAT wind products.

4 Results and Discussions

4.1 Short-range forecasts

Figure 4 shows the geographical distribution of the normalized change in RMSD based on the first-guess (o-b) departure. The statistics for each climatic region are summarized in Table 1. According to the maps in Figure 4, the RMSDs for wind vectors reduced by up to 3% for most regions, with a larger magnitude for the u component than the v component. A negative or neutral impact of Aeolus data assimilation is mainly found over the tropical regions of the east Pacific. Note that the vector data has improved sampling with respect to the u and v components and hence reduced noise.

According to Table 1, the overall impact of Aeolus on wind vector is small but statistically significant and positive at the global scale and for the extratropics in both hemispheres, while the impact on the tropical ocean regions is nearly neutral. This result is comparable to the verification by ECMWF (Rennie & Isaksen, 2022). A beneficial impact is furthermore found for both the u and v components. Assuming a typical wind component departure of 1.5 m/s, the SDE improvements appear typically 0.02 m/s except for the tropics, where forecast improvement is only obtained for the u component. This is probably partly because what Aeolus detects is almost the east-west wind component, except for the polar regions, according to its measurement geometry (Andersson et al., 2008), and the relative independence of u and v components in the tropics (e.g., Žagar et al., 2021).

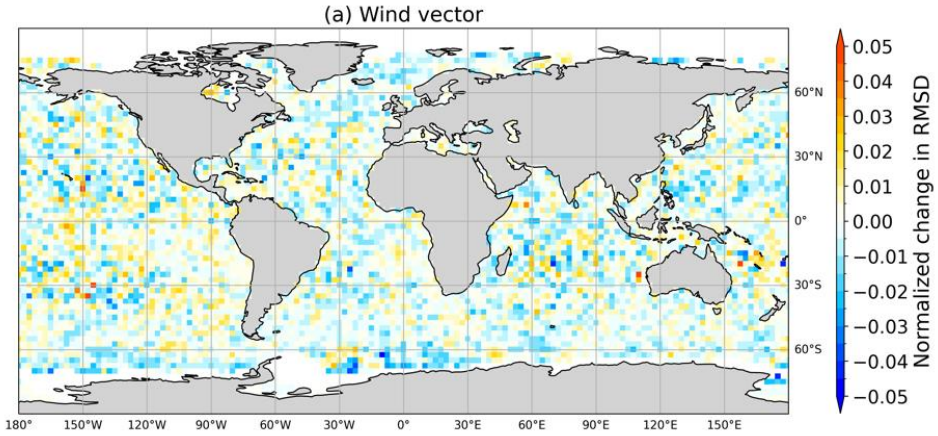
(a) Wind vector
60°N
30°N
0°
30°S
60°S
180°
150°W
120°W
90°W
60°W
30°W
0°
30°E
60°E
90°E
120°E
150°E
0.05
0.04
0.03
0.02
0.01
0.00
−0.01
−0.02
−0.03
−0.04
−0.05
Normalized change in RMSD

248

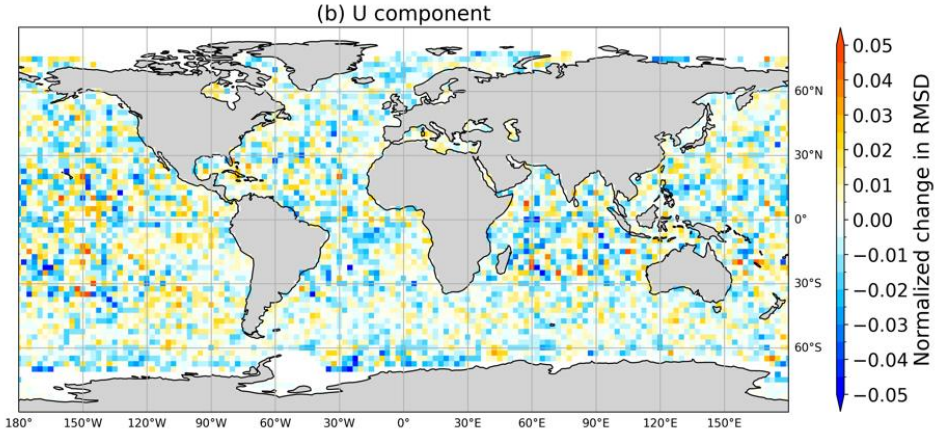
(b) U component
60°N
30°N
0°
30°S
60°S
180°
150°W
120°W
90°W
60°W
30°W
0°
30°E
60°E
90°E
120°E
150°E
0.05
0.04
0.03
0.02
0.01
0.00
−0.01
−0.02
−0.03
−0.04
−0.05
Normalized change in RMSD

249

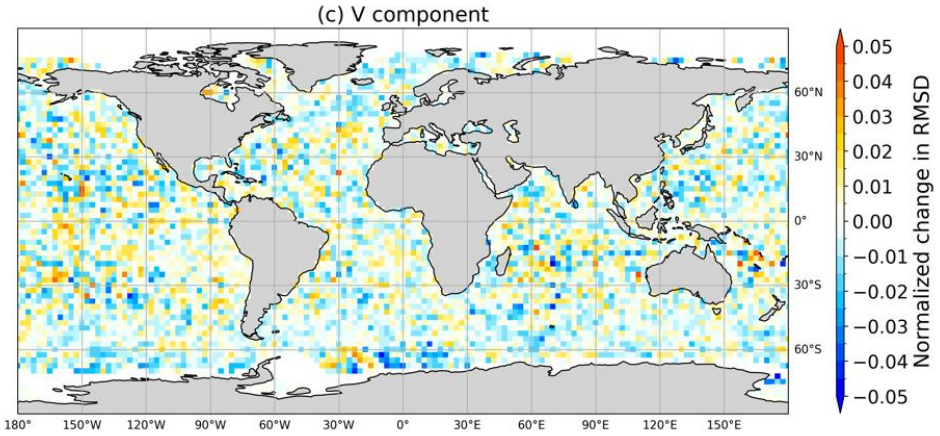

Figure 4. Normalized change in RMSD for (a) wind vector, (b) u component and (c) v component based on ASCAT wind first-guess departures. Negative values indicate a positive impact of Aeolus.

Table 1. Normalized change in RMSD for each climatic region. Negative values indicate a positive impact of Aeolus. The values in the square brackets are uncertainties at a 95% confidence interval. The star (*) marks a positive impact of Aeolus that is statistically significant.

Region	Wind vector	u component	v component
Global	-0.0011* [-0.0013, -0.0009]	-0.0013* [-0.0016, -0.0010]	-0.0009* [-0.0012, -0.0006]
NH (>20°N)	-0.0012* [-0.0017, -0.0008]	-0.0012* [-0.0017, -0.0006]	-0.0012* [-0.0018, -0.0007]
Tropics	-0.0004 [-0.0009, 0.0000]	-0.0013* [-0.0019, -0.0006]	0.0002 [-0.0004, 0.0007]
SH (>20°S)	-0.0015* [-0.0018, -0.0011]	-0.0014* [-0.0019, -0.0009]	-0.0016* [-0.0020, -0.0012]

Figure 5 shows the influence of Aeolus on bias correction. It can be seen that the u and v biases are generally negative for extratropical regions, while the u and v biases for tropics are positive and negative, respectively, as shown in Figure 5a and Figure 5b. According to Figure 5c and Figure 5d, Aeolus tends to make more westerly and southerly winds over the tropics and more easterly winds at around 60°S. However, though quite large scale, these changes (0.02 to 0.05 m/s) are an order of magnitude smaller as compared to the large model biases observed by scatterometers. On the other hand, the biases are typically the same size as the reduction of the SDD of o-b departures in the Aeolus experiment, suggesting that they are statistically significant. For example, the large-scale reduction in the SH tropics v (blue) coincides with positive biases in the NoAeolus experiment and hence helps to reduce bias.

Figure 6 shows the relationship between the bias changes and the model biases in the NoAeolus experiment for each climatic region. Corresponding to the maps in Figure 5, extratropical u and v

biases are generally negative, while tropical u and v biases are positive and negative, respectively. For the u component, most scatters are in quadrants II or IV, implying that the biases are slightly corrected with Aeolus wind assimilation. This is probably associated with the mainly zonal wind measurements of Aeolus. For the v component, it appears that the results are mixed especially for the tropics and the SH extratropics with scatters distributing more evenly at all quadrants compared to the u component. In summary, Aeolus generally improves zonal biases, while meridional biases are on average beneficially affected only in the NH extratropics.

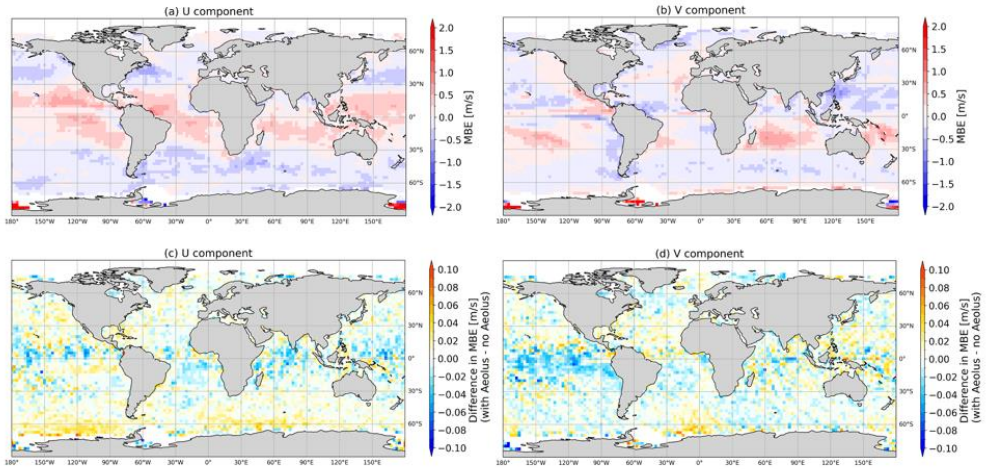

Figure 5. The MBE (a and b) and DMBE (c and d) for u and v components based on the first-guess departures (o-b) by taking ASCAT winds as the reference.

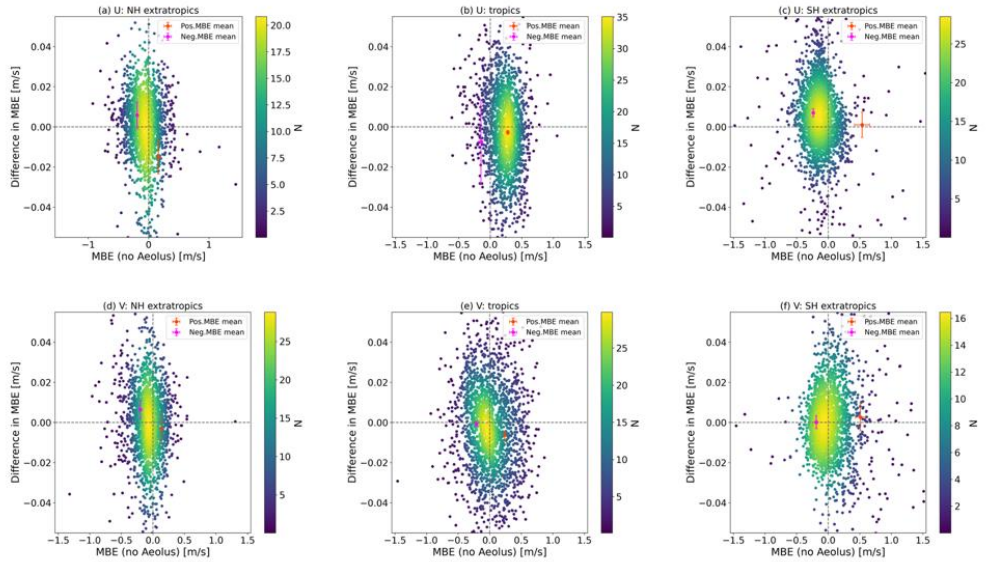

Figure 6. Scatter plots of the difference in MBE against the MBE in the NoAeolus experiment for u and v components for each climatic zone. Scatters in quadrants II and IV indicate bias reduction. The red and magenta points with error bars indicate the mean values for the positive and negative biases, respectively.

4.2 Medium-range forecasts

Figure 7 shows the distribution of the normalized change in RMSD at T+24 h, 48 h, 72 h, 96 h and 120 h forecast steps with ASCAT and HSCAT as references. With the forecast step extending, the impact of Aeolus data assimilation becomes more apparent, from 0.5% at T+24 h up to 4% at T+120 h. The positive impact is mainly found over the extratropical Atlantic Ocean and the ocean to the south of Australia up to the T+96 h forecast step when taking ASCAT as reference. When compared with HSCAT winds, the positive impact is mainly obtained for the Indian Ocean for the T+24 h and T+48 h. From the T+96 h forecast step, the southeast Pacific and the south Indian Ocean tend to benefit more from Aeolus.

Table 2 summerises the overall impact of Aeolus for medium-range forecasts. Regarding the verifications with ASCAT winds, the overall impact of Aeolus is significantly positive from T+24 h to T+96 h forecast steps. Moreover, significant improvement in wind vector forecasts is mainly obtained over the extratropical oceans in the SH until the T+96 h forecast step. The positive impact may be associated with Aeolus wind measurements in the upper atmosphere, which improve upper air analyses and benefit sea surface wind forecasts through downward propagation. The assessment based on HSCAT winds shows a significant reduction in RMSD only at T+120 h, mainly for the extratropics in the SH. The difference in the ASCAT and HSCAT verifications, and as a function of time, is probably due to the different weather regimes, where the model may have different performances. For the tropics, the impact of Aeolus is still limited, although Aeolus does correct background errors in the upper troposphere of the ITCZ (Rennie & Isaksen, 2022), it seems the sea surface wind forecasts do not benefit from it. Another noteworthy finding is that no statistically significant negative impact is found for both ASCAT and HSCAT evaluations. To summarize, Aeolus has the potential to benefit medium-range sea surface wind forecasts up to 120 h forecast step, especially for the SH extratropics.

Our study focuses on the forecasts up to the T+120 h step because the impact of Aeolus on the low-level atmosphere becomes very limited or neutral after day-5 according to the verifications against operational analysis at the ECMWF (Rennie & Isaksen, 2022).

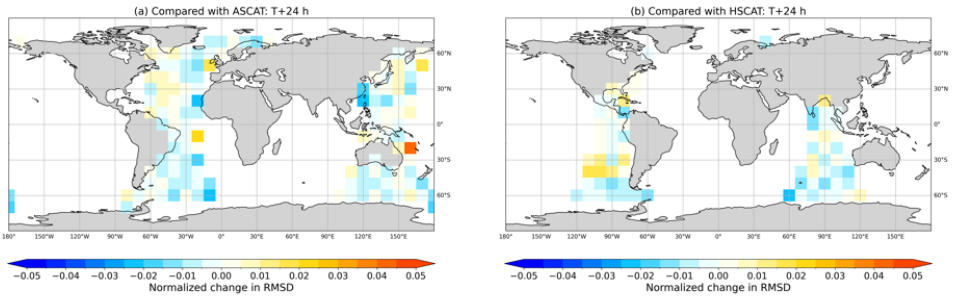

311

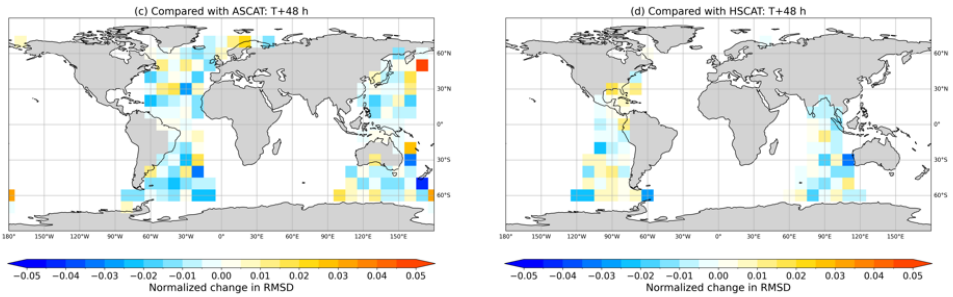

312

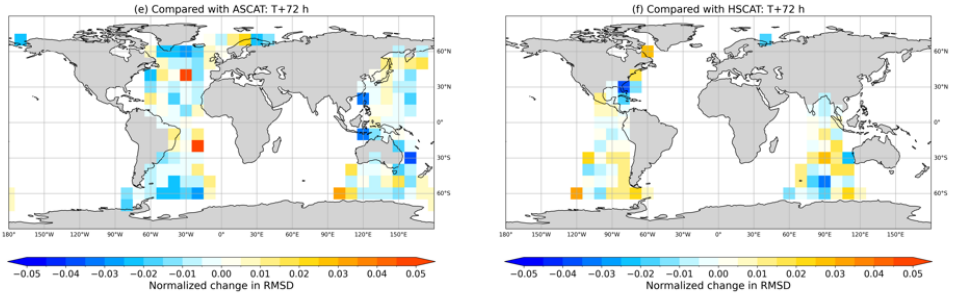

313

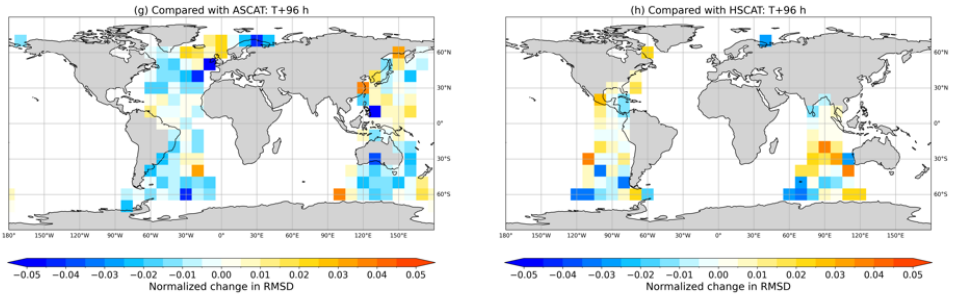

314

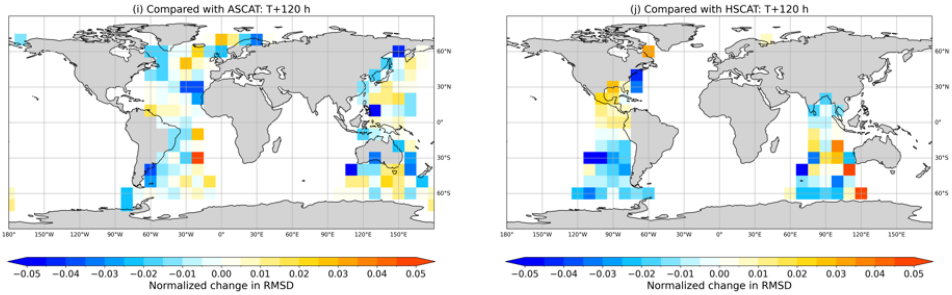

Figure 7. Normalized change in RMSD for wind vector by taking ASCAT and HSCAT as reference, respectively. Negative values indicate a positive impact of Aeolus.

Table 2. Normalized change in RMSD for each climatic region for the forecast steps from T+24 h to T+120 h. The values in the square brackets are uncertainties at a 95% confidence interval. The star (*) marks the statistically significant and positive impact of Aeolus with ASCAT and HSCAT as reference.

Reference	Region	T+24 h	T+48 h	T+72 h	T+96 h	T+120 h
ASCAT	All	-0.0018* [-0.0033,-0.0003]	-0.0026* [-0.0048,-0.0004]	-0.0027* [-0.005,-0.0004]	-0.0076* [-0.0146, -0.0006]	-0.0089 [-0.0197, 0.002]
	NH (>20°N)	-0.0005 [-0.0028, 0.0017]	0.001 [-0.0028, 0.0048]	-0.0024 [-0.0065,0.0018]	-0.0044 [-0.01,0.0011]	-0.0055* [-0.0102, -0.0008]
	Tropics	0 [-0.0035, 0.0034]	-0.0032* [-0.006, -0.0004]	-0.0014 [-0.0057, 0.0029]	-0.012 [-0.035,0.011]	-0.0197 [-0.0567,0.0173]
	SH (>20°S)	-0.0042* [-0.006, -0.0023]	-0.0053* [-0.0093, -0.0013]	-0.004* [-0.0077, -0.0003]	-0.0071* [-0.0113,-0.0028]	-0.0037 [-0.0087,0.0013]
HSCAT	All	-0.0013 [-0.0031,0.0005]	-0.0022 [-0.0044,0.0001]	0.0016 [-0.0014,0.0047]	0.001 [-0.003,0.0049]	-0.0057* [-0.011,-0.0004]
	NH (>20°N)	0.0013 [-0.0021,0.0046]	0.0051 [-0.0014,0.0117]	-0.0048 [-0.0227,0.0131]	0.0053 [-0.0079,0.0186]	-0.0002 [-0.0237,0.0233]
	Tropics	-0.0005 [-0.0028,0.0019]	-0.0028 [-0.0056,0.0001]	0.0001 [-0.0027,0.0028]	0.0031 [-0.001,0.0073]	0.0018 [-0.0032,0.0068]
	SH (>20°S)	-0.0022 [-0.005,0.0005]	-0.0028 [-0.0063,0.0007]	0.0037 [-0.0008,0.0082]	-0.0012 [-0.0076,0.0051]	-0.0118* [-0.0196,-0.0039]

5 Conclusions

With the help of ECMWF OSE and scatterometer winds from Metop and HY-2B satellites, this study evaluates the impact of Aeolus wind assimilation on sea surface wind forecasts.

The results demonstrate the potential of Aeolus to improve the short-range sea surface wind forecasts for global oceans except for the tropics. In addition, zonal biases generally benefit from Aeolus wind assimilation, while the impact on meridional biases is mixed. Regarding medium-range forecasts, the results suggest that the extratropical ocean regions in the Southern Hemisphere tend to benefit most from Aeolus data assimilation.

Overall, this study provides information about which ocean regions benefit more from Aeolus wind observations. It also guides us to investigate the negative impact regions in the future, thus further improving the model performance and avoiding detrimental impact cases and biases.

Acknowledgements

We thank ECMWF for providing Aeolus OSE data and High-Performance Computing Facility for data analysis. Our appreciation also goes to Royal Netherlands Meteorological Institute (KNMI) and EUMETSAT OSI SAF for access to the HSCAT 25 km and ASCAT Level-2 25 km wind products. We would like to thank Anton Verhoef from KNMI for his technical support in using AWDP and PenWP. This research is a part of the PhD project Aeolus Satellite Lidar for Wind Mapping, a sub-project of the Innovation Training Network Marie Skłodowska-Curie Actions: Lidar Knowledge Europe (LIKE), supported by the European Union Horizon 2020 (Grant number: 858358). Otto Moensted Foundation supports half of the expenses for the external research stay at KNMI.

Availability Statement

The data of ECMWF OSEs in this study can be obtained from https://www.ecmwf.int/en/forecasts/dataset/ecmwf-research-experiments on application (ECMWF Research Department, 2022). The ASCAT winds at 25 km swath grid are available at EUMETSAT Data Center via https://eoportal.eumetsat.int/userMgmt/protected/welcome.faces with registration (EUMETSAT OSI SAF, 2009). The HSCAT winds at 25 km swath grid during the study period can be obtained from KNMI upon reasonable request (EUMETSAT OSI SAF, 2021).

The v3.3 of the ASCAT Wind Data Processor (AWDP) used for collocating wind forecasts with ASCAT winds is available at https://nwp-saf.eumetsat.int/site/software/scatterometer/awdp/ (EUMETSAT NWP SAF, 2020). The v4.0 of the Pencil Beam Wind Processor (PenWP) used for collocating wind forecasts with HSCAT winds can be downloaded from https://nwp-saf.eumetsat.int/site/software/scatterometer/penwp/ (EUMETSAT NWP SAF, 2022).

References

Aeolus Data Innovation and Science Cluster (DISC). (2020). Summary of Quality of Aeolus Data Products from 1st Reprocessing Campaign covering June to December 2019. ESA. Retrieved from https://earth.esa.int/eogateway/documents/20142/0/Aeolus-Summary-Reprocessing-1-DISC.pdf

Amiridis, V., Kampouri, A., Gkikas, A., Misios, S., Gialitaki, A., Marinou, E., et al. (2023). Aeolus winds impact on volcanic ash early warning systems for aviation. *Scientific Reports*, *13*(1), 7531. https://doi.org/10.1038/s41598-023-34715-6

Andersson, E., Dabas, A., Endemann, M., Ingmann, P., Källén, E., Offiler, D., & Stoffelen, A. (2008). *ADM-Aeolus Science Report* (No. SP-1311) (pp. 1–121). ESA. Retrieved from https://esamultimedia.esa.int/multimedia/publications/SP-1311/SP-1311.pdf

Belmonte Rivas, M., & Stoffelen, A. (2019). Characterizing ERA-Interim and ERA5 surface wind biases using ASCAT. *Ocean Science*, *15*(3), 831–852. https://doi.org/10.5194/os-15-831-2019

Belova, E., Kirkwood, S., Voelger, P., Chatterjee, S., Satheesan, K., Hagelin, S., et al. (2021). Validation of Aeolus winds using ground-based radars in Antarctica and in northern Sweden. *Atmospheric Measurement Techniques*, *14*(8), 5415–5428. https://doi.org/10.5194/amt-14-5415-2021

Borne, M., Knippertz, P., Weissmann, M., Martin, A., Rennie, M., & Cress, A. (2023). Impact of Aeolus wind lidar observations on the representation of the West African monsoon circulation in the ECMWF and DWD forecasting systems. *Quarterly Journal of the Royal Meteorological Society*, *149*(752), 933–958. https://doi.org/10.1002/qj.4442

ECMWF Research Department. (2022). ECMWF Research Experiments (RD) [Dataset]. MARS Catalogue. https://www.ecmwf.int/en/forecasts/dataset/ecmwf-research-experiments

ESA. (2022). Christmas comes early for Aeolus. Retrieved June 10, 2023, from https://www.esa.int/Applications/Observing_the_Earth/FutureEO/Aeolus/Christmas_comes_early_for_Aeolus

EUMETSAT NWP SAF. (2020). ASCAT Wind Data Processor (Version 3.3) [Software]. EUMETSAT. https://nwp-saf.eumetsat.int/site/software/scatterometer/awdp/

EUMETSAT NWP SAF. (2022). Pencil Beam Wind Processor (Version 4.0) [Software]. EUMETSAT. https://nwp-saf.eumetsat.int/site/software/scatterometer/penwp/

EUMETSAT OSI SAF. (2009). ASCAT Winds and Soil Moisture at 25 km Swath Grid – Metop [Dataset]. EUMETSAT. https://navigator.eumetsat.int/product/EO:EUM:DAT:METOP:OAS025

EUMETSAT OSI SAF. (2021). HSCAT Winds at 25 km Swath Grid - Hai Yang 2B [Dataset]. EUMETSAT. https://navigator.eumetsat.int/product/EO:EUM:DAT:0537

Garrett, K., Liu, H., Ide, K., Hoffman, R. N., & Lukens, K. E. (2022). Optimization and impact assessment of Aeolus HLOS wind assimilation in NOAA's global forecast system. *Quarterly Journal of the Royal Meteorological Society*, *148*(747), 2703–2716. https://doi.org/10.1002/qj.4331

Ingmann, P., & Straume, A. G. (2016). ADM-Aeolus Mission Requirements Document. ESA. Retrieved from https://esamultimedia.esa.int/docs/EarthObservation/ADM-Aeolus_MRD.pdf

Iwai, H., Aoki, M., Oshiro, M., & Ishii, S. (2021). Validation of Aeolus Level 2B wind products using wind profilers, ground-based Doppler wind lidars, and radiosondes in Japan. *Atmospheric Measurement Techniques*, *14*(11), 7255–7275. https://doi.org/10.5194/amt-14-7255-2021

Laroche, S., & St-James, J. (2022). Impact of the Aeolus Level-2B horizontal line-of-sight winds in the Environment and Climate Change Canada global forecast system. *Quarterly*

Journal of the Royal Meteorological Society, *148*(745), 2047–2062. https://doi.org/10.1002/qj.4300

Lee, S., Song, H., Kwon, I., & Kang, J. (2023). Impacts of Aeolus horizontal LINE-OF-SIGHT (HLOS) wind assimilation on the Korean integrated model (KIM) forecast system. *Atmospheric Science Letters*, *24*(3). https://doi.org/10.1002/asl.1138

Lux, O., Lemmerz, C., Weiler, F., Kanitz, T., Wernham, D., Rodrigues, G., et al. (2021). ALADIN laser frequency stability and its impact on the Aeolus wind error. *Atmospheric Measurement Techniques*, *14*(9), 6305–6333. https://doi.org/10.5194/amt-14-6305-2021

OSI SAF Winds Team. (2021). Product User Manual (PUM) for the HY-2 winds. EUMETSAT. Retrieved from https://scatterometer.knmi.nl/publications/pdf/osisaf_cdop3_ss3_pum_hy-2_winds.pdf

OSI SAF/EARS Winds Team. (2021). ASCAT Wind Product User Manual. EUMETSAT. Retrieved from https://scatterometer.knmi.nl/publications/pdf/ASCAT_Product_Manual.pdf

Pourret, V., Šavli, M., Mahfouf, J., Raspaud, D., Doerenbecher, A., Bénichou, H., & Payan, C. (2022). Operational assimilation of Aeolus winds in the Météo-France global NWP model ARPEGE. *Quarterly Journal of the Royal Meteorological Society*, *148*(747), 2652–2671. https://doi.org/10.1002/qj.4329

Ratynski, M., Khaykin, S., Hauchecorne, A., Wing, R., Cammas, J.-P., Hello, Y., & Keckhut, P. (2023). Validation of Aeolus wind profiles using ground-based lidar and radiosonde observations at Réunion island and the Observatoire de Haute-Provence. *Atmospheric Measurement Techniques*, *16*(4), 997–1016. https://doi.org/10.5194/amt-16-997-2023

Rennie, M., & Isaksen, L. (2020). Use of Aeolus observations at ECMWF. Retrieved May 22, 2023, from https://www.ecmwf.int/en/newsletter/163/news/use-aeolus-observations-ecmwf

Rennie, M., & Isaksen, L. (2022). The NWP impact of Aeolus Level-2B winds at ECMWF. ECMWF. Retrieved from https://confluence.ecmwf.int/display/AEOL/L2B+team+technical+reports+and+relevant+papers?preview=/46596815/288355970/AED-TN-ECMWF-NWP-025--20220810_v5.0.pdf

Stoffelen, A., Benedetti, A., Borde, R., Dabas, A., Flamant, P., Forsythe, M., et al. (2020). Wind Profile Satellite Observation Requirements and Capabilities. *Bulletin of the American Meteorological Society*, *101*(11), E2005–E2021. https://doi.org/10.1175/BAMS-D-18-0202.1

Straume-Lindner, A. G., Parrinello, T., Von Bismarck, J., Bley, S., Wernham, D., Kanitz, T., et al. (2021). ESA'S Wind Mission Aeolus - Overview, Status and Outlook. In *2021 IEEE International Geoscience and Remote Sensing Symposium IGARSS* (pp. 755–758). Brussels, Belgium: IEEE. https://doi.org/10.1109/IGARSS47720.2021.9554007

Vogelzang, J., & Stoffelen, A. (2021). Quadruple Collocation Analysis of In-Situ, Scatterometer, and NWP Winds. *Journal of Geophysical Research: Oceans*, *126*(5). https://doi.org/10.1029/2021JC017189

Witschas, B., Lemmerz, C., Geiß, A., Lux, O., Marksteiner, U., Rahm, S., et al. (2022). Validation of the Aeolus L2B wind product with airborne wind lidar measurements in the polar North Atlantic region and in the tropics. *Atmospheric Measurement Techniques*, *15*(23), 7049–7070. https://doi.org/10.5194/amt-15-7049-2022

World Meteorological Organization (WMO). (2020). *Vision for the WMO Integrated Global Observing System in 2040*. Retrieved from https://library.wmo.int/index.php?lvl=notice_display&id=21716

Žagar, N., Rennie, M., & Isaksen, L. (2021). Uncertainties in Kelvin Waves in ECMWF Analyses and Forecasts: Insights From Aeolus Observing System Experiments. *Geophysical Research Letters*, *48*(22). https://doi.org/10.1029/2021GL094716

Zuo, H., Hasager, C. B., Karagali, I., Stoffelen, A., Marseille, G.-J., & de Kloe, J. (2022). Evaluation of Aeolus L2B wind product with wind profiling radar measurements and numerical weather prediction model equivalents over Australia. *Atmospheric Measurement Techniques*, *15*(13), 4107–4124. https://doi.org/10.5194/amt-15-4107-2022

Technical University of Denmark

DTU Risø Campus
Frederiksborgvej 399
4000 Roskilde
Tlf. 46775085

www.wind.dtu.dk